



THE UNIVERSITY *of* EDINBURGH

Edinburgh Research Explorer

Application of noble gas tracers to identify the retention mechanisms of CO₂ migrated from a deep reservoir into shallow groundwater

Citation for published version:

Ju, Y, Gilfillan, S, Lee, S-S, Kaown, D, Hahm, D, Lee, S, Park, I-W, Ha, S-W, Park, K, Do, H-K, Yun, S-T & Lee, K-K 2020, 'Application of noble gas tracers to identify the retention mechanisms of CO₂ migrated from a deep reservoir into shallow groundwater', *International Journal of Greenhouse Gas Control*, vol. 97. <https://doi.org/10.1016/j.ijggc.2020.103041>

Digital Object Identifier (DOI):

[10.1016/j.ijggc.2020.103041](https://doi.org/10.1016/j.ijggc.2020.103041)

Link:

[Link to publication record in Edinburgh Research Explorer](#)

Document Version:

Peer reviewed version

Published In:

International Journal of Greenhouse Gas Control

General rights

Copyright for the publications made accessible via the Edinburgh Research Explorer is retained by the author(s) and / or other copyright owners and it is a condition of accessing these publications that users recognise and abide by the legal requirements associated with these rights.

Take down policy

The University of Edinburgh has made every reasonable effort to ensure that Edinburgh Research Explorer content complies with UK legislation. If you believe that the public display of this file breaches copyright please contact openaccess@ed.ac.uk providing details, and we will remove access to the work immediately and investigate your claim.



Manuscript Details

Manuscript number	JGGC_2019_597_R2
Title	Application of noble gas tracers to identify the retention mechanisms of CO ₂ migrated from a deep reservoir into shallow groundwater
Article type	Full Length Article

Abstract

Carbon Capture and Storage (CCS) is a valuable climate-mitigation technology, which offers the potential to cost-effectively reduce the emissions associated with the burning of fossil fuels. However, there is a potential risk of a small portion of the stored CO₂ unintentionally migrating from a storage site to a shallow groundwater aquifer which is the final retaining zone for any migrated CO₂ before it escapes to the atmosphere. Hence, it is imperative to identify the physical retention mechanisms of CO₂ within a shallow aquifer. In this study 1.70x10² kg of CO₂ and noble gas tracers (He, Ar and Kr) were continuously injected into a groundwater aquifer over 28 days with the aim of identifying the mechanisms and amount of CO₂ retention. Among the tracers, Kr was found to be the earliest indicator of CO₂ migration. The other tracers – He and Ar – arrived later and exhibited diluted signals. The diluted signals were attributed to degassing of the plume mass (1.6% of CO₂) during the early stages of CO₂ migration. Diffusion accelerated the dilution of the lighter elements at the plume boundaries. Consequently, the clear relation of the noble gases with the CO₂ proved that degassing and mixing primarily control the mass retention of CO₂ in shallow groundwater, and the relative importance of these processes varies along the evolving path of migrating CO₂.

Keywords	CCS; monitoring; CO ₂ leakage; noble gas tracing; artificial tracer; geochemical monitoring
Corresponding Author	Kang-Kun Lee
Corresponding Author's Institution	Seoul National University - School of Earth and Environmental Sciences
Order of Authors	YeoJin Ju, Stuart Gilfillan, Seong-Sun Lee, Dugin Kaown, Doshik Hahm, Sanghoon Lee, In-Woo Park, Seung-Wook Ha, Keyhong Park, Hyun-Kwon Do, Seong-Taek Yun, Kang-Kun Lee
Suggested reviewers	Greg Holland, Finlay Stuart, Stephanie Flude, Domokos Gyore

Submission Files Included in this PDF

File Name [File Type]

Cover letter.docx [Cover Letter]

Response to Reviewers.docx [Response to Reviewers]

[1] Ju et al.,_revised.docx [Review Reports]

Highlights_revised.docx [Highlights]

[2] Ju et al.,_revised.docx [Manuscript File]

Figure1.tif [Figure]

Figure2.tif [Figure]

Figure3.tif [Figure]

Figure4_revised.tif [Figure]

Figure5.tif [Figure]

Figure 6_revised.tif [Figure]

Figure7_revised.tif [Figure]

Figure8.tif [Figure]

Figure9.tif [Figure]

Figure10.tif [Figure]

Figure11.tif [Figure]

Figure12.tif [Figure]

declaration-of-competing-interests.docx [Conflict of Interest]

Credit Author Statement.docx [Author Statement]

Supplementary Material.docx [Supplementary Material]

To view all the submission files, including those not included in the PDF, click on the manuscript title on your EVISE Homepage, then click 'Download zip file'.

Research Data Related to this Submission

Data set <https://data.mendeley.com/datasets/hrydvx2xgp/1>

The dataset associated with the mass balance calculation

You can find all the dataset associated with the mass balance calculation (Figure 8~12).

Seoul National University
College of Natural Sciences

School of Earth and Environmental Sciences, Seoul National University,
Seoul 08826, Republic of Korea



March 27, 2020

Editors-in-chief

International Journal of Greenhouse Gas Control

Dear Editors-in-chief,

RE: Manuscript by Ju, Gilfillan, Lee et al. “**Application of noble gas tracers to identify the retention mechanisms of CO₂ migrated from a deep reservoir into shallow groundwater**”

Once again, we would like to thank the associate editor and all the reviewers for very informative and constructive comments for the improvement of our manuscript. We tried to respond to every comment by the reviewers and incorporated the responses into the revised manuscript. You can find all details in the ‘Response to Reviewers.docx’ file listing all the comments and responses.

I hope the revised manuscript is suitable for publication in the *International Journal of Greenhouse Gas Control*.

Sincerely,

Kang-Kun Lee, Ph.D.

Professor and Chair, School of Earth and Environmental Sciences

Seoul National University

Seoul 08826, Korea

Email: kklee@snu.ac.kr

Phone: +82-2-880-8161

Fax: +82-2-873-3647

[Reviewer 1]

Once again, we thank Reviewer #1 for his/her very detailed reading of our manuscript and associated comments and suggestions. Please see our responses below with the revised version of the manuscript ([1] Ju et al.,_revised).

Specific comments

Introduction

1) Line 40 (Languages)

- RESPONSE: CHANGES MADE.
- It has been modified as below:
- From: "This leaked CO₂ could potentially migrate through geological conduits such as permeable faults and/or abandoned wells resulting in the deterioration of fresh water resources above the CO₂ reservoir"
- To: "This CO₂ could potentially migrate through geological conduits such as permeable faults and/or abandoned wells resulting in the deterioration of fresh water resources above the CO₂ reservoir" (Lines 40–42 in [1]).

2) Line 70 (Languages)

- RESPONSE: CHANGES MADE.
- It has been modified as below:
- From: "The degree of solubility trapping has also been determined using noble gases, through identification of the fractionation of naturally present noble gas tracers due to the partitioning of the noble gases into groundwater present within the reservoir formations"
- To: "The degree of solubility trapping has also been determined using noble gases, through identification of the degree of partitioning of the noble gases into groundwater present within the reservoir formations" (Lines 69–71 in [1]).

Materials and methods

3) Line 145 (Languages)

- RESPONSE: CHANGES MADE.
- It has been modified as below:
- From: "The SMWs are located along the created groundwater flow, while PS-04 was upgradient relative to the CO₂ injection point."
- To: "The SMWs are located along the created groundwater flow pathway, while PS-04 was up-gradient relative to the CO₂ injection point." (Lines 143–144 in [1])

4) Line 147 (Languages)

- RESPONSE: CHANGES MADE.
- It has been modified as below:
- From: "The well BS-09 was intended to capture the preferential movement of a released CO₂ along a high connectivity zone between injection well and BS-09, identified in the work of Ju et al. (2019)."
- To: "The well BS-09 was intended to capture the preferential movement of the released CO₂ along a high connectivity zone between injection well and BS-09, identified in the work of Ju et al. (2019)." (Lines 144–146 in [1])

5) Line 229 (Languages)

- RESPONSE: CHANGES MADE.
- It has been modified as below:
- From: "...before samples injection into the RGA200 mass spectrometer (Stanford Research Systems, California, USA)."
- To: "...before sample injection into the RGA200 mass spectrometer (Stanford Research Systems, California, USA) for analysis." (Lines 229–230 in [1])

Results

6) Line 376-377 (Languages)

- RESPONSE: CHANGES MADE.
- It has been modified as below:
- From: "This was attributed to dilution of CO₂ plume along a concentration gradient"
- To: "This was attributed to the Kr taking a less distributed pathway through the subsurface than the other tracers, and a result of the dilution of CO₂ plume along the concentration gradient" (Lines 370–372 in [1]).

7) Line 389-391 (Languages)

- RESPONSE: CHANGES MADE.
- It has been modified as below:
- From: "Note that SMW 4-2 showed a stronger signal at the plateau than SWM 3-2 did (Figure 6), implied a low conductivity zone existing and hindering the SMW 3-2 from capturing a CO₂ plume efficiently. This result was consistent with the observations made in alkalinity and pCO₂ (Figure 5)."
- To: "It is worth noting that SMW 4-2 exhibited a higher concentration of Kr once the tracers arrived than SWM 3-2 (Figure 6), implying that a low conductivity zone hinders well SMW 3-2 from capturing the full CO₂ plume. This result was consistent with the observations made in alkalinity and pCO₂ (Figure 5)." (Lines 383–386 in [1])

8) Line 403 (Languages)

- RESPONSE: CHANGES MADE.
- It has been modified as below:
- From: "In the final stage of BTCs, the plume tail is recorded in all of the monitoring wells through the decrease of noble gas concentration resulting after the injection at the IW ceased."
- To: "In the final stage of BTCs, the plume tail is recorded in all of the monitoring wells through the decrease of noble gas concentrations after injection at the IW ceased." (Lines 397–399 in [1])

Conclusions

9) Line 603-604 (Languages)

- RESPONSE: CHANGES MADE.
- It has been modified as below:
- From: "Around the leak point, CO₂ degassing dominantly occurred from a dissolved plume of high gas pressure, suggesting a near-surface monitoring network is necessary for capturing the active "vertical" movement of degassed budget in this area."

- To: "Our findings indicate that around the injection point, CO₂ degassing dominantly occurs from the dissolved plume due to the high gas pressure, suggesting a near-surface monitoring network is necessary for capturing the active "vertical" movement of degassed budget in this area." (Lines 595–598 in [1])

[Reviewer 2]

Once again, we thank Reviewer #2 for his/her very detailed reading of our manuscript and associated comments and suggestions. Please see our responses below with the revised version of the manuscript ([1] Ju et al.,_revised).

General observations

The authors have made changes that have improved the manuscript significantly. I have a couple substantial comments however that need attention.

- RESPONSE: CHANGES MADE.
- We sincerely appreciate your thorough review. Please find detailed responses below.

Major comments

Results

1) **Table 1** has several errors. First, the exponents for the values were not fully updated and so the results are non-sensical.

- RESPONSE: CHANGES MADE.
- My apologies for the confusion. The exponents have been fully updated according to your comment (Table 1 in [1]).

Second, the data originally shown for "% lost" were not updated when the column title was changed to "% remaining".

- RESPONSE: CHANGES MADE.
- My apologies for the confusion. The column has been updated according to the changed title (Table 1 in [1]).

2) A major conclusion of this work is that the Kr plume front precedes the CO₂ plume front. However, that is difficult to see based on comparisons of Figs. 5 and 6. Perhaps you could add a BTC figure that plots these two gases at the higher time resolution of Fig. 6, to help convince the reader that Kr precedes CO₂. It might work to add pCO₂ to Fig. 6, but it might also be too difficult to see with all four gases plotted.

- RESPONSE: CHANGES MADE.
- Thank you for the beneficial comment. This has been modified according to your suggestions in the revised version of the manuscript (Figure 6 in [1]).

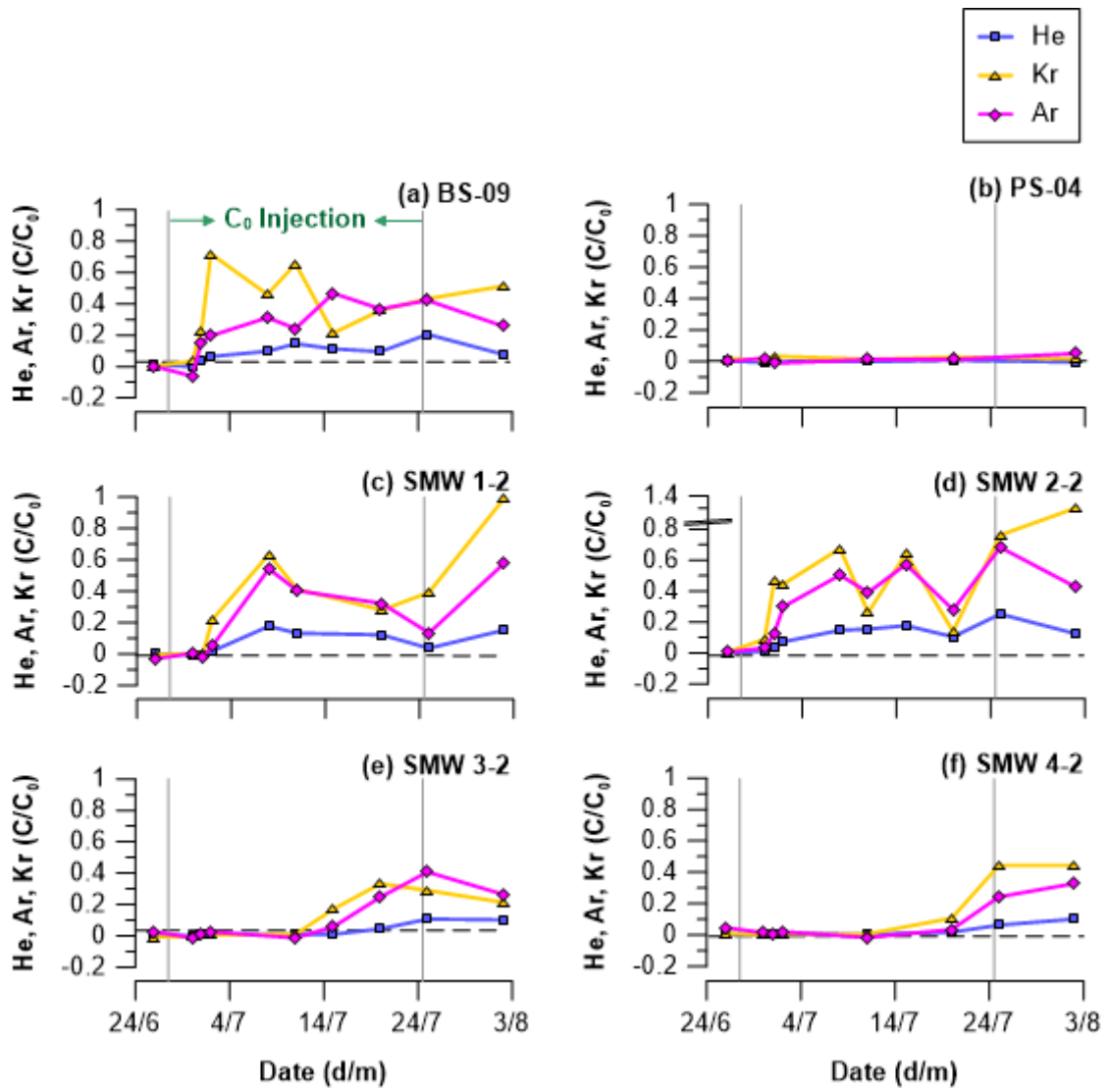


Figure R1 Original version of Figure 6.

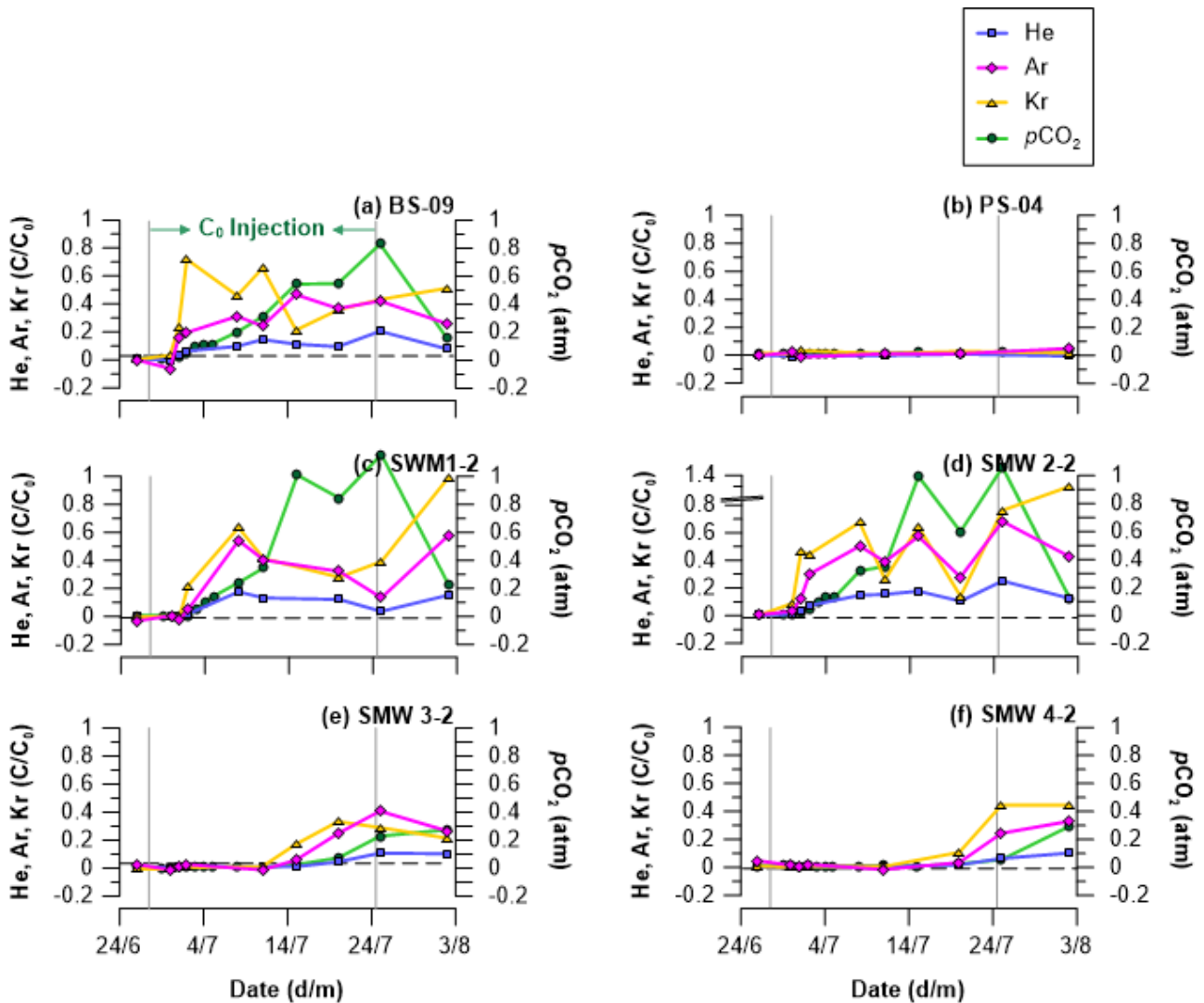


Figure R2 Modified version of Figure 6.

Specific comments

We sincerely appreciate the English corrections. All of your suggestions have been accepted and reflected in the revised version of the manuscript.

Introduction

3) **Line 82-83** change to read "... and ASW. Differences in the noble gas contents of these samples stemmed from ..."

- RESPONSE: CHANGES MADE.
- It has been modified according to your comment (Lines 86–87 in [1]).

4) **Line 98** delete "artificial" (there is no such thing as an artificial noble gas!)

- RESPONSE: CHANGES MADE.
- It has been modified according to your comment (Line 102 in [1]).

Materials and methods

- 5) **Line 152** delete "works".
- RESPONSE: CHANGES MADE.
 - It has been modified according to your comment (Line 166 in [1]).
- 6) **Line 200** change to read "Figure 3. Schedule for water sample collection during the CO2 injection test"
- RESPONSE: CHANGES MADE.
 - It has been modified according to your comment (Lines 206–207 in [1]).
- 7) **Line 222** change to read ". . . before sample injection . . ."
- RESPONSE: CHANGES MADE.
 - It has been modified according to your comment (Line 229 in [1]).

Results

- 8) **Line 246** change to read "However, prior to the experiment the hydrostatic pressure data showed a stable correlation with atmospheric pressure changes and no irregular turbulence . . ."
- RESPONSE: CHANGES MADE.
 - It has been modified according to your comment (Lines 254–256 in [1]).
- 9) **Line 256** delete "to"
- RESPONSE: CHANGES MADE.
 - It has been modified according to your comment (Line 264 in [1]).
- 10) **Line 257** change to read "In contrast, wells SMW 3-2 . . ."
- RESPONSE: CHANGES MADE.
 - It has been modified according to your comment (Lines 264–265 in [1]).
- 11) **Line 344** change to read "The pH also decreased noticeably, . . ."
- RESPONSE: CHANGES MADE.
 - It has been modified according to your comment (Line 352 in [1]).
- 12) **Figure 6** Still need to change the order of the noble gases in the figure legend so that they align with atomic mass (i.e., He, Ar, Kr).
- RESPONSE: CHANGES MADE.
 - The legend has been modified according to your suggestion (Figure 6 in [1]).

Discussion

- 13) **Figure 8, 9, 10 and 11** Vertical axis title is only partly shown.
- RESPONSE: EXPLAINED.
 - They look okay in both word and pdf format. In case, the figures were also uploaded to the website as a separate file.

Conclusions

14) **Line 562** change to read: “. . . plume and the other . . .”

- RESPONSE: CHANGES MADE.
- It has been modified according to your comment (Line 580 in [1]).

15) **Line 592** change to read “. . . just a few meters from the leak point . . .”

- RESPONSE: CHANGES MADE.
- It has been modified according to your comment (Line 611 in [1]).

16) **Line 596** spelling of “gaseous”

- RESPONSE: CHANGES MADE.
- It has been modified according to your comment (Line 615 in [1]).

17) **Line 596-597** change to read “. . . pathways in the vadose zone depending on the . . .”

- RESPONSE: CHANGES MADE.
- It has been modified according to your comment (Lines 615–616 in [1]).

1 **Application of noble gas tracers to identify the retention mechanisms of CO₂ migrated from a**
2 **deep reservoir into shallow groundwater**

3 YeoJin Ju¹, Stuart M. V. Gilfillan², Seong-Sun Lee¹, Dugin Kaown¹, Doshik Hahm³, Sanghoon Lee¹,
4 In-Woo Park¹, Seung-Wook Ha¹, Keyhong Park⁴, Hyun-Kwon Do⁵, Seong-Taek Yun⁵, Kang-Kun
5 Lee^{1,*}

6 ¹School of Earth and Environmental Sciences, Seoul National University, 1 Gwanak-ro, Gwanak-gu,
7 Seoul, 08826, South Korea.

8 ²School of GeoSciences, The University of Edinburgh, Grant Institute, James Hutton Road, Edinburgh
9 EH9 3FE, UK.

10 ³Department of Oceanography, Pusan National University, Busan, South Korea.

11 ⁴Korea Polar Research Institute, Incheon, South Korea.

12 ⁵Department of Earth and Environmental Sciences, Korea University, Seoul 02841, South Korea.

13 Email: jinee18@snu.ac.kr, stuart.gilfillan@ed.ac.uk, soon3311@snu.ac.kr, dugin1@snu.ac.kr,
14 hahm@pusan.ac.kr, lshlsh2311@snu.ac.kr, inwoo0415@snu.ac.kr, hasabana@snu.ac.kr,
15 keyhongpark@kopri.re.kr, iq1pc@korea.ac.kr, styun@korea.ac.kr.

16 *Corresponding author. Tel.: +82 2 873 3647. E-mail address: kkleee@snu.ac.kr.

17

18 **Abstract**

19 Carbon Capture and Storage (CCS) is a valuable climate-mitigation technology, which offers
20 the potential to cost-effectively reduce the emissions associated with the burning of fossil fuels.
21 However, there is a potential risk of a small portion of the stored CO₂ unintentionally migrating from a
22 storage site to a shallow groundwater aquifer. ~~The shallow groundwater which~~ is the final retaining
23 zone for any migrated CO₂ before it escapes ~~into~~ the atmosphere. Hence, it is imperative to ~~To~~ identify
24 the physical retention mechanisms of CO₂ within a shallow aquifer. In this study 1.70x10² kg of CO₂
25 and noble gas tracers (He, Ar and Kr) were continuously injected into a groundwater aquifer over 28
26 days with the aim of identifying the mechanisms and amount of CO₂ retention. Among the tracers, Kr
27 was found to be the earliest indicator of CO₂ migration. The other tracers – He and Ar – arrived later
28 and exhibited diluted signals. The diluted signals were attributed to degassing of the plume mass (1.6%
29 of CO₂) during the early stages of CO₂ migration. Diffusion accelerated the dilution of the lighter
30 elements at the plume boundaries. Consequently, the clear relation of the noble gases with the CO₂
31 proved that degassing and mixing primarily control the mass retention of CO₂ in shallow groundwater,
32 and the relative importance of these processes ~~is differentiated~~ varies along the evolving path of
33 migrating CO₂.

34 **Keywords:** CCS; monitoring; CO₂ leakage; noble gas tracing; artificial tracer; geochemical monitoring

35 1. Introduction

36 Carbon Capture and Storage (CCS) is a climate change mitigation technology that comprises
37 the capture of CO₂ from an industrial point source, such as a power plant or refinery, transport of the
38 captured CO₂ to a storage site followed by the injection of the captured CO₂ into deep geological strata
39 for permanent disposal (IPCC, 2005). However, there is a potential risk that a small portion of the
40 mobile CO₂ in a storage site could accidentally migrate out of the subsurface reservoir and inadvertently
41 reach shallower levels of the subsurface (Alcalde et al., 2018). This ~~leaked~~ CO₂ could potentially
42 migrate through geological conduits such as permeable faults and/or abandoned wells resulting in the
43 deterioration of fresh water resources above the CO₂ reservoir (Harvey et al., 2012; IEAGHG, 2011;
44 Lemieux, 2011; Lion et al., 2014) and ~~in the~~ leakage of a small portion of the CO₂ into the atmosphere
45 (Ide et al., 2006; IPCC, 2005). Recently, the Weyburn-Midale (Canada) CO₂ monitoring and storage
46 project faced allegations that leakage of CO₂ injected into the Weyburn-Midale oil field for Enhanced
47 Oil Recovery (EOR) and storage was causing a deterioration of the groundwater quality on a farm
48 located above the field (Beaubien et al., 2013; Gilfillan et al., 2017).

49 A variety of geochemical tools have been used to verify CO₂ storage security and track the fate
50 of CO₂ injected for storage. These include CO₂ soil gas and groundwater concentrations, stable C and
51 O isotopes within the CO₂, on-site monitoring parameters (pH, alkalinity, ORP, EC, temperature and
52 DO), inert gas tracers, major and trace ions and radiocarbon (¹⁴C) (Flude et al., 2016; Lee et al., 2016).
53 Soil gas and dissolved CO₂ concentrations in groundwater can provide a direct tracer of CO₂ migration,
54 allowing discrimination of different CO₂ origins and providing a means to establish the mass balance
55 of CO₂ present in the groundwater system (Ballentine et al., 2001; Beaubien et al., 2014; Gilfillan et al.,
56 2011; Lollar et al., 1997; Sathaye et al., 2016). Recent developments in on-site monitoring technologies
57 now allow the continuous measurement of a number of parameters (e.g. alkalinity, T, EC, pH) which
58 can be used to establish the overall distribution and temporal evolution of a small CO₂ plume within a
59 shallow groundwater aquifer (Lee et al., 2016). Noble gases are characterized by their- inert behavior,
60 which makes them ideal tracers within a subsurface system. This inertness means that noble gases are

61 conservative tracers and do not partake in the chemical reactions that dilute the CO₂ leakage signals and
62 hence are capable of providing a robust means to distinguish between natural and stored CO₂ (Risk et
63 al., 2015).

64 Noble gas tracing techniques have been used to track both the fate and migration pathways of
65 injected CO₂ in reservoirs. Within a typical porous CO₂ storage reservoir, CO₂ is retained by a
66 combination of structural, residual and solubility trapping mechanisms (Alcalde et al., 2018; Holland
67 and Gilfillan, 2013; IPCC, 2005). Recent experiments at the CO₂CRC Otway Demonstration site for
68 CO₂ storage in Australia have used Kr and Xe as conservative tracers to determine the degree of residual
69 trapping within a porous saline formation, using a numerical mass balance approach (LaForce et al.,
70 2014). The degree of solubility trapping has also been determined using noble gases, through
71 identification of the ~~degree of fractionation of naturally present noble gas tracers due to the~~ partitioning
72 of the noble gases into groundwater present within the reservoir formations (Ballentine et al., 1991;
73 Brennwald et al., 2005; Gilfillan et al., 2008, 2009; 2014; Pinti and Marty, 1995; Zhou et al., 2005).

74 Noble gas tracers are also suitable for monitoring the vertical migration of the reservoir CO₂,
75 thanks to the compositional difference of natural noble gas tracers between storage reservoir and ~~the~~
76 near surface environment (Mackintosh and Ballentine, 2012). Gilfillan et al. (2011) applied noble gas
77 tracing tools to constrain the nature of CO₂ leakage into shallow groundwater and surface water bodies.
78 ~~The Further work by Gilfillan et al., (2017) used~~ inherent tracers residing in ~~a the Weyburn-Midale~~
79 ~~injection and storage project reservoir CO₂ reservoir provided a means~~ to show that CO₂- migration
80 from ~~a the~~ deep reservoir into the shallow aquifer system had not occurred ~~near an artificial CO₂~~
81 ~~injection site at the Weyburn-Midale Storage and Monitoring project. This work found that as the~~ noble
82 gas composition ~~in the groundwater samples above the CO₂ injection and storage project~~ did not vary
83 over a typical background level of a shallow aquifer, ~~that is, the of~~ Air Saturated Water (ASW) with an
84 excess air component of up to 45% (Gilfillan et al., 2017). Recent work by Flude et al. (2016) and Flude
85 et al. (2017) evaluated the inherent tracing ability of noble gases focusing on the compositional
86 difference of them between captured CO₂, the subsurface storage reservoir, air and ASW. ~~The~~

87 ~~distinguished composition of~~ Differences in the noble gases contents of these samples ~~between the~~
88 ~~sampled gases~~ stemmed from the different CO₂ capturing processes and what controls the composition
89 of noble gas tracer in a stored fluid (e.g. gas stripping of reservoir water and/or interaction with
90 radiogenic components).

91 The concept of inert tracers was extended to artificial enhancement studies, involving the
92 addition of inert gas tracers such as SF₆ and noble gases to the injected CO₂ in CCS storage. This aimed
93 to provide a much clearer distinction between the injected CO₂ and that naturally present in the
94 subsurface and so improving the monitoring efficiency (Myers et al., 2013; Nimz and Hudson, 2005).
95 For example, noble gases have been previously used as artificial tracers to indicate CO₂ leakage
96 pathways in the vadose zone (Cohen et al., 2013; Rillard et al., 2015) and in the aquifer system (Lu et
97 al., 2012; Nimz and Hudson, 2005; Stalker et al., 2009). In the CO₂-Vadose project, undertaken at a test
98 CO₂ release site in France, the lighter noble gases (He and Ne) were found to have the fastest arrival
99 time in monitoring wells due to their higher diffusion coefficient and low solubility within the soil water
100 compared to the CO₂ and other tracers (Cohen et al., 2013). In contrast, the heavier noble gas tracers
101 (Kr and Xe) exhibited the fastest arrival in the aquifer system due to their solubility in groundwater
102 compared to other noble gases following the artificial injection into a deep reservoir (~2 km) (Stalker
103 et al., 2015). In a recent test, a small amount of CO₂ (16.9 kg) spiked with ~~artificial~~ noble gas was
104 released into a shallow aquifer at Korea CO₂ Storage Environmental Management (K-COSEM) study
105 site, in order to understand the behavior of the leaked plume in the shallow groundwater system. This
106 study identified that the mass distribution of the leaked CO₂ is predominantly controlled by the
107 solubility of the individual noble gases and mixing processes during the limited time of monitoring
108 work (i.e. 4 months) (Ju et al., 2019).

109 The shallow groundwater is the final zone encountered by migrating CO₂ before it is lost into
110 the vadose zone and atmosphere. Furthermore, this reservoir is directly linked into the human activity,
111 hence, should be protected from a potential leakage of stored CO₂ (Lee et al., 2016). While noble gas
112 tracers have proven useful to monitor leaked CO₂ plume in shallow aquifer systems (Flude et al., 2016;

113 2017), this has only been demonstrated on a few occasions, for example, in a natural CO₂ production
114 site using inherent noble gases (Gilfillan et al., 2011), in a CO₂ injection test site using artificially
115 enhanced noble gases (Ju et al., 2019) and to rule out CO₂ migration in a shallow aquifer above an
116 actual CO₂ storage reservoir using inherent noble gases (Gilfillan et al., 2017), as described above. In
117 this study, we presents the results of applying noble gases to a CO₂ injection test into a near-surface
118 aquifer. This artificial CO₂ migration test aims to mimic a situation where a measurable amount of CO₂
119 (1.70x10² kg) has migrated from a deep CO₂ storage reservoir into a shallow groundwater aquifer. This
120 study ~~aims~~ focuses on ~~to~~ determin~~ing~~ing the amount of CO₂ retained in the groundwater and the
121 mechanisms controlling the migration of the CO₂ plume using noble gas tracers. A mass balance model
122 was constructed based on the partitioning coefficients of noble gas tracers in a gas-water system, to
123 understand and to quantify the final retention of the injected CO₂ within the shallow aquifer system.

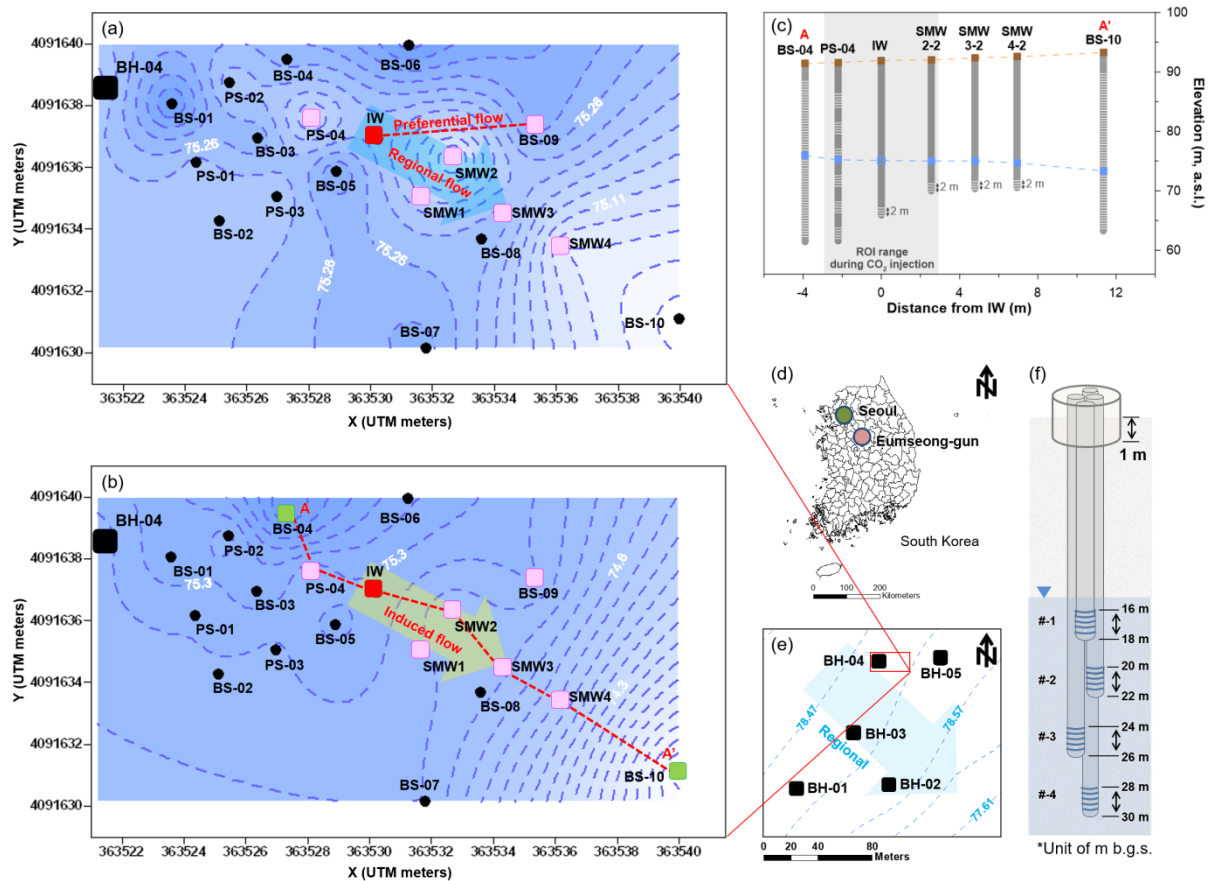
124 2. Materials and methods

125 2.1 Site description

126 The Korea CO₂ Storage Environmental Management (K-COSEM) Research Center has
127 installed a controlled CO₂ release experiment at Eumseong gun (county) of South Korea (Figure 1). The
128 geology at the field experimental site includes three different subsurface media, firstly consisting of a
129 weathered soil layer composed of medium to coarse grained silty sand (0–30 m below ground surface
130 (bgs)), followed by weathered biotite granite (30–70 m bgs), and finally consolidated biotite granite
131 (starting at 70 m bgs) (Lee et al., 2017; Ju et al., 2018a). The water level was located at the 16.0–18.4
132 m bgs and the hydraulic conductivity of the aquifer was estimated from pumping tests, ranging from
133 1.7×10^{-5} cm/s for the consolidated bedrock to 2.0×10^{-4} cm/s for the weathered layer. Prior to the
134 commencement of the experiment, the groundwater was flowing from the northwest toward the
135 southeast following a hydraulic gradient of 0.003 (i.e., the regional flow in Figure 1a).

136 At the K-COSEM site, a total of 24 monitoring wells had been installed in the shallow aquifer
137 (i.e. < 15 m below the water table) including the injection well (IW), partially screened (PS), boreholes
138 (BH), borehole screened (BS) and saturated zone monitoring wells (SMWs) (Figure 1a). Each saturated

139 zone monitoring well (SMW) contained several screened multi-depth monitoring wells for groundwater
140 monitoring at different depths (Figure 1f). In this CO₂ injection study, the IW and six monitoring wells
141 (PS-04, SMW1 to 4, BS-04, -09 and -10) were employed for the CO₂ injection experiment (Figure 1b).
142 The wells BS-04 and BS-10 located at both ends of the monitoring range were used to create an induced
143 pressure gradient field by pumping out groundwater at a down-gradient location (BS-10) and successive
144 injection in at an up-gradient location (BS-4) (Figure 1c). The SMWs are located along the created
145 groundwater flow pathway, while PS-04 was up-gradient relative to the CO₂ injection point. The well
146 BS-09 was intended to capture the preferential movement of ~~a~~-the released CO₂ along a high
147 connectivity zone between injection well and BS-09, identified in the work of Ju et al. (2019). Details
148 on the study site and monitoring network can also be found in previous works (Lee et al., 2017; Lee et
149 al., 2018; Ju et al., 2018b; Ju et al., 2019).



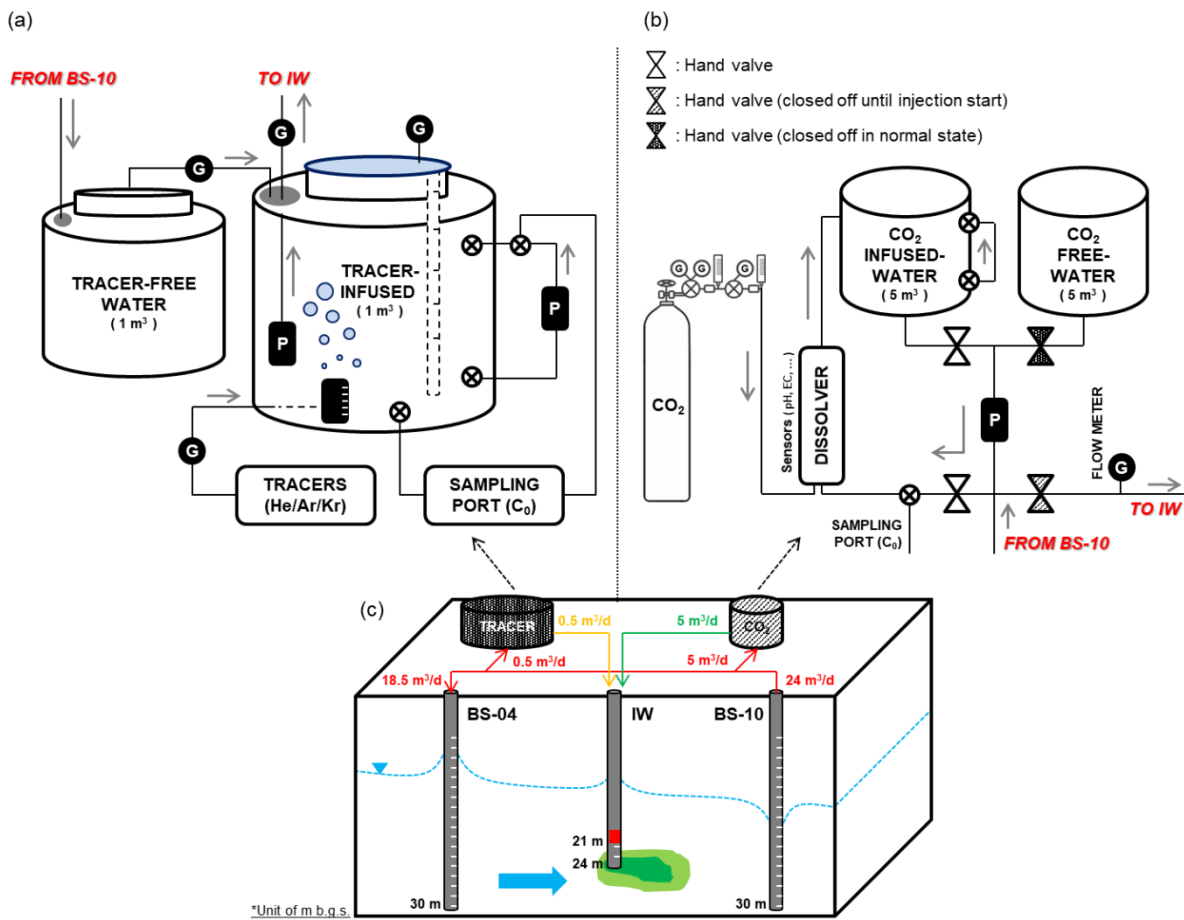
150

151 **Figure 1.** Maps of the study site. Figures on the left show (a) natural pressure gradient regional
 152 groundwater flow field (shown as a blue-colored arrow) before enhanced groundwater circulation using
 153 the wells BS-04 and BS-10, where a preferential path exists in this field due to local hydrogeological
 154 heterogeneity (16 May 2016), (b) induced pressure gradient field (shown as a green-colored arrow) after
 155 the pumping out and pumping in using the two wells (see green squares) (4 July 2016). Note that the
 156 induced flow was intended to speed up the plume migration along the groundwater flow (i.e., regional
 157 flow in [a]). Pink squares represent the wells used for monitoring works; a red square represents the
 158 injection well (IW). Figures on the right show (c) a cross-section view along the induced pressure
 159 gradient (4 July 2016), (d) the location map of the study area, (e) the contours of groundwater levels
 160 obtained by kriging using 17 wells surrounding the study site (7 March 2015), and (f) the structure of
 161 each saturated zone monitoring well (SMW) containing a bundle of four screened pipes with different
 162 lengths.

163 2.2 Artificial injection

164 2.2.1 Induced pressure gradient field

165 The CO₂ injection was undertaken in the induced pressure gradient field to reinforce the
166 groundwater flow, therefore, to speed up the CO₂ plume migration (Figure 2c). The hydraulic pressure
167 gradient was achieved by enhancing groundwater circulation ~~work~~, consisting of water production and
168 reinjection using the BS-04 and BS-10 wells located at both ends of the monitoring network (Figure
169 2c). A total of 24.0 m³/d of groundwater was pumped from BS-10 and reinjected into BS-04 (Figure
170 2c). A period of 1 month was required to stabilize the pressure gradient (22 May 2017 to 27 June 2017).
171 The pressure gradient was steeper near the injection site and production points (i.e. the BS-04 and BS-
172 10), with the average gradient being 0.18 (Figure 2c). The circulation was maintained until 17
173 September 2017.



174

175 **Figure 2.** Injection systems for the artificial CO₂ release experiment. (a) tracer-infused groundwater

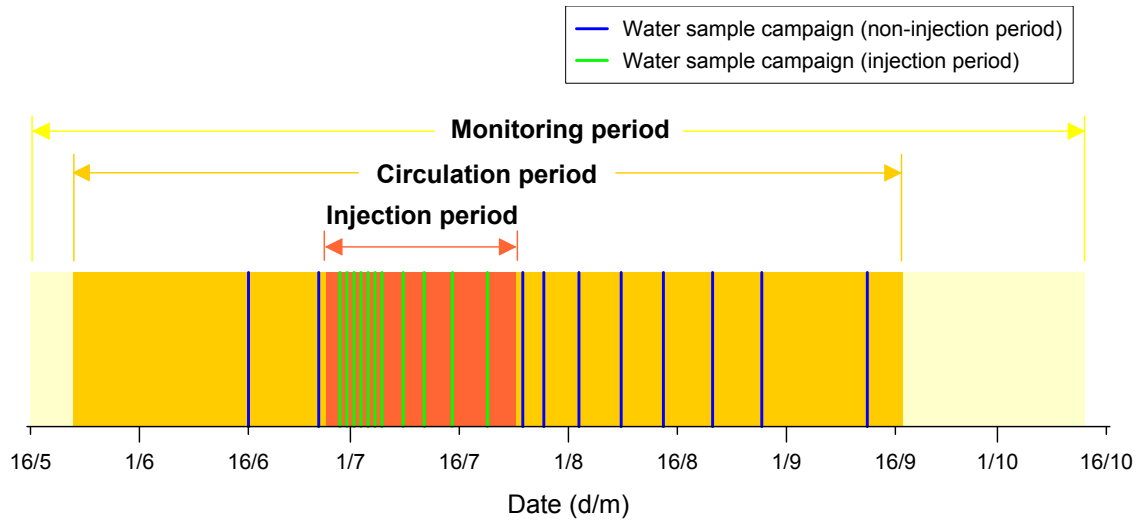
176 was prepared in a 1 m³ tank and (b) CO₂-infused groundwater was prepared in a 5 m³ tank. (c) gas-
177 charged groundwater was continuously released into the induced pressure gradient field through the
178 IW.

179 **2.2.2 Injection**

180 To prepare the injection water, the water flux sent to BS-04 (24.0 m³/d) was reduced to 18.5
181 m³/d and 5.5 m³/d of groundwater was sent into the injection tank (Figure 2c). 5.0 m³/d of groundwater
182 was sent into the CO₂ dissolver tank (Figure 2b) and 0.5 m³/d of tracer-enhanced water was prepared
183 in the other tank (Figure 2a). The CO₂-infused groundwater was prepared in the 5 m³ tank equipped
184 with the circulation pump, CO₂ dissolver, water sampling port and flow meter (Figure 2b). Injection
185 was initiated when the CO₂ concentration reached the equilibrium state (termed C₀). To ensure that the
186 equilibrium concentration was maintained, alkalinity, pH, EC, DO, ORP, temperature, salinity, TDS
187 was continuously monitored with real time measurement devices such as YSI (YSI Inc./Xylem Inc.,
188 USA), LTC Levellogger Junior (Solinst, Canada) and SH-300-DS (SOHA TECH, Inc., Korea) while
189 circulating water within the tank using a pump (Figure 2b). These measurements showed that it took
190 approximately 24 hours to achieve the equilibrium state. The noble gas infused groundwater was also
191 prepared one day ahead of the injection test. Approximately 0.5 m³/d of groundwater was pumped into
192 the 1 m³ of closed tank equipped with the circulation pump, tracer tank, water sampling port and flow
193 meter (Figure 2a). ~~Tracers~~ The injected tracers were a mixture of He (0.2 vol. %), Ar (99.4 vol. %), and
194 Kr (0.4 vol. %) and were injected through a flowmeter and diffuser (AS-10 3/8) into the 1 m³ dissolver
195 tank. The infused liquids were first injected into the subsurface on 27 June 2017 and continued to be
196 injected for 27 days until 24 July 2017. Samples for initial concentration analyses (i.e. C₀) were
197 collected during the injection event and through the sampling ports (Figures 2a and b). Injection took
198 place at 4.5–7.5 m below the water table (corresponding to 21–24 m bgs) in an isolated zone below a
199 packer (Figure 2c). The ambient surface weather conditions during the injection event were 20.4–26.9°C
200 without precipitation. The injection rate was controlled by a submersible and controllable quantitative
201 pump (model MP1, Grundfos, Denmark) at a constant rate of 5.5 m³/d (Figure 2c).

202 **2.3 Real-time monitoring**

203 Real-time monitoring data was collected from 17 May 2017 to 13 October 2017 (Figure 3).
204 Over this period, hydraulic pressure (P), temperature (T) and electrical conductivity (EC) were
205 measured in-situ using the LTC Levellogger Junior (Solinst, Canada) and the barometric state was
206 monitored at the same time using the Barologger Edge (Solinst, Canada) at 10 minute intervals.



207

208 **Figure 3.** ~~Record for monitoring works~~Schedule for water sample collection during the ~~artificial~~-CO₂
209 injection test.

210 **2.4 Water sampling campaign**

211 **2.4.1 Baseline survey period**

212 Water samples were collected using a Watterra Inertial Pump with PowerPack PP-1 (Watterra,
213 Canada) to obtain baseline data before the CO₂ injection. The local baseline of the *p*CO₂ was obtained
214 on two occasions through water sampling between 16 June 2017 and 26 June 2017 (Figure 3). The
215 baseline for the noble gas tracers was determined by a single water-sampling operation on 26 June 2017
216 (Figure 3). Alkalinity was determined in the field site by acid titration method with 0.05 N HNO₃. The
217 pH and temperature were also measured in-situ using a portable water quality meter (YSI ProDSS, YSI
218 Inc./Xylem Inc., USA). The noble gas samples were collected using a standard copper tube of 28 cm³
219 and a pinch-off clamp set.

220 **2.4.2 Injection and post-injection period**

221 Data acquisition after the CO₂ injection was conducted in the same manner as the baseline data
222 collection. Water samples were collected on 19 occasions following the injection event, over 76 days
223 from 27 June 2017 to 12 September 2017 (Figure 3).

224 **2.5 Laboratory analyses**

225 **2.5.1 Noble gas**

226 The noble gas samples were analyzed in the noble gas analysis laboratory at the Korea Polar
227 Research Institute (KOPRI) using an automated system as outlined in Stanley et al. (2009) and Kim et
228 al. (2016). Gases were first extracted from a groundwater sample under high vacuum condition ($\sim 10^{-7}$
229 mbar) and stored in an aluminosilicate glass ampoule (Lott and Jenkins, 1998). Excessive water vapor,
230 active gases, and condensable gases were then removed using cryogenic traps and a series of hot and
231 cold Zr-Al alloy getters (St 101, SAES Getters S.p.A., Italy) before samples injection into the RGA200
232 mass spectrometer (Stanford Research Systems, California, USA) for analysis. The noble gases, He,
233 Ne, Ar, and Kr were calibrated against air standards of 0.9 and 2.7 cm³ STP, to cover the wide range of
234 the tracer enhanced injection water. The discrepancy between duplicate samples was less than 5% (Ju
235 et al., 2019).

236 **2.6 Analytical methods**

237 **2.6.1 *p*CO₂ calculation**

238 *p*CO₂ values for the sampled waters were calculated using the monitored parameters of
239 alkalinity, pH, and temperature. Alkalinity, pH and temperature were measured in-situ. Using these data
240 a robust calculation for *p*CO₂ value was made using the program PHREEQC Version 3 (Parkhurst and
241 Appelo, 2013).

242 **2.6.2 Mass balance model**

243 At the early stage of the CO₂ injection, the CO₂ plume is unstable with a high partial pressure,
244 resulting in a degree of CO₂ degassing. Hence, CO₂ bubbles rise freely from the brine with a proportion
245 of the CO₂ remaining in the dissolved phase. During the degassing period, the free-phase CO₂ strips out

246 the dissolved, relatively insoluble noble gases, especially the lighter elements (He and Ne), leaving the
247 system relatively enriched in the heavier noble gases (Ar, Kr, Xe) (Ballentine et al., 2002; Holland and
248 Gilfillan, 2013). Based on the degree of this enrichment, we can inversely constrain the mass balance
249 of the CO₂ plume in terms of the degassing process (see the Appendix A Mass-mass balance model for
250 detailed explanation).

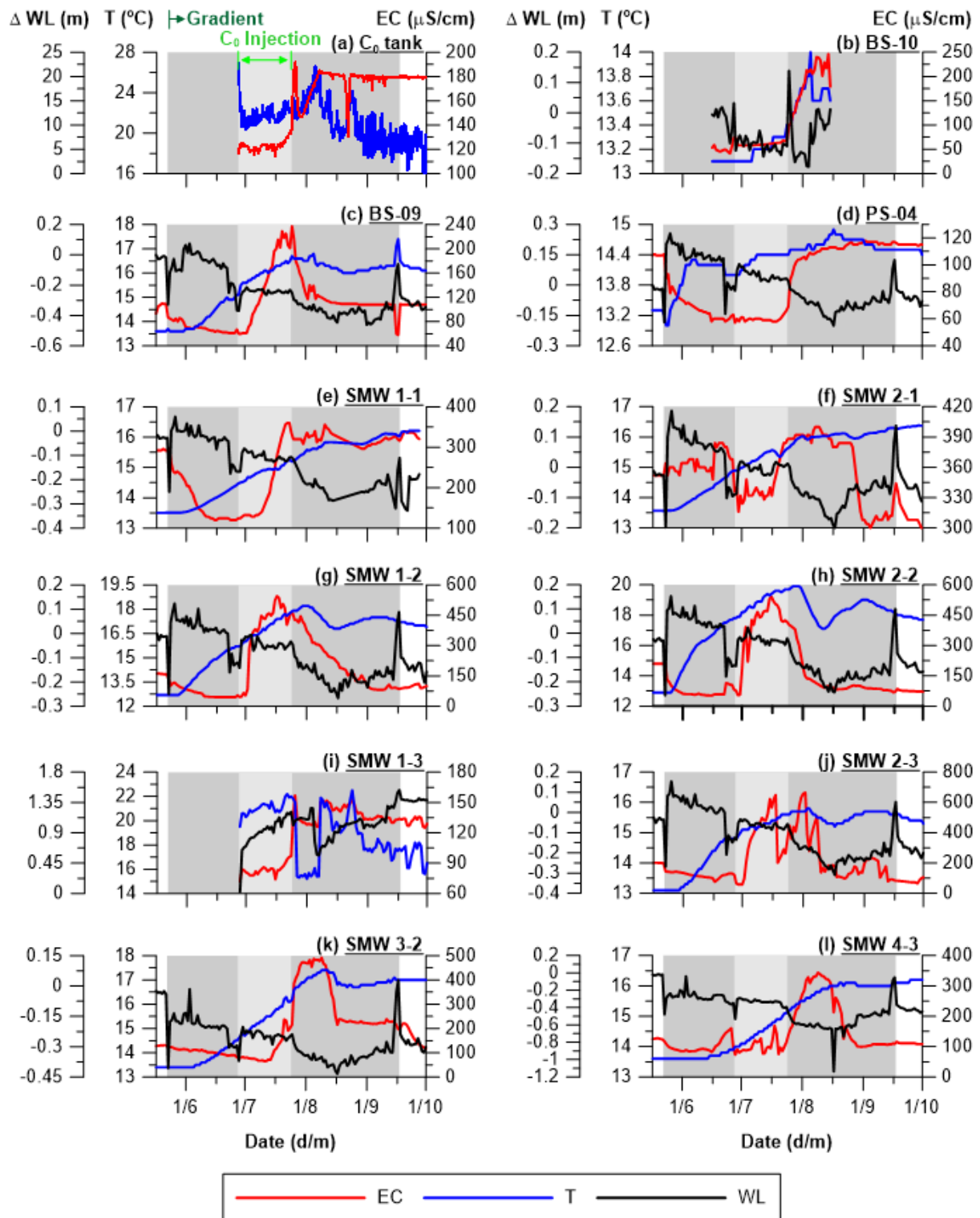
251 **3 Results**

252 **3.1 Prior to CO₂ injection**

253 Pressure and temperature changes result in the degassing of insoluble substances from the
254 groundwater system. At the K-COSEM test site, the groundwater level shows a clear decreasing trend
255 due to large-scale water consumption from nearby industrial complexes (Figure 4) (Ju et al., 2019).
256 However, prior to the experiment the hydrostatic pressure ~~data does not record any irregular turbulence~~
257 ~~prior to the experiment and maintained~~showed a stable correlation with ~~the~~ atmospheric pressure
258 changes and no irregular turbulence (Supplementary Figure S1). Groundwater temperatures
259 corresponded to normal seasonal values ranging between 12.7 to 13.6°C (Figure 4).

260 The induced pressure gradient commenced on the 22 May 2017 as a result of the onset of water
261 circulation (Figure 3c). Perturbations were detected in the water level (WL), temperature (T), and
262 electrical conductivity (EC) values during the initiation of water circulation (see the start points of dark
263 grey zone in Figure 4). The pressure turbulence was most noticeable within the monitoring wells located
264 inside the radius of influence (ROI) area both of the pumping (BS-10) and injection wells (BS-04). For
265 example, PS-04, SMW 1 series and SMW 2 series wells showed an instant pressure increase after the
266 circulation commenced, as they are located near ~~to~~ the injection well (BS-04) (Figure 4d-j). In
267 Contrastinglycontrast, wells SMW 3-2 and 4-3 showed an abrupt decrease in pressure, as a result of
268 their location near to well BS-10 where water was extracted (Figure 4k and l). Well BS-09 also
269 displayed a modest increase in pressure 9 days after water circulation commenced (specifically on 31
270 May 2017) (Figure 4c). Temperature within all monitoring wells showed an overall increase after the
271 water circulation regime started (see the start points of dark grey zone in Figure 4). This is most likely

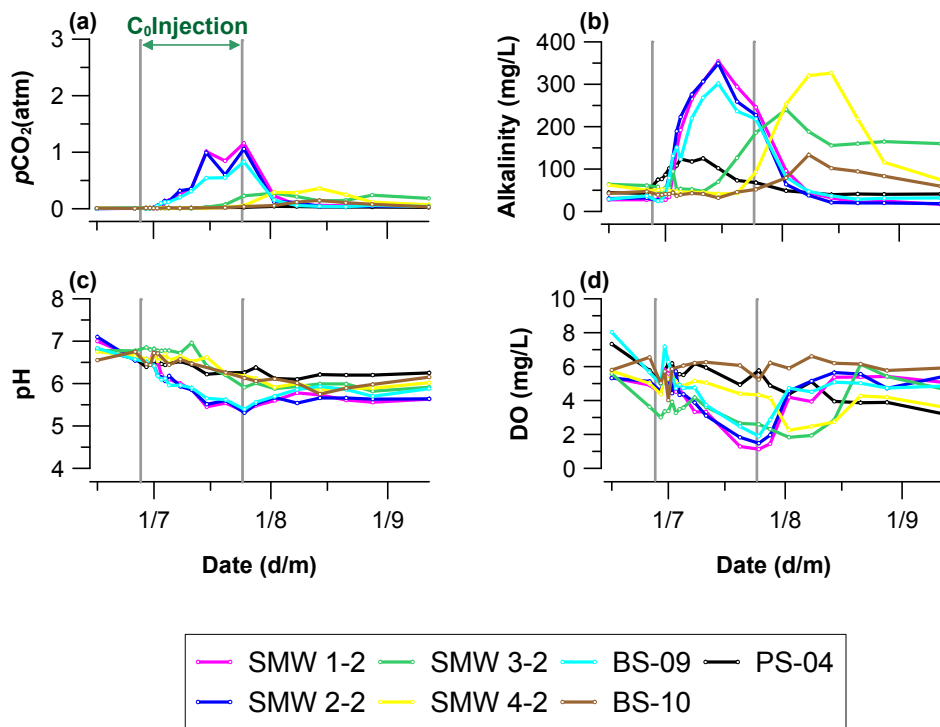
272 linked to the groundwater for injection having resided in the surface tank at temperatures warmer (i.e.,
273 17.1 to 28.6°C) than those of the subsurface groundwaters (i.e., 13.3°C) for the day prior to re-injection
274 into the subsurface. The EC showed the overall decreasing trend in the initial circulation period as the
275 re-injected water (BS-10) has a relatively low EC background compared to the other wells, with the
276 exception of well SMW 2-1 (Figure 4).



277

278 **Figure 4.** Water level (WL), temperature (T) and electrical conductivity (EC) data. Measurements were
 279 completed in the monitoring wells continuously using a LTC data logger. The groundwater circulation
 280 was initiated at 22 May 2017 (dark grey shaded zone) and the CO₂ injection started at 27 June 2017 and
 281 kept going till 24 July 2017 (light grey shaded zone).

282 As outlined previously, two water sampling campaigns were conducted during the circulation
 283 period and prior to CO₂ injection commenced, in order to establish the groundwater baseline
 284 composition (16 June 2017 and 26 June 2017) (Figure 3). The baseline alkalinity values were relatively
 285 low (27.5–64.1 mg/L), DO exhibited a wide variation (3.6–8.0), pH was weakly acidic (6.5–7.1) and
 286 *p*CO₂ was relatively low (0.0–0.01 atm) prior to CO₂ injection (Figure 5). All of the parameters were
 287 close to the baseline values of low carbonate levels in the biotite granite protolith (Ju et al., 2019).



288

289 **Figure 5.** *p*CO₂, pH, alkalinity and DO values. The grey vertical lines represent the injection period.

290 During the water circulation period, pH exhibited an overall decreasing trend as the low-pH
 291 water was pumped out from the down-gradient well (BS-10) and reinjected into the up-gradient well
 292 (BS-04) (Figure 5c). DO also exhibited a decreasing trend as groundwater was re-equilibrated in the
 293 warm surface temperature (17.1–28.6°C) before being injected into the well BS-04 (Figure 4d). *p*CO₂
 294 and alkalinity showed minor variation across the monitored region depending on the groundwater flow
 295 direction and the initial C parameter distributions (Figure 4a and b).

296 Mean He, Ar and Kr concentrations measured before the injection commenced were 5.43×10^{-8}
297 $\text{cm}^3 \text{ STP/g}_{\text{H}_2\text{O}}$, $3.72 \times 10^{-4} \text{ cm}^3 \text{ STP/g}_{\text{H}_2\text{O}}$ and $9.80 \times 10^{-8} \text{ cm}^3 \text{ STP/g}_{\text{H}_2\text{O}}$, respectively. These are close
298 to the Air Saturated Water (ASW) value at the temperature condition (i.e. 13.3°C) of study site—such
299 as $4.58 \times 10^{-8} \text{ cm}^3 \text{ STP/g}_{\text{H}_2\text{O}}$, $3.58 \times 10^{-4} \text{ cm}^3 \text{ STP/g}_{\text{H}_2\text{O}}$ and $8.30 \times 10^{-8} \text{ cm}^3 \text{ STP/g}_{\text{H}_2\text{O}}$ for He, Ar and
300 Kr values, respectively (Kipfer et al., 2002).

301 **3.2 Injection fluid**

302 The gas-infused groundwater was released into the IW from 27 June 2017 to 24 July 2017
303 (Figure 3). The CO_2 -infused groundwater (C_0) collected from the 5 m^3 tank (Figure 2b) was initially
304 below the saturation point (0.40 atm) for 11 days after the injection (29 June 2017 to 8 July 2017), and
305 reached to the over-saturation state ($> 2.3 \text{ atm}$) about 18 days after the injection on 15 July 2017 (Figure
306 5a). This CO_2 variation can be attributed to an accidentally reduced water flux going into the CO_2 tank,
307 causing a decrease of the water level, resulting in altering of the C system balance in CO_2 tank. For the
308 same reason, the pH and DO initially maintained 5.0 and 3.9 mg/L but showed a sudden decrease to 4.2
309 and 0.5 mg/L on the 15 July 2017. Water samples collected from the 1 m^3 tank (C_0) (Figure 2a) were
310 analyzed for their He, Ar and Kr concentrations, and reported at $2.92 \times 10^{-5} \text{ cm}^3 \text{ STP/g}_{\text{H}_2\text{O}}$, $2.26 \times 10^{-}$
311 $^2 \text{ cm}^3 \text{ STP/g}_{\text{H}_2\text{O}}$ and $4.95 \times 10^{-5} \text{ cm}^3 \text{ STP/g}_{\text{H}_2\text{O}}$, respectively. The noble gas concentrations lie between
312 fully saturated and Air Saturated Water (ASW) levels, and thus they will remain dissolved in the
313 groundwater system unless being exposed to low partial pressure conditions such as air bubbles or the
314 vadose zone interface (i.e. water table) (Ju et al., 2019).

315 **3.3 Post injection**

316 **3.3.1 P, T and EC**

317 Pressure turbulence was observed in all monitoring wells prior to the initiation of CO_2 injection
318 (Figure 4), which can be attributed to the change in water volume from $24.0 \text{ m}^3/\text{d}$ to $18.5 \text{ m}^3/\text{d}$ for
319 preparing the gas-infused water of 5.5 m^3 (C_0) before CO_2 injection within the circulation system (see
320 the section 2.2.2 Injection for detailed explanation). Minor changes in temperature were observed inside
321 the Radius of Influence (ROI) zone of IW such as PS-04, BS-09, SMW 1 and SMW 2 (Figure 4c~j).

322 The temperature showed a gradual increase since the groundwater circulation initiated in which the
323 SMW 2-2 showed the highest increase of up to +7.0°C and followed by SMW1-2 (+5.5°C), SMW 3-2
324 (+4.0°C), BS-09 (+3.8°C) and the others (< +2.8°C) (Figure 4). The higher increase in the temperature
325 of BS-09 indicates a preferential flow gradient still exists in the study site even after the formation of
326 the induced pressure gradient (Figure 1a). In EC data, the most prominent signals were recorded at
327 SMW 1-2 (+464 $\mu\text{S}/\text{cm}$, +472%), SMW 2-2 (+447 $\mu\text{S}/\text{cm}$, +368%), SMW 2-3 (+531 $\mu\text{S}/\text{cm}$, +301%),
328 SMW 3-2 (+383 $\mu\text{S}/\text{cm}$, +250%) with the others showing a less pronounced change (< +129%). These
329 observations were consistent with temperature data, exhibiting the greatest change in the SMW #-2
330 wells. This indicated that the CO₂ plume moved horizontally from the injection depth of 21–24 m to the
331 screen depth of SMW #-2 (i.e., 20–22 m) (Figure 1c). The response in EC is clearly different to that of
332 temperature as a notable increase in EC was only observed after CO₂ injection occurred. This is because
333 EC is the function of geochemical interaction between the CO₂ water and the rock materials (Vialle et
334 al., 2014). In the groundwater flow regime, the SMW series wells, BS-09 and BS-10 are located ahead
335 of the migration direction of the IW, which is illustrated by the clearly increasing EC trend (Figure 1b).
336 Alternatively, well PS-04 is located upgradient from the CO₂ injection point, resulting in a gradual
337 lowering of the EC trend after the CO₂ injection was initiated as there is no communication between
338 this well and the CO₂ rich-water (Figure 1b).

339 **3.3.2 $p\text{CO}_2$, pH, alkalinity and DO**

340 As expected, the chemical elements exhibited strong signals correlating with the CO₂ plume
341 arrival. The parameters are presented as breakthrough curves (BTCs) (Figure 5). Note that for the
342 SMWs, the parameters represent the data from the injection depth (i.e., SMW #-2) only, as this
343 generated the largest signals among all depths. The $p\text{CO}_2$ produced the strongest signal at SMW 1-2
344 (+1.15 atm, +25,385%) which was followed by SMW 2-2 (+1.05 atm, +18,067%), BS-09 (+0.82 atm,
345 +12,631%), SWM 4-2 (+0.35 atm, +3,746%) and the others wells (< +2,923%) (Figure 5a). The
346 pronounced response of $p\text{CO}_2$ compared to other parameters is attributed to its low baseline
347 concentration (0.0–0.01 atm) (Risk et al., 2015). Alkalinity also showed significant increases with the
348 arrival of the injected CO₂, particularly in wells SMW 1-2 (+326.4 mg/L, +1,189%), SMW 2-2 (+318.0

349 mg/L, +1,017%), BS-09 (+269.2 mg/L, +821%), SMW 4-2 (+270.0 mg/L, +478%) with other wells
350 showing smaller, but measureable changes (< +286%) (Figure 5b). Alkalinity gradually increases with
351 the chemical interactions between the CO₂ plume and the aquifer materials similar to the EC. The small
352 differences in response to CO₂ injection between EC and alkalinity can be attributed to the geochemical
353 variation of the study site resulting in different CO₂ related buffering capacities (Sechriest, 1960).

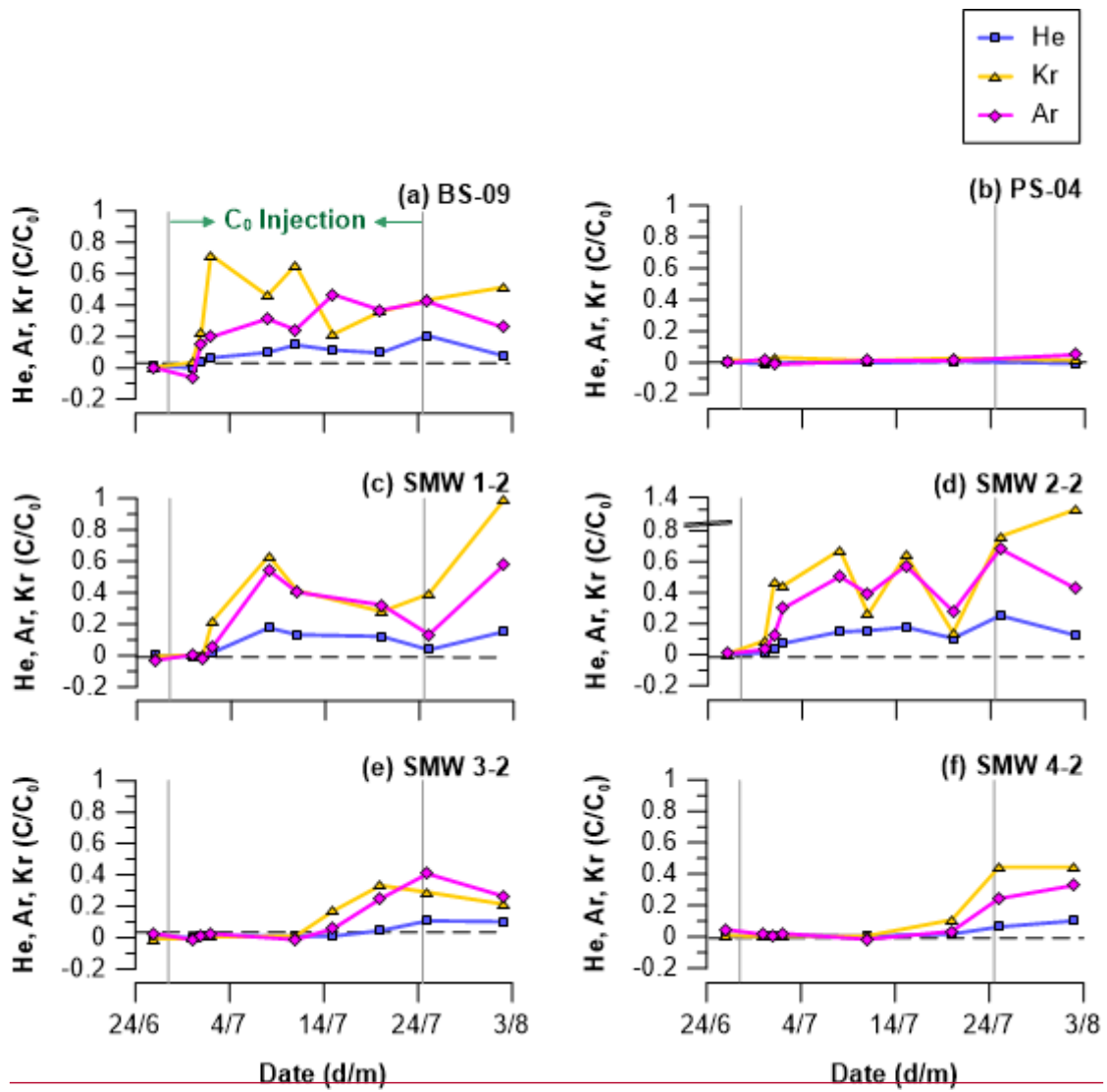
354 The pH also ~~showed-decreased~~ noticeably, changing by -1.5 units at SMW 2-2, which was
355 followed by -1.5 units at SMW 1-2, -1.4 units at SMW 2-3, -1.3 units at BS-09 and > -0.96 units at the
356 others (Figure 5c). The DO showed relatively modest change by up to -4.0 mg/L (-78%) at SMW 1-2
357 which was followed by BS-09 (-4.9 mg/L, -72%), SMW 2-2 (-3.7 mg/L, -72%), SMW 3-2 (-2.8 mg/L,
358 -60%) and the others (< -58%) (Figure 5d). In this experimental setting, the DO evolves with the three-
359 component groundwater mixing between low-DO water volumes (re-injection water at BS-04 and
360 injection water at IW) and high-DO water volume (local groundwater) (Figure 2).

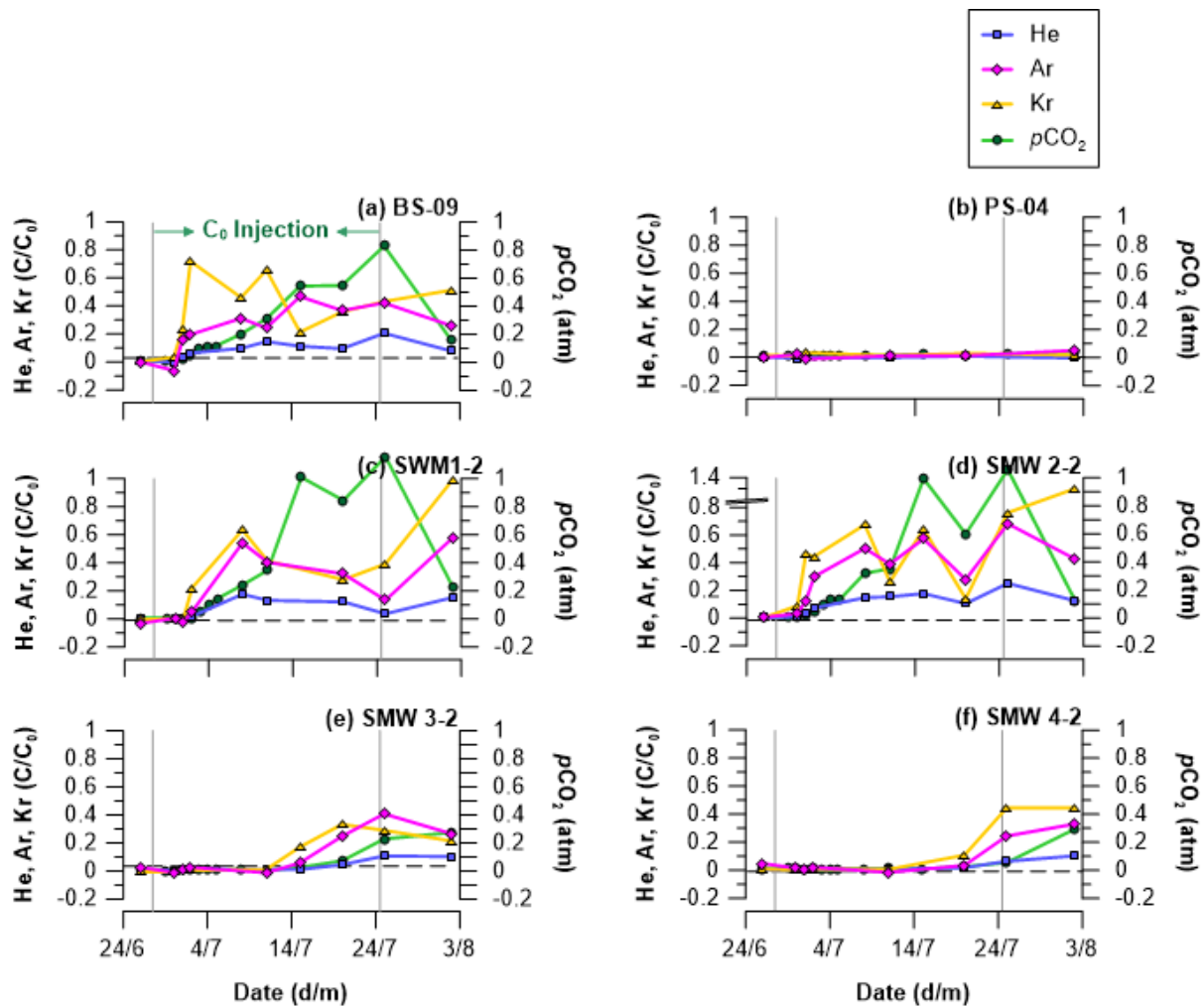
361 3.3.3 Noble gas tracers

362 The measured concentrations of He, Ar and Kr tracers are presented in BTCs (Figure 6). The
363 concentration was normalized to the injection amount (C_0) after the background portion (i.e.
364 atmospheric origin) was subtracted from both monitored (C) and initial concentration (C_0), to simply
365 define the CO₂ arrival as a positive signal. Note that for the SMWs, the parameters present the data
366 from the injection depth (i.e., SMW #-2) only, as this exhibited the largest signals of all depths. As a
367 result, the tracers successfully produced the strong positive signals with the CO₂ plume arrival in the
368 BTCs (Figure 6). The tracer concentrations exhibited variable arrival times and concentrations due to
369 the CO₂ plume following different flow paths within the heterogeneous groundwater system at the site,
370 similar to ~~what was the findings of described by~~ Kilgallon et al. (2018), Lee et al. (2017), Lu et al. (2012)
371 and Stalker et al. (2015). Most importantly, Kr showed the earliest arrivals through all monitoring wells
372 compared to the He and Ar tracer. This was attributed to the Kr taking a less distributed pathway through
373 the subsurface than the other tracers, and a result of the dilution of CO₂ plume along a the concentration
374 gradient (see the discussion section 4.1.2 Diffusion process controlling the efficiency of noble gas

375 tracing).

376 The tracers associated with the CO₂ plume were firstly detected in SMW 2-2 (+4 d) followed
377 by BS-09 (+4 d), SMW 1-2 (+5 d), SMW 3-2 (+18 d) and SMW 4-2 (+23 d) (Figure 6a, c, d, e and f).
378 The strongest signal was recorded at SMW 2-2 (+1,430% for He, +322% for Ar and +6,904% for Kr)
379 suggesting the majority of the CO₂ plume moved along the induced groundwater pressure gradient
380 (Figure 6). A portion of the tracers also moved toward BS-09 and produced a strong signal in spite of
381 ~~its longer being a greater moving~~ distance away from the injection point (5.2 m) than that of SWM 1-1
382 and SMW 2-2 (2.6 m). This can be attributed to the preferential flow path way present in the study site
383 (Figure 1a) (Ju et al., 2019; Lu et al., 2012). Well PS-04 did not record the presence of any tracers
384 during the injection period due to its location behind the IW in the groundwater flow direction (Figure
385 1b). Note It is worth noting that SMW 4-2 ~~showed exhibited a stronger signal a~~ higher concentration of
386 Kr once the tracers arrived at the plateau than SWM 3-2 ~~did~~ (Figure 6), ~~implied implying that~~ a low
387 conductivity zone ~~existing and hindering hinders well~~ the SMW 3-2 from capturing a the full CO₂ plume
388 efficiently. This result was consistent with the observations made in alkalinity and *p*CO₂ (Figure 5).



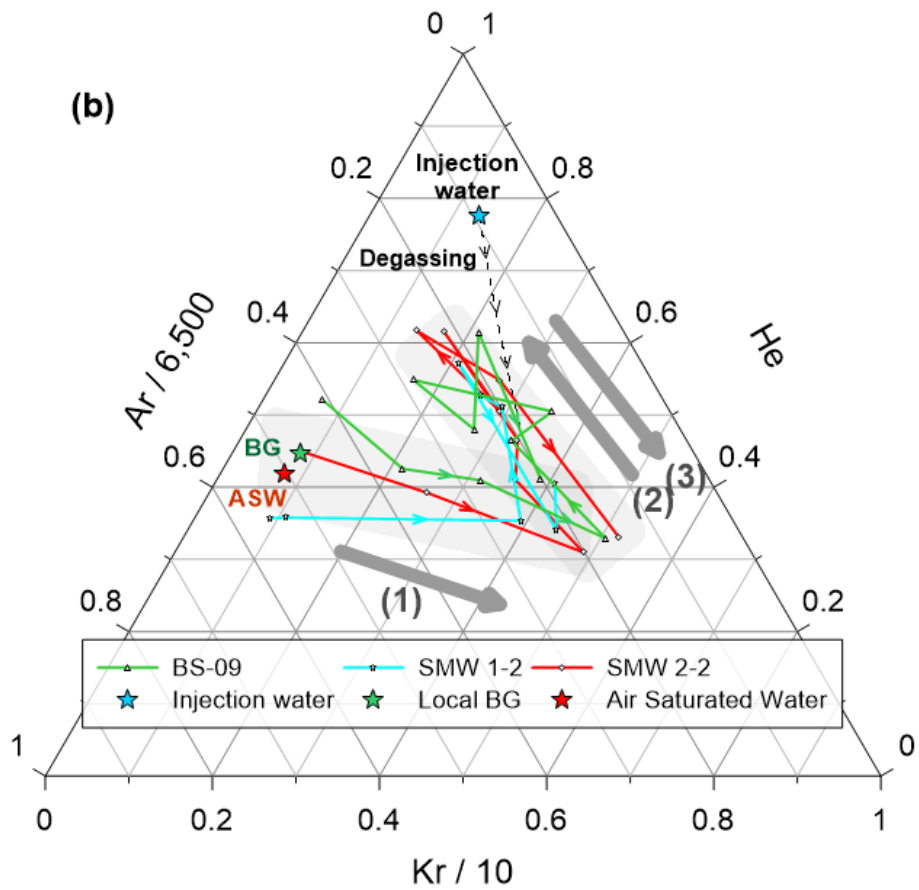
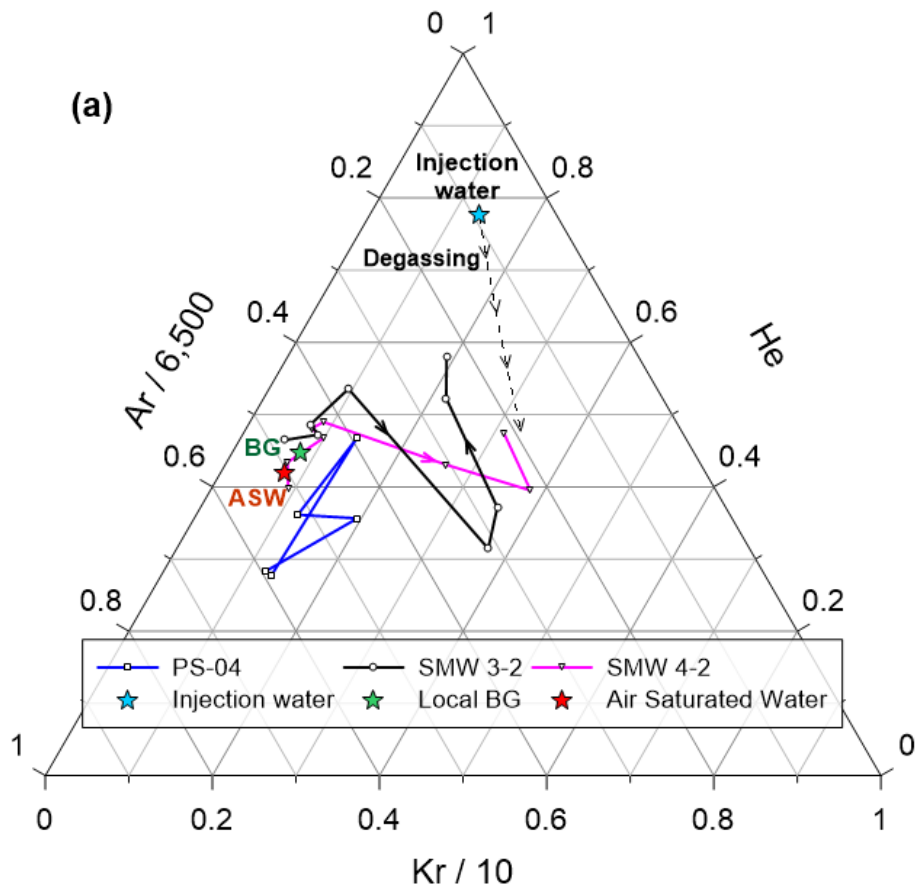


390

391 **Figure 6.** Noble-gas tracer concentration during the experiment. Noble gas was presented as C/C_0 (see
 392 the text for details) with $p\text{CO}_2$. The grey vertical lines show the start and end of the injection period.
 393 The Air Saturated Water (ASW, black dotted horizontal line) was calculated according to Kipfer et al.
 394 (2002) to indicate the local background level of noble gas tracers.

395 As the injection water gradually approached the monitoring network, the observation wells
 396 captured the temporal evolution of the CO_2 plume. In the early stage of BTCs, Kr showed the fastest
 397 arrival time compared to the other tracers for all monitoring wells (Figure 6). This was followed by an
 398 increase in Ar and He concentrations, with both parameters soon reaching their peak concentration
 399 within a few days (Figure 6). In the final stage of BTCs, the plume tail is recorded in all of the
 400 monitoring wells through the decrease of noble gas concentrations resulting after the injection at the
 401 IW ceased. However, it can be observed that the concentration increased in the last stage of the BTCs
 402 for monitoring wells adjacent to IW (Figure 6c and d). This can be attributed to the circulation injection

403 system of this experiment. In the final stage of the injection period (4 days before the end of injection),
404 the tracer-charged plume had reached BS-10 (Figure 4b). As water was still being produced for the
405 reinjection at the IW, a portion of the CO₂ plume was returned back into the injection tank containing
406 the- artificial noble gas tracers. Note that heavier components such as Ar and Kr acted as an early
407 warning tracer for CO₂ arrival in every monitoring well during the monitoring period. This was
408 attributed to physical mechanisms affecting the distribution of the dissolved gases (see the section 4.1.2
409 Diffusion process controlling the efficiency of noble gas tracing).



411 **Figure 7.** Noble gas ternary diagram showing the two groups of wells categorized by their response.
412 (a) monitoring wells which showed no concentration change from background level (i.e., PS-04) or
413 only an early-stage evolution (i.e., SMW 3-2 and SMW 4-2). (b) monitoring wells that showed a three-
414 step evolution as located close to the injection point (i.e., SMW 1-2 and SMW 2-2) and located in a
415 preferential migration path (i.e., BS-09). The early-stage CO₂ plume is characterized by high Kr
416 concentration (Arrow 1), the plume then gradually increases in He and Ar concentrations (Arrow 2). In
417 the final stage, it becomes rich in Kr again, following the cessation of injection (Arrow 3). The peak
418 composition was different from that of injection water due to initial degassing loss.

419 The consistent temporal evolution of the recorded noble gas concentrations within the six
420 monitoring wells is depicted in the ternary diagram of Figure 7. The local BG (i.e., green star) represents
421 the average of background level of individual monitoring wells. Prior to the CO₂ plume arrival, each
422 monitoring well plots near to the Air Saturated Water (ASW) level. The initial arrival of the CO₂ plume
423 was marked by a significant increase in Kr in all monitoring wells (see the arrow 1 in Figure 7) which
424 corresponds to the early stage evolution in the BTCs (Figure 6). Note that PS-04 did not exhibit a
425 response after injection. Following the arrival of the Kr tracer, the He and Ar concentrations within the
426 monitoring wells increase as the plume center approached, converging at a single point (Figure 7).
427 However, the concentrations of noble gas tracers at the peak concentrations were lower than those at
428 the time of injection. They were 73.6–88.3% (He), 26.2–55.5% (Ar), and 0–65.5% (Kr) of the initial
429 concentrations. The lower concentrations can be attributed to the degassing loss of the injection fluid
430 (Sathaye et al., 2016), explained in more detail in the section 4.1.1. This degassing process controls the
431 overall retention amount of the injected CO₂. The composition of the plume tail captured in the
432 monitoring wells was similar to the composition of the plume front, characterized by a high Kr
433 concentration (Figure 7).

434 **3.4 Following injection**

435 ~~The C₀CO₂ injection ceased~~stopped after 28 days ~~of injection~~ (27 June 2017 to 24 July 2017)
436 (Figure 3). This corresponds to the point where the monitoring parameters start to change at the BS-10

437 (Figure 4b and 5). In this moment, the slight increase of EC was also observable in the CO₂ tank as CO₂
438 water re-entered the injection tank (Figure 4a). ~~Accordingly~~ Additionally, -PS-04 also showed a minor
439 increase in EC at the termination period due to the re-circulation of CO₂ injected water (Figure 4d).
440 From this point (24 July 2017), the groundwater circulation system was modified to avoid the re-
441 enhancement of the CO₂ plume. Another local groundwater from BH-03 was prepared and from then
442 onwards substituted the circulation portion going to the BS-04 (Figure 1e and 2c).

443 **3.5 Following groundwater circulation**

444 The groundwater circulation ended on 17 September 2017, 56 days after CO₂ injection stopped
445 and 118 days after groundwater circulation commencement (Figure 3). The pressure turbulence was
446 observable in all monitoring wells (Figure 4) and also EC turbulence was detected in some of the
447 monitoring wells (Figure 4c, f and k), but the groundwater quickly recovered to its previous state (Figure
448 4).

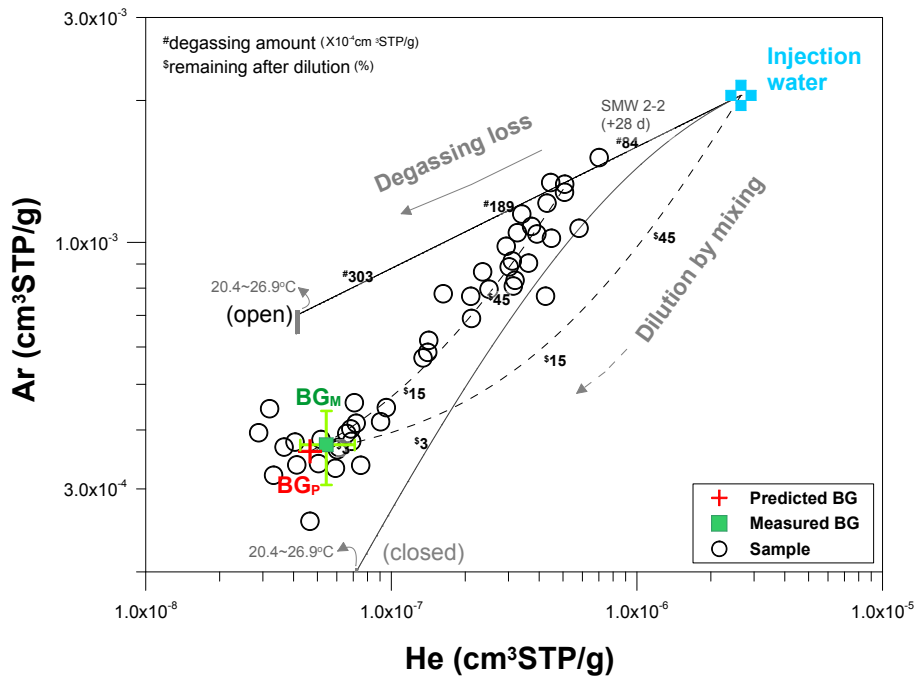
449 **4 Discussion**

450 **4.1 Mass retention mechanisms**

451 **4.1.1 Degassing process controlling the overall retention amount of released CO₂**

452 If an inert tracer is continuously released into the groundwater system, the concentration will
453 gradually increase in monitoring wells and eventually become similar to the composition of injection
454 fluid. In this study, as the tracer-charged water was continuously released into the groundwater system,
455 the monitored concentration was expected to resemble the injection fluid's concentration by the final
456 stage. However, a notable difference in CO₂ and noble gas concentrations was observed between the
457 injection fluid and the plateau points (Figure 7). This phenomenon indicates that tracer mass was not
458 conserved in the groundwater system and suffered from mass-reducing processes. As the noble gas
459 tracer is biochemically inert in the groundwater system, the decrease is likely to be the result of physical
460 processes (Holland and Gilfillan, 2013). For instance, a similar noble gas deficit has been observed in
461 a natural CO₂-rich system, where CO₂ and CH₄ bubbles also stripped out the insoluble gases from the
462 groundwater system (Gilfillan et al., 2008, 2017; Brennwald et al., 2005; Zhou et al., 2005) and in

463 artificial CO₂ injection sites (Nimz and Hudson, 2005; Stalker et al., 2015). Hence, this deficit could be
 464 explained by the degassing of unstable CO₂-rich plume.



465
 466 **Figure 8.** Mass balance of the CO₂ plume depicted with He and Ar tracer. The plume was expected to
 467 follow the mixing line between the injection water (blue cross symbol) and the measured background
 468 concentration (BG_M, green square symbol). Degassing loss of ~~the~~ CO₂ from the dissolved CO₂ plume,
 469 however, would result~~ed~~ in a new mixing line starting from the SMW 2-2 (+28 days) toward the
 470 background concentration (BG_P, red cross symbol). The BG_P was estimated based on the optimization
 471 process of the degassing model (see the Appendix B Model optimization for detailed explanation). The
 472 shaded zone on the degassing models indicates the uncertainty arising from the injection water
 473 temperature (20.4–26.9°C).

474 A diagram was constructed using noble gas tracers to determine the major processes
 475 influencing the CO₂ plume migration (Figure 8). In Figure 8, the concentrations of He and Ar at the
 476 well SMW 2-2 (on 25 July 2017) decreased gradually to their background concentration (BG_P),
 477 indicating mixing of the plume with the local groundwater. The mass distribution of observed samples
 478 was the function of two distinct processes over the testing period: mass reduction of the CO₂ plume
 479 occurred through the degassing process (black line), followed by the dilution of the plume by the local

480 groundwater (black dotted line). The observed data clearly indicated the mixing process was preceded
 481 by the degassing process.

482 **Table 1** Mass balance of the leaked CO₂ plume in shallow aquifer system.

Open system	Injection		After degassing loss			Solubility [†] (mM/atm)
	Amount (kg)	partial pressure (atm)	ΔAmount (kg)	Δpartial pressure (atm)	Remaining (%)	
He	7.04×10^{-5}	3.07×10^{-0}	5.64×10^{-0}	2.46×10^{-0}	80.1 <u>19.9</u>	0.386
Ar	5.43×10^{-0}	6.11×10^{-0}	1.85×10^{-0}	2.08×10^{-0}	34.0 <u>66.0</u>	1.50
Kr	2.50×10^{-0}	7.41×10^{-0}	5.13×10^{-0}	1.52×10^{-0}	20.5 <u>79.5</u>	2.71
CO ₂ p. [‡]	1.70×10^2	6.62×10^{-0}	2.72×10^0	1.07×10^{-0}	1.6 <u>98.4</u>	38.7

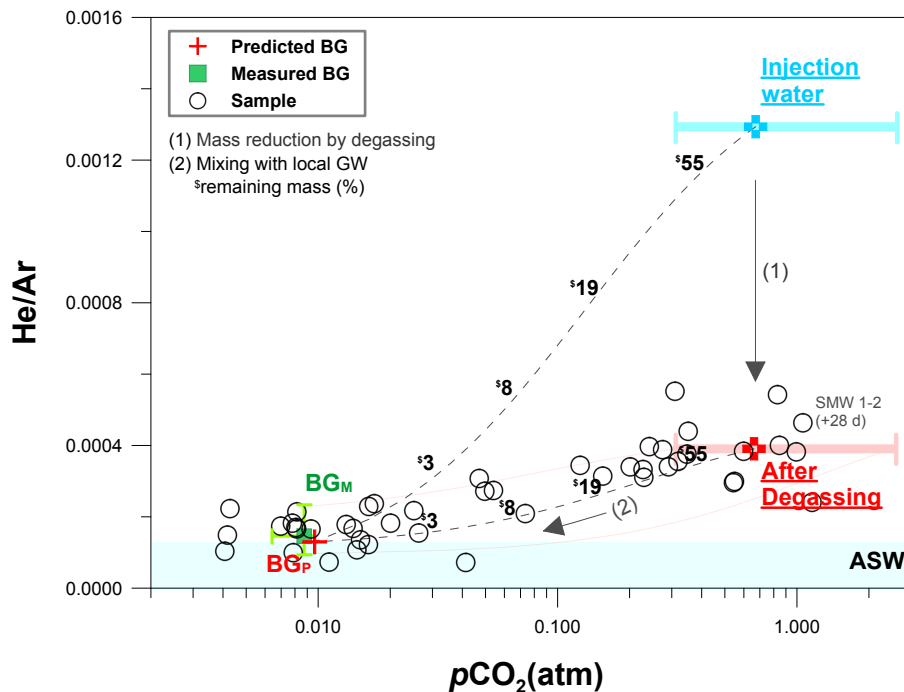
483 [†]NIST chemistry webbook of Sander (2017) at temperature of 21.8°C.

484 ~~the~~The predicted value from model optimization (see the Appendix B Model optimization for detailed
 485 explanation).

486 Elemental fractionation of noble gases is controlled by their differing solubilities and the
 487 ambient reservoir conditions (Figure 8) (Ballentine et al., 2002; Ma et al., 2009). In a closed system,
 488 the dissolved air remains in the groundwater, and equilibrium is achieved between the bubbles and the
 489 surrounding groundwater. In an open system, the air bubbles are mobile after the phase transition and
 490 escape from the aquifer system continuously until the end of the degassing process. In Figure 8, the
 491 mixing line (black dotted line) intersects a degassing line (black line) explaining the loss of air bubbles
 492 by 1.40×10^{-2} cm³/g_{H₂O} through the degassing process in an open system. The analytical technique for
 493 this calculation is shown in Appendix A Mass balance model. In the experiment, CO₂ degassing was
 494 detected just above the water table at the IW reconfirming the initial loss happened into the vadose zone
 495 (Supplementary Figure S2).

496 Unlike noble gases, CO₂ is involved in diverse chemical and biological processes in the
 497 groundwater. To identify the major controls on the CO₂ distribution, the *p*CO₂ was plotted against
 498 measured noble gas tracer concentrations in Figure 9. As expected, the total mass of CO₂ in the plume

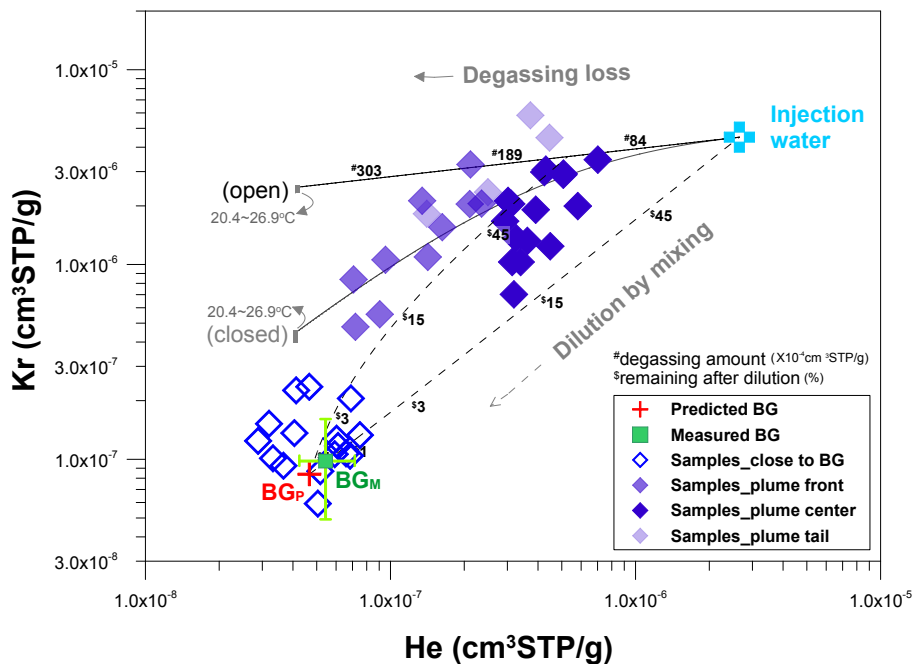
499 was decreased by degassing and mixing processes. Our data designate a clear mixing line stretching
 500 from SMW 1-2 (25 July 2017) to BG_p, indicating that mixing process mainly controlled the mass
 501 distribution of CO₂ in the plume after the initial degassing event. The minor variations from the mixing
 502 trend mostly fall in the ranges of the initial composition of injected CO₂-infused water (Figure 9). The
 503 solubility-controlled process is shown as the black arrow stretching from the blue-cross symbol to red-
 504 cross symbol (Figure 9). The abrupt change in He/Ar ratio stands in strong contrast to the minimal
 505 change observed in the *p*CO₂ during the degassing event (ca. 1.6% overall loss of CO₂). Losses of noble
 506 gases (20.5% for Kr, 34.0% for Ar, and 80.1% for He) are much greater than for CO₂ (Table 1).



507
 508 **Figure 9.** Plot of *p*CO₂ against He/Ar showing the concentration changes of CO₂ and noble gas tracers
 509 during CO₂ plume evolution. The BG_M (green square symbol) is the measured background level, and
 510 the BG_P (red cross symbol) is an estimated value from the optimization process of the degassing model
 511 (see the Appendix B Model optimization for detailed explanation). The CO₂ plume firstly reduces total
 512 mass by the degassing process (Arrow 1) and then gradually gets diluted by mixing with local
 513 groundwater (Arrow 2).

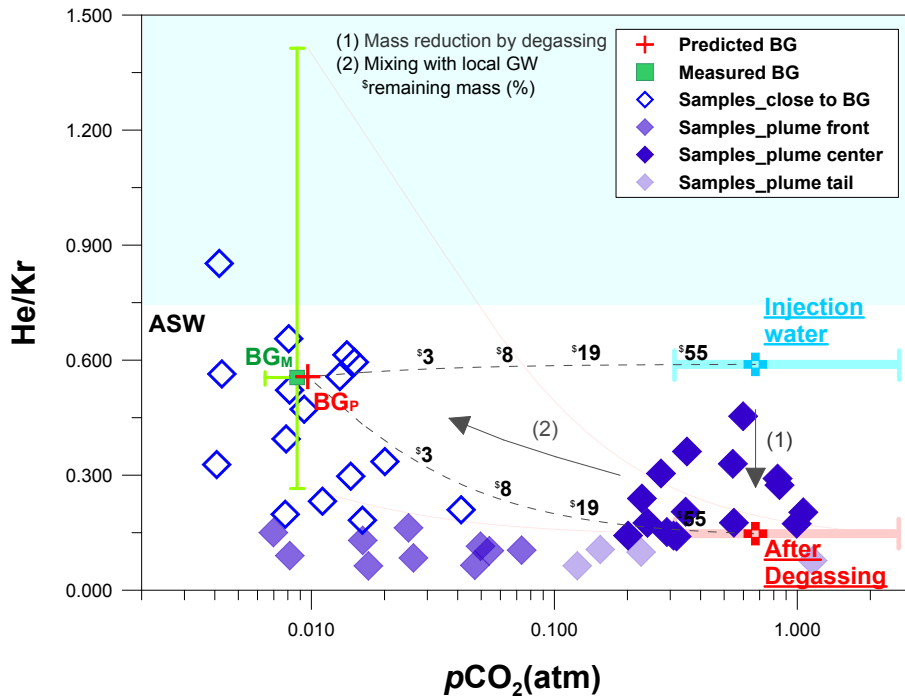
514 **4.1.2 Diffusion process controlling the efficiency of noble gas tracing**

515 The different noble gas species cover a wide mass range and thus may provide a chance to
 516 constrain the mass-dependent processes occurring in the groundwater system. A comparison was made
 517 to scrutinize the behavioral difference for noble gases, as observed from the He/Ar (Figure. 8) and
 518 He/Kr (Figure 10) relationships. The mixing line in Figure 10, represented by a black dotted line
 519 stretching from the degassing line to BGp, corresponds to the mixing line estimated in Figure 8.
 520 However, it is noteworthy that the He and Kr pair did not exhibit a singular trend with many variations
 521 scattering from the estimated mixing line. It is also noteworthy that samples from the plume's center
 522 tend to converge on the estimated mixing line, while the samples from both the plume's front and tail
 523 display a large scatter pattern over the estimated line (Figure 10). Such discordance was also observable
 524 in the $p\text{CO}_2$ versus He/Kr diagram (Figure 11) in which many samples, especially those from the
 525 plume's front and tail had significantly lower He/Kr ratios (around 0.10) than the ratio describing the
 526 estimated mixing line (0.24). This difference indicates that another mass-dependent process was
 527 affecting the tracer distribution in addition to the solubility-controlled process.



528
 529 **Figure 10.** Mass balance of the CO_2 plume depicted with He and Kr tracers. To see the plume evolution
 530 in detail, the samples were sorted by the breakthrough positions. Note that many samples, especially on
 531 the plume front and tail, are scattered over the estimated mixing line, contrary to the He–Ar pair mixing

532 trend in Figure 8.

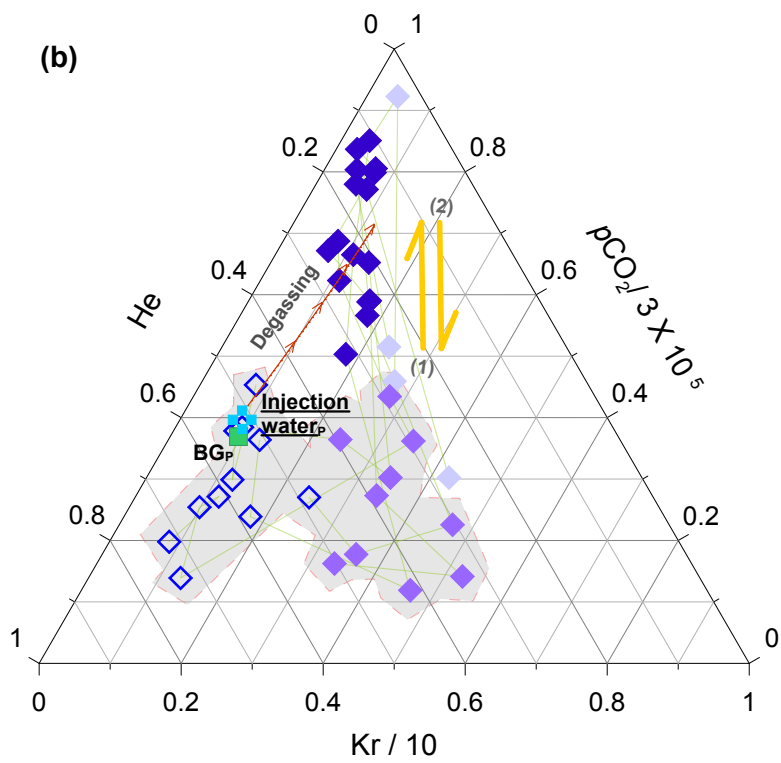
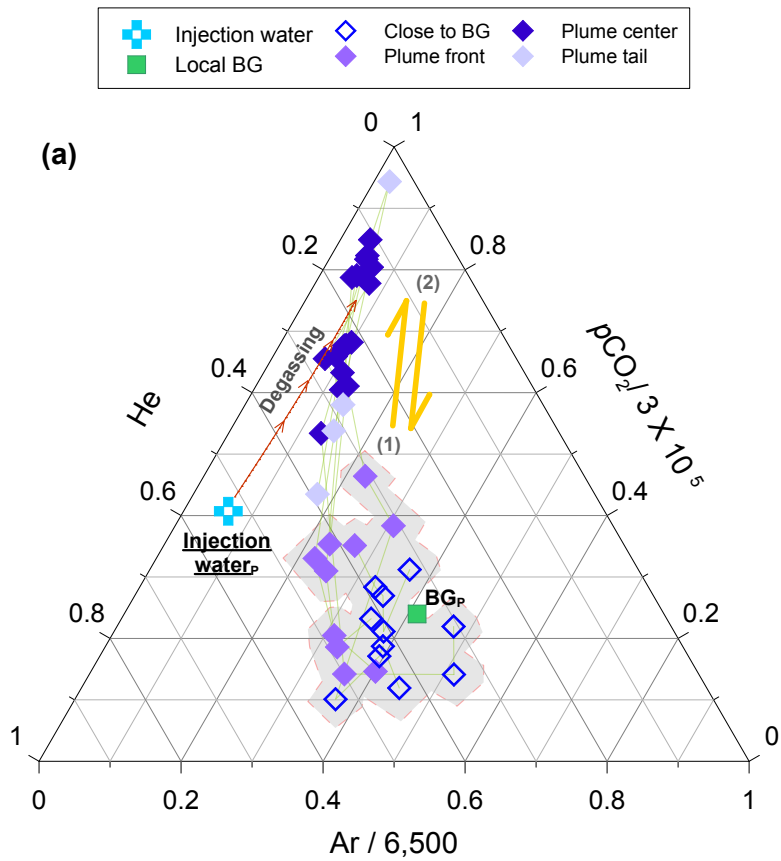


533

534 **Figure 11.** Diagrams showing the concentration changes of CO₂ and noble gas tracers during CO₂
535 plume evolution. To see the plume evolution in detail, the samples were sorted by the breakthrough
536 positions. Note that, many samples, especially on the plume's front and tail, are scattered from the
537 estimated mixing line, as compared to the observations in the pCO₂ versus He/Ar relationship in Figure
538 9.

539 To further examine the temporal progression of the CO₂ plume, ternary plots among of pCO₂
540 He, and Ar or Kr were composed according to the locations of samples in the plume (i.e., front, center,
541 and tail) (Figure 12). In the He/Ar/pCO₂ diagram, the samples have a small variation near BG_p in the
542 initial period, while as the plume center approached the monitoring points, it showed an upward shift
543 toward the degassing point in the Figure 12a. In the He/Kr/pCO₂ diagram, the samples show a much
544 wider variation during the initial stage of the CO₂ plume arrival than the observed change in the
545 He/Ar/pCO₂ diagram (Figure 12b). This difference indicated that another physical process was involved
546 in the mass distribution at the CO₂ plume's front. Note that the initial composition of the plume was
547 characterized by the high concentration of Kr as it appeared firstly in the observation wells (see also

548 Figure 7).



550 **Figure 12.** Ternary diagram showing the compositions of $p\text{CO}_2$, He, and Ar (a) or Kr (b) tracers. To
551 scrutinize the plume evolution, the samples were sorted according to the breakthrough positions. In the
552 initial period of plume evolution, the relative compositional change among $p\text{CO}_2$, He and Kr (b) showed
553 a much wider variation near the background levels (BG_p , green square symbol) than that observed
554 among $p\text{CO}_2$, He and Ar (a), which attributed to the diffusion process (see the text for details). This
555 diffusion-dominant movement was followed by the upward shift toward the degassing point (see Arrow
556 1), as also shown by the intersection point in Figure 8. In the final stage, the samples return to the
557 composition similar to the plume's front (see Arrow 2), after cessation of injection-~~cessation~~.

558 In open water, diffusion is capable of elemental fractionation depending on the molecular mass
559 (Zheng and Bennett, 2002). According to Fick's law, the mass distribution of a solute in a groundwater
560 system is restricted by molecular diffusion along the concentration gradient. In our experimental design,
561 the artificial injection formed a CO_2 - and tracer-rich plume in the groundwater system, setting a steep
562 concentration gradient at the plume boundary. Consequently, the plume boundary was actively
563 subjected to the diffusion process facing with the local groundwater of low concentration level of noble
564 gases. As the diffusion rate is inversely proportional to the elemental mass of the solute, the tracer
565 composition at the plume boundary was regulated by the mass-dependent fractionation. This
566 phenomenon also has been observed in a coal bed methane field, where the free CO_2 and CH_4 gases
567 stripped off the insoluble noble gases from groundwater and this action set the concentration gradient
568 at interfaces with the un-degassed local groundwater, at which diffusion process resulting in a mass
569 dependent fractionation of noble gas tracers (Zhou et al., 2005). Overall, the fact that the diffusion
570 allocates the mass distribution at plume boundary (i.e., plume's front and tail) suggests that the early
571 detection of the migrated CO_2 leaked plume is dependent on this process. This further implies that the
572 early-stage degassing loss is of primary importance in terms of the noble gas tracing efficiency because
573 the degassing process is associated with the overall plume composition including the feature of the
574 concentration gradient at plume front.

575 5 Conclusions

576 A portion of CO₂ stored within the deep subsurface may unintentionally migrate upward to
577 reach overlying shallow aquifers. Whilst noble gas tracers have proved to be useful in monitoring CO₂
578 leakage, they have been rarely adopted for monitoring purposes in the shallow aquifer system. This
579 study utilized the noble gas tracers to indicate the CO₂ leakage and also to elucidate the mass balance
580 of the leaked plume after injection of 1.70 x 10² kg of CO₂ into a shallow aquifer system. The CO₂- and
581 tracer-enhanced groundwater was released into the induced gradient field and subsequent monitoring
582 works have been conducted. The noble gas tracers produced a strong signal ~~withof the -themigrated~~
583 CO₂ leakage, with Kr consistently exhibiting the first arrival time₂ ahead of the CO₂-plume ~~and than~~ the
584 other noble gas tracers throughout all of the monitoring points.

585 The mass distribution of the CO₂ plume was controlled by three different physical processes;⁵
586 solubility-controlled (degassing), physical groundwater mixing and diffusion. The degassing process
587 reduced the overall mass of the CO₂ plume and caused noble gas tracers to be mass-dependently
588 fractionated, which occurred at the initial stage of CO₂ leakage before plume migration. The diffusion
589 process was also involved during the plume migration, but only influenced the noble gas distributions
590 in the leaked plume and did not act as a primary control for the CO₂ distribution within the monitoring
591 period. This phenomenon, however, can accelerate the dilution of artificial tracers at the plume front,
592 especially for the lighter elements, suggesting this process has an important control on the monitoring
593 efficiency of the artificial tracers in terms of early detection of CO₂ leakage. Most importantly, as the
594 noble gas tracers display more apparent changes according to the retention mechanisms than CO₂ itself,
595 ~~noble gas tracers~~they can provide a robust system for precisely monitoring both the fate and pathway
596 taken by the migrating CO₂.

597 Noble gas tracers were used to ~~explain-constrain~~ the physical retention ~~mechanisms of the~~
598 ~~injected CO₂ of-within a~~ shallow aquifer ~~for the leaked CO₂. Our findings indicate that A~~around the
599 ~~injectionleak~~ point, CO₂ degassing dominantly ~~occurred-occurs~~ from ~~a-the~~ dissolved plume ~~ofdue to the~~
600 ~~highthe high~~ gas pressure, suggesting a near-surface monitoring network is necessary for capturing the
601 active “vertical” movement of degassed budget in this area. This can be accomplished by performing a

602 continuous monitoring of CO₂ at the vadose zone, for example by a soil flux measure, soil gas sampling
603 and borehole head space sampling around a potential leak point. The monitoring regime can be
604 performed cost-effectively with limiting a “degassing boundary” around a suspected leak point. In this
605 study, only a few meters away from the leak point (>2.6 m), the degassing behavior was greatly
606 diminished as a gas pressure of CO₂ plume reduced significantly. From this point, the CO₂ plume was
607 stabilized as a dissolved phase and dominantly diluted by mixing with a local groundwater along a flow
608 direction. Therefore, from this stage, sparse monitoring of saturated zone is recommended for tracing
609 down a horizontal migration of a dissolved CO₂ plume, rather than an intensive gas monitoring for a
610 degassed component. Hence, the key aspect to establish an effective monitoring network is how well
611 constrained the “CO₂ degassing boundary” around a potential leak point is, and how well the
612 groundwater flow regime is understood.

613 Monitoring of degassed CO₂ might not be easily achieved in a real CCS field using direct
614 measurements. In this study, the degassing boundary was just a few meters ~~apart from a~~ the leak point
615 (<2.6 m), whilst a strong artificial gradient (~0.18) was enforced for the plume migration. This suggests
616 that a degassing boundary would be even narrower in a natural gradient system, making a direct
617 detection of this extremely difficult. Furthermore, heterogeneity in the vadose zone can put an additional
618 uncertainty in monitoring of the vertical flux, as ~~gaseous~~ gaseous CO₂ can take various pathways in the
619 vadose zone depending on a ~~the~~ soil permeability distribution (Cohen et al., 2013). Hence, identification
620 of a point source of CO₂ leakage using a direct measurement technique in the vadose zone would be
621 very difficult, unless an intensive monitoring is undertaken around the exact point source. However,
622 noble gas monitoring of groundwater is able to record the migration of a CO₂ plume from the leak point
623 along the groundwater flow pathway, as highlighted in this study. Our findings are similar to previous
624 work (Mackintosh and Ballentine, 2012) that showed monitoring of noble gases in groundwater is an
625 order of magnitude more sensitive for detecting migrated gases than vadose zone gas monitoring.
626 Therefore, we recommend that monitoring of noble gases in groundwaters should be used in addition
627 to direct vadose zone methods, in order to increase the sensitivity of the monitoring regime and improve
628 the protection of the shallow groundwater aquifer above a storage site.

629 **Acknowledgements**

630 This research was supported by a Korea Environmental Industry & Technology Institute (KEITI) [grant](#)
631 entitled “R&D Project on Environmental Management of Geologic CO2 Storage” (Project Number:
632 2018001810002), by a Korea Polar Research Institute grant (PE19060) and by a National Research
633 Foundation of Korea (NRF) grant funded by the Korean government (MSIT) (No. 0409-20190119). We
634 thank all the members of the K-COSEM team and, appreciate Intae Kim and Minjung Kim for their
635 efforts and support on noble gas analysis. Also, we appreciate the help of Dr. Stan E. Beaubien in
636 interpreting the noble gas data. Finally, the authors would like to thank two anonymous reviewers for
637 their detailed comments and observations which greatly improved the present paper.

639 **Appendix A. Mass balance model**

640 At least, two noble gases of different solubility are necessary to determine the degassed mass
 641 as outlined in Ju et al. (2019). The closed system is a one-step phase-partitioning process, and therefore,
 642 the degassed amount can be determined just by repeatedly adjusting the gas/liquid ratio until the result

643 $\left(\frac{A}{B}\right)_{(l)}$ fits into the measured data:

644
$$\left(\frac{A}{B}\right)_{(g)} = \left(\frac{A}{B}\right)_{(l)} \times \alpha$$

645
$$\alpha = \frac{\frac{r_A}{\phi_A} K_A}{\frac{r_B}{\phi_B} K_B}$$

646 Here:

647 $\left(\frac{A}{B}\right)_{(g)}$ = A and B ratio in exsolved bubbles, where A and B are different noble gases

648 $\left(\frac{A}{B}\right)_{(l)}$ = the composition of A and B remaining in the dissolved phase

649 α = partitioning coefficient for gas/liquid system

650 K_A, K_B = Henry's constant for A and B, from Sander et al., (2017)

651 r_A, r_B = dissolved-phase activity coefficients for A and B and

652 ϕ_A, ϕ_B = gas-phase fugacity coefficients for A and B.

653 In open system, the CO₂ bubble ($V_{(g)}$) is continuously lost into vadose zone carrying the noble
 654 gas tracers with it from the groundwater system until the plume is stabilized. An iteration calculation
 655 can be undertaken to account for the continuous loss and which terminates when the resultant mass (
 656 $m_{(l)}^i$) fits the observed noble gas data:

657
$$m_{A(l)}^i = m_{A(l)}^{i-1} - m_{A(g)}^{i-1}$$

658
$$m_{B(l)}^i = m_{B(l)}^{i-1} - m_{B(g)}^{i-1}$$

659 Here:

660 i = Iteration step

661 $m_{(l)}^{i-1}$ = mass in dissolved phase before $i - 1^{th}$ degassing loss (g)

662 $m_{(l)}^i$ = mass in dissolved phase after $i - 1^{th}$ degassing loss (g)

663 $m_{(g)}^{i-1}$ = degassed mass during $i - 1^{th}$ degassing process (g)

664 and degassed mass was determined from the degassed volume, such that:

$$665 \quad m_{(g)}^{i-1} = C(V_{(g)} \times p^{i-1})$$

$$666 \quad C = M/R \cdot T$$

$$667 \quad p^{i-1} = \gamma K x^{i-1}/\Phi$$

$$668 \quad x^{i-1} = 18 [NG]^{i-1} (\rho_{(l)} V_{(l)})^{-1}$$

669 Here:

670 $V_{(g)}$ = degassed volume during $i - 1^{th}$ degassing process (cc)

671 C = conversion factor from volume to mass

672 M = molar mass (g/mol)

673 R = gas constant (8.314 cc · atm/K/mol)

674 T = temperature (K)

675 p^{i-1} = partial pressure of removed noble gas during $i - 1^{th}$ degassing process

676 K = Henry's constant in units of pressure (atm)

677 γ = liquid-phase activity coefficient

678 Φ = gas-phase fugacity coefficient

679 x^{i-1} = molar fraction of noble gas in dissolved phase at $i - 1^{th}$ degassing moment ($mol_{NG}/mol_{(l)}$)

680 $[NG]^{i-1}$ = number of moles in dissolved phase at $i - 1^{th}$ degassing moment (mol)

681 $\rho_{(l)}$ = density of dissolved phase (g/cm^3)

682 $V_{(l)}$ = volume of dissolved phase (cm^3)

683 For an open system, an iterative model was used with a fixed $V_{(g)}$ value which should be small enough
684 to finally achieve convergence with the measured noble gas composition. The noble gas concentration
685 in the groundwater was gradually decreased in iterative steps. In the final stage ($i = n$), $\frac{m_A^n}{m_B^n}$ was
686 matched against the monitored composition, and then the total degassed volume was calculated by
687 multiplication of the bubble size ($V_{(g)}$) and the number of iteration steps (i) in the open system model.

688 **Appendix B. Model optimization**

689 Model optimization can be achieved in a similar manner to that used by Ballentine (1997) and
690 Castro et al. (2009). The optimization aims to replicate the monitored noble gas data into a calculated
691 mixing line with the smallest misfit to the observed data. As the monitored concentration is defined by
692 mixing between two end-members, therefore, to achieve the minimum misfit, the end-members
693 constituting the predicted mixing line were repeatedly updated. There are two end-members for the
694 mixing line such as: 1) the noble gas concentration after the degassing event; and 2) the noble gas
695 concentration of the background concentration (Supplementary Figure S3). The first end-member is the
696 function of the initial amount and total degassed budget ($V_{(g)}$) of a species as discussed in the previous
697 section. The second end-member is the function of excess air intrusion level (A) to the Air Saturated
698 Water (ASW) (Mazor and Bosch, 1987; Kipfer et al., 2002). Hence, this optimization process allows
699 quantification of the degassing amount and the background level of leaked plume within the
700 groundwater system. The optimization process is given by:

701

702
$$\chi^2 = \sum_{i=1}^N \left[\left(\frac{NG1_i^m - NG1_i^p}{\sigma_{NG1,i}} \right)^2 + \left(\frac{NG2_i^m - NG2_i^p}{\sigma_{NG2,i}} \right)^2 \right]$$

703 Here:

704 $i = i^{\text{th}}$ sample

705 $N =$ the number of sample

706 $\sigma =$ error of the observed data

707 $NG1^m =$ measured value of noble gas sample

708 $NG1^p =$ predicted value of noble gas sample from the arbitrary mixing line

709 This optimization process was conducted using a code compatible with the Matlab program.

710

711 **References**

712 Alcalde, J., Flude, S., Wilkinson, M., Johnson, G., Edlmann, K., Bond, C.E., Scott, V.,
713 Gilfillan, S.M.V., Ogaya, X., Haszeldine, R.S., 2018. Estimating geological CO₂ storage security to
714 deliver on climate mitigation. *Nat. Commun.* 9(1), 2201. <https://doi.org/10.1038/s41467-018-04423-1>.

715 Ballentine, C.J., 1997. Resolving the mantle He/Ne and crustal ²¹Ne/²²Ne in well gases. *Earth*
716 *Planet Sci. Lett.* 152(1-4), 233–249. [https://doi.org/10.1016/S0012-821X\(97\)00142-8](https://doi.org/10.1016/S0012-821X(97)00142-8).

717 Ballentine, C.J., Burgess, R., Marty, B., 2002. Tracing fluid origin, transport and interaction
718 in the crust. *Rev. Mineral. Geochem.* 47(1), 539–614.

719 Ballentine, C.J., O'nions, R.K., Oxburgh, E.R., Horvath, F., Deak, J., 1991. Rare gas
720 constraints on hydrocarbon accumulation, crustal degassing and groundwater flow in the Pannonian
721 Basin. *Earth Planet Sci. Lett.* 105(1-3), 229–246. [https://doi.org/10.1016/0012-821X\(91\)90133-3](https://doi.org/10.1016/0012-821X(91)90133-3).

722 Ballentine, C.J., Schoell, M., Coleman, D., Cain, B.A., 2001. 300-Myr-old magmatic CO₂ in
723 natural gas reservoirs of the west Texas Permian basin. *Nature* 409(6818), 327.
724 <https://doi.org/10.1038/35053046>.

725 Beaubien, S.E., Bigi, S., Lombardi, S., Sacco, P., and Tartarello, M.C., 2014. Groundwater
726 changes caused by flow through naturally occurring gas (±water) leakage points. 4th EAGE CO₂
727 Geological Storage Workshop 2014; Stavanger; Norway; April 22–24, 2014.

728 Beaubien, S.E., Jones, D.G., Gal, F., Barkwith, A.K.A.P., Braibant, G., Baubron, J.C., Ciotoli,
729 G., Graziani, S., Lister, T.R., Lombardi, S., Michel, K., Quattrocchi, F., Michel, K., 2013. Monitoring
730 of near-surface gas geochemistry at the Weyburn, Canada, CO₂-EOR site, 2001–2011. *Int. J. Greenh.*
731 *Gas Control* 16, 236–262. <https://doi.org/10.1016/j.ijggc.2013.01.013>.

732 Brennwald, M.S., Kipfer, R., Imboden, D.M., 2005. Release of gas bubbles from lake sediment
733 traced by noble gas isotopes in the sediment pore water. *Earth Planet Sci. Lett.* 235(1–2), 31–44.
734 <https://doi.org/10.1016/j.epsl.2005.03.004>.

735 Castro, M.C., Ma, L., Hall, C.M., 2009. A primordial, solar He–Ne signature in crustal fluids
736 of a stable continental region. *Earth Planet Sci. Lett.* 279(3–4), 174–184.
737 <https://doi.org/10.1016/j.epsl.2008.12.042>.

738 Cohen, G., Loisy, C., Laveuf, C., Le Roux, O., Delaplace, P., Magnier, C., Rouchon, V., Garcia,
739 B., Cerepi, A., 2013. The CO₂-Vadose project: Experimental study and modelling of CO₂ induced
740 leakage and tracers associated in the carbonate vadose zone. *Int. J. Greenh. Gas Control* 14, 128–140.
741 <https://doi.org/10.1016/j.ijggc.2013.01.008>.

742 Flude, S., Györe, D., Stuart, F.M., Zurakowska, M., Boyce, A.J., Haszeldine, R.S.,
743 Chalaturnyk, R., Gilfillan, S.M.V., 2017. The inherent tracer fingerprint of captured CO₂. *Int. J. Greenh.*
744 *Gas Control* 65, 40–54. <https://doi.org/10.1016/j.ijggc.2017.08.010>.

745 Flude, S., Johnson, G., Gilfillan, S.M., Haszeldine, R.S., 2016. Inherent tracers for carbon
746 capture and storage in sedimentary formations: composition and applications. *Environ. Sci. Technol.*
747 50(15), 7939–7955. <https://doi.org/10.1021/acs.est.6b01548>.

748 Gilfillan, S.M.V., Ballentine, C.J., Holland, G., Blagburn, D., Sherwood Lollar, B., Scott, S.,
749 Schoell, M., Cassidy, M., 2008. The noble gas geochemistry of natural CO₂ gas reservoirs from the
750 Colorado Plateau and Rocky Mountain provinces, USA. *Geochim. Cosmochim. Acta* 72, 1174–1198.
751 <https://doi.org/10.1016/j.gca.2007.10.009>.

752 Gilfillan, S.M.V., Haszeldine, S., Stuart, F., Gyore, D., Kilgallon, R., Wilkinson, M., 2014.
753 The application of noble gases and carbon stable isotopes in tracing the fate, migration and storage of
754 CO₂. *Energy Procedia* 63, 4123–4133. <https://doi.org/10.1016/j.egypro.2014.11.443>.

755 Gilfillan, S.M.V., Lollar, B.S., Holland, G., Blagburn, D., Stevens, S., Schoell, M., Cassidy,
756 M., Ding, Z., Zhou, Z., Lacrampe-Couloume, G., Ballentine, C.J., 2009. Solubility trapping in
757 formation water as dominant CO₂ sink in natural gas fields. *Nature* 458(7238), 614.
758 <https://doi.org/10.1016/j.gca.2007.10.009>.

759 Gilfillan, S.M.V., Sherk, G.W., Poreda, R.J., Haszeldine, R.S., 2017. Using noble gas

760 fingerprints at the Kerr Farm to assess CO₂ leakage allegations linked to the Weyburn-Midale CO₂
761 monitoring and storage project. *Int. J. Greenh. Gas Control* 63, 215–225.
762 <https://doi.org/10.1016/j.ijggc.2017.05.015>.

763 Gilfillan, S.M.V., Wilkinson, M., Haszeldine, R.S., Shipton, Z.K., Nelson, S.T., Poreda, R.J.,
764 2011. He and Ne as tracers of natural CO₂ migration up a fault from a deep reservoir. *Int. J. Greenh.*
765 *Gas Control* 5(6), 1507–1516. <https://doi.org/10.1016/j.ijggc.2011.08.008>.

766 Harvey, O.R., Qafoku, N.P., Cantrell, K.J., Lee, G., Amonette, J.E., Brown, C.F., 2012.
767 Geochemical implications of gas leakage associated with geologic CO₂ storage. *Crit Rev. Environ. Sci.*
768 *Technol.* 47(1), 23–36. <https://doi.org/10.1021/es3029457>.

769 Holland, G., Gilfillan, S., 2013. Application of noble gases to the viability of CO₂ storage. In
770 : Burnard, P. (Eds), *The Noble Gases as Geochemical Tracers. Advances in Isotope Geochemistry*,
771 Springer, Berlin, Heidelberg 177–223. https://doi.org/10.1007/978-3-642-28836-4_8.

772 Ide, S.T., Friedmann, S.J., Herzog, H.J., 2006. CO₂ leakage through existing wells: current
773 technology and regulations. In *8th International Conference on Greenhouse Gas Control Technologies*,
774 19–22.

775 IEAGHG, 2011. *Potential Impacts on Groundwater Resources of CO₂ Storage*. IEAGHG,
776 Cheltenham, UK.

777 IPCC, 2005. *Intergovernmental Panel on Climate Change. Special Report on CO₂ Capture*
778 *and Storage*, edited, pp. 208–210.

779 Ju, Y., Beaubien, S.E., Lee, S.S., Kaown, D., Hahm, D., Lee, S., Park, I.W., Park, K., Yun,
780 S.T., Lee, K.K., 2019. Application of natural and artificial tracers to constrain CO₂ leakage and
781 degassing in the K-COSEM site, South Korea. *Int. J. of Greenh. Gas Control* 86, 211–225.
782 <https://doi.org/10.1016/j.ijggc.2019.05.002>.

783 Ju, Y., Kaown, D., Lee, K.K., 2018a. A three-pronged approach for identifying source and

784 extent of nitrate contamination in groundwater. *J. Soil Water Conserv.* 73(5), 493–503.
785 <https://doi.org/10.2489/jswc.73.5.493>.

786 Ju, Y., Lee, S.S., Kaown, D., Lee, K.K., 2018b. Application of Inert Gas Tracers to Identify the
787 Physical Processes Governing the Mass Balance Problem of Leaking CO₂ in Shallow Groundwater
788 System. 14th Greenhouse Gas Control Technologies Conference; Melbourne; Australia; October 21–
789 26. https://papers.ssrn.com/sol3/papers.cfm?abstract_id=3365686.

790 Kilgallon, R., Gilfillan, S.M.V., Edlmann, K., McDermott, C.I., Naylor, M., Haszeldine, R.S.,
791 2018. Experimental determination of noble gases and SF₆, as tracers of CO₂ flow through porous
792 sandstone. *Chem. Geol.* 480, 93–104. <https://doi.org/10.1016/j.chemgeo.2017.09.022>.

793 Kim, I., Hahm, D., Rhee, T.S., Kim, T.W., Kim, C.S., Lee, S., 2016. The distribution of glacial
794 meltwater in the Amundsen Sea, Antarctica, revealed by dissolved helium and neon. *J. Geophys. Res.:*
795 *Oceans* 121(3), 1654–1666. <https://doi.org/10.1002/2015JC011211>.

796 Kipfer, R., Aeschbach-Hertig, W., Peeters, F., Stute, M., 2002. Noble gases in lakes and
797 ground waters. *Rev. Mineral. Geochem.* 47(1), 615–700. <https://doi.org/10.2138/rmg.2002.47.14>.

798 LaForce, T., Ennis-King, J., Boreham, C., Paterson, L., 2014. Residual CO₂ saturation estimate
799 using noble gas tracers in a single-well field test: the CO₂CRC Otway project. *Int. J. Greenh. Gas*
800 *Control* 26, 9–21. <https://doi.org/10.1016/j.ijggc.2014.04.009>.

801 Lee, K.K., Lee, S.H., Yun, S.T., Jeon, S.W., 2016. Shallow groundwater system monitoring
802 on controlled CO₂ release sites: a review on field experimental methods and efforts for CO₂ leakage
803 detection. *Geosci. J.* 20(4), 569–583. <https://doi.org/10.1007/s12303-015-0060-z>.

804 Lee, S.S., Ju, Y., HA, S.W., Joun, W.T., Jun, S.C., Yun, S.T., Lee, K.K., 2018. Controlled CO₂
805 Injection into a Shallow Aquifer and Leakage Detection Monitoring by Two Different Leakage Events
806 at the K-Cosem Site, Korea. In 14th Greenhouse Gas Control Technologies Conference Melbourne;
807 Australia; October 21–26. https://papers.ssrn.com/sol3/papers.cfm?abstract_id=3366360.

808 Lee, S.S., Kim, H.H., Joun, W.T., Lee, K.K., 2017. Design and Construction of
809 Groundwater Monitoring Network at Shallow-depth CO₂ Injection and Leak Test Site, Korea. *Energy*
810 *Procedia* 114, 3060–3069. <https://doi.org/10.1016/j.egypro.2017.03.1434>.

811 Lemieux, J.M., 2011. The potential impact of underground geological storage of carbon
812 dioxide in deep saline aquifers on shallow groundwater resources. *Hydrogeol. J.* 19(4), 757–778.
813 <https://doi.org/10.1007/s10040-011-0715-4>.

814 Lions, J., Devau, N., De Lary, L., Dupraz, S., Parmentier, M., Gombert, P., Dictor, M.C., 2014.
815 Potential impacts of leakage from CO₂ geological storage on geochemical processes controlling fresh
816 groundwater quality: a review. *Int. J. Greenh. Gas Control* 22, 165–175.
817 <https://doi.org/10.1016/j.ijggc.2013.12.019>.

818 Lollar, B.S., Ballentine, C.J., Onions, R.K., 1997. The fate of mantle-derived carbon in a
819 continental sedimentary basin: integration of C/He relationships and stable isotope signatures. *Geochim.*
820 *Cosmochim. Acta* 61(11), 2295–2307. [https://doi.org/10.1016/S0016-7037\(97\)00083-5](https://doi.org/10.1016/S0016-7037(97)00083-5).

821 Lott, D.E., Jenkins, W.J., 1998. Advances in analysis and shipboard processing of tritium and
822 helium samples. *International WOCE Newsletter*, 30, 27–30.

823 Lu, J., Cook, P.J., Hosseini, S.A., Yang, C., Romanak, K.D., Zhang, T., Freifeld, B.M., Smyth,
824 R.C., Zeng, H., Hovorka, S.D., 2012. Complex fluid flow revealed by monitoring CO₂ injection in a
825 fluvial formation. *J. Geophys. Res. Solid Earth* 117. <https://doi.org/10.1029/2011JB008939>.

826 Ma, L., Castro, M.C., Hall, C.M., 2009. Atmospheric noble gas signatures in deep Michigan
827 Basin brines as indicators of a past thermal event. *Earth Planet Sci. Lett.* 277(1–2), 137–147.
828 <https://doi.org/10.1016/j.epsl.2008.10.015>.

829 Mackintosh, S.J., Ballentine, C.J., 2012. Using ³He/⁴He isotope ratios to identify the source of
830 deep reservoir contributions to shallow fluids and soil gas. *Chem. Geol.* 304–305, 142–150.
831 <https://doi.org/10.1016/j.chemgeo.2012.02.006>.

832 Mazor, E., Bosch, A., 1987. Noble gases in formation fluids from deep sedimentary basins: a

833 review. *Appl. Geochem.* 2(5–6), 621–627. [https://doi.org/10.1016/0883-2927\(87\)90014-X](https://doi.org/10.1016/0883-2927(87)90014-X).

834 Myers, M., Stalker, L., Pejčić, B., Ross, A., 2013. Tracers—Past, present and future applications
835 in CO₂ geosequestration. *Appl. Geochem.* 30, 125–135.
836 <https://doi.org/10.1016/j.apgeochem.2012.06.001>.

837 Nimz, G.J., Hudson, G.B., 2005. The use of noble gas isotopes for monitoring leakage of
838 geologically stored CO₂. In: Thomas, D., Benson, S. (Eds.), *Carbon Dioxide Capture for Storage in*
839 *Deep Geologic Formations* vol. 2. Elsevier Press, Amsterdam 1113–1130.

840 Parkhurst, D.L., Appelo, C.A.J., 2013. Description of input and examples for PHREEQC
841 version 3: a computer program for speciation, batch-reaction, one-dimensional transport, and inverse
842 geochemical calculations (No. 6-A43). US Geological Survey. <https://doi.org/10.3133/tm6A43>.

843 Pinti, D.L., Marty, B., 1995. Noble gases in crude oils from the Paris Basin, France:
844 Implications for the origin of fluids and constraints on oil-water-gas interactions. *Geochim. Cosmochim.*
845 *Acta* 59(16), 3389–3404. [https://doi.org/10.1016/0016-7037\(95\)00213-J](https://doi.org/10.1016/0016-7037(95)00213-J).

846 Rillard, J., Loisy, C., Le Roux, O., Cerepi, A., Garcia, B., Noirez, S., Rouchon, V., Delaplaceb,
847 P., Willequet, O., Bertrand, C., 2015. The DEMO-CO₂ project: A vadose zone CO₂ and tracer leakage
848 field experiment. *Int. J. Greenh. Gas Control* 39, 302–317. <https://doi.org/10.1016/j.ijggc.2015.04.012>.

849 Risk, D., Lavoie, M., Nickerson, N., 2015. Using the Kerr investigations at Weyburn to screen
850 geochemical tracers for near-surface detection and attribution of leakage at CCS/EOR sites. *Int. J.*
851 *Greenh. Gas Control* 35, 13–17. <https://doi.org/10.1016/j.ijggc.2015.01.019>.

852 Sander, R., 2017. Henry's Law Constants. In: Linstrom, P.J., Mallard, W.G. (Eds.), *NIST*
853 *Chemistry WebBook*, NIST Standard Reference Database Number 69. National Institute of Standards
854 and Technology, Gaithersburg MD, 20899. <https://doi.org/10.18434/T4D303>.

855 Sathaye, K.J., Larson, T.E., Hesse, M.A., 2016. Noble gas fractionation during subsurface gas
856 migration. *Earth Planet Sci. Lett.* 450, 1–9. <https://doi.org/10.1016/j.epsl.2016.05.034>.

857 Sechriest, R.E., 1960. Relationship between total alkalinity, conductivity, original pH, and
858 buffer action of natural water. OHIO J. SCI. 60(5), 303.

859 Stalker, L., Boreham, C., Underschultz, J., Freifeld, B., Perkins, E., Schacht, U., Sharma, S.,
860 2009. Geochemical monitoring at the CO2CRC Otway Project: tracer injection and reservoir fluid
861 acquisition. Energy Procedia 1(1), 2119–2125. <https://doi.org/10.1016/j.egypro.2009.01.276>.

862 Stalker, L., Boreham, C., Underschultz, J., Freifeld, B., Perkins, E., Schacht, U., Sharma, S.,
863 2015. Application of tracers to measure, monitor and verify breakthrough of sequestered CO₂ at the
864 CO2CRC Otway Project, Victoria, Australia. Chem. Geol. 399, 2–19.
865 <https://doi.org/10.1016/j.chemgeo.2014.12.006>.

866 Stanley, R.H., Jenkins, W.J., Lott, D.E., Doney, S.C., 2009. Noble gas constraints on air-sea
867 gas exchange and bubble fluxes. J. Geophys. Res.: Oceans 114(C11).
868 <https://doi.org/10.1029/2009JC005396>.

869 Vialle, S., Contraires, S., Zinzsner, B., Clavaud, J.B., Mahiouz, K., Zuddas, P., Zamora, M.,
870 2014. Percolation of CO₂-rich fluids in a limestone sample: Evolution of hydraulic, electrical, chemical,
871 and structural properties. J. Geophys. Res. Solid Earth 119(4), 2828–2847.
872 <https://doi.org/10.1002/2013JB010656>.

873 Zheng, C., Bennett, G.D., 2002. Applied contaminant transport modeling. Wiley-Interscience,
874 New York.

875 Zhou, Z., Ballentine, C.J., Kipfer, R., Schoell, M., Thibodeaux, S., 2005. Noble gas tracing of
876 groundwater/coalbed methane interaction in the San Juan Basin, USA. Geochim. Cosmochim. Acta
877 69(23), 5413–5428. <https://doi.org/10.1016/j.gca.2005.06.027>.

Highlights

- Shallow aquifers are the last trapping zone for a CO₂ migrated from a storage site.
- CO₂ and noble gas tracers were co-injected into a shallow groundwater aquifer.
- Noble gasThe tracers showed a clear relationship to thewith CO₂ species during CO₂after the injection in shallow aquifer.
- Most ofThe released CO₂ was mostly retained in the shallow aquifer rather than lost into the vadoseatmosphere.
- Physical mixing and solubility trapping controls primarily determine the mass retention of migrated released CO₂.
- Shallow aquifer is the last trapping zone for mobile CO₂ that migrates from the deep CO₂ storage.

1 **Application of noble gas tracers to identify the retention mechanisms of CO₂ migrated from a**
2 **deep reservoir into shallow groundwater**

3 YeoJin Ju¹, Stuart M. V. Gilfillan², Seong-Sun Lee¹, Dugin Kaown¹, Doshik Hahm³, Sanghoon Lee¹,
4 In-Woo Park¹, Seung-Wook Ha¹, Keyhong Park⁴, Hyun-Kwon Do⁵, Seong-Taek Yun⁵, Kang-Kun
5 Lee^{1,*}

6 ¹School of Earth and Environmental Sciences, Seoul National University, 1 Gwanak-ro, Gwanak-gu,
7 Seoul, 08826, South Korea.

8 ²School of GeoSciences, The University of Edinburgh, Grant Institute, James Hutton Road, Edinburgh
9 EH9 3FE, UK.

10 ³Department of Oceanography, Pusan National University, Busan, South Korea.

11 ⁴Korea Polar Research Institute, Incheon, South Korea.

12 ⁵Department of Earth and Environmental Sciences, Korea University, Seoul 02841, South Korea.

13 Email: jinee18@snu.ac.kr, stuart.gilfillan@ed.ac.uk, soon3311@snu.ac.kr, dugin1@snu.ac.kr,
14 hahm@pusan.ac.kr, lshlsh2311@snu.ac.kr, inwoo0415@snu.ac.kr, hasabana@snu.ac.kr,
15 keyhongpark@kopri.re.kr, iq1pc@korea.ac.kr, styun@korea.ac.kr.

16 *Corresponding author. Tel.: +82 2 873 3647. E-mail address: kkleee@snu.ac.kr.

17

18 **Abstract**

19 Carbon Capture and Storage (CCS) is a valuable climate-mitigation technology, which offers
20 the potential to cost-effectively reduce the emissions associated with the burning of fossil fuels.
21 However, there is a potential risk of a small portion of the stored CO₂ unintentionally migrating from a
22 storage site to a shallow groundwater aquifer which is the final retaining zone for any migrated CO₂
23 before it escapes to the atmosphere. Hence, it is imperative to identify the physical retention
24 mechanisms of CO₂ within a shallow aquifer. In this study 1.70x10² kg of CO₂ and noble gas tracers
25 (He, Ar and Kr) were continuously injected into a groundwater aquifer over 28 days with the aim of
26 identifying the mechanisms and amount of CO₂ retention. Among the tracers, Kr was found to be the
27 earliest indicator of CO₂ migration. The other tracers – He and Ar – arrived later and exhibited diluted
28 signals. The diluted signals were attributed to degassing of the plume mass (1.6% of CO₂) during the
29 early stages of CO₂ migration. Diffusion accelerated the dilution of the lighter elements at the plume
30 boundaries. Consequently, the clear relation of the noble gases with the CO₂ proved that degassing and
31 mixing primarily control the mass retention of CO₂ in shallow groundwater, and the relative importance
32 of these processes varies along the evolving path of migrating CO₂.

33 **Keywords:** CCS; monitoring; CO₂ leakage; noble gas tracing; artificial tracer; geochemical monitoring

34 **1. Introduction**

35 Carbon Capture and Storage (CCS) is a climate change mitigation technology that comprises
36 the capture of CO₂ from an industrial point source, such as a power plant or refinery, transport of the
37 captured CO₂ to a storage site followed by the injection of the captured CO₂ into deep geological strata
38 for permanent disposal (IPCC, 2005). However, there is a potential risk that a small portion of the
39 mobile CO₂ in a storage site could accidentally migrate out of the subsurface reservoir and inadvertently
40 reach shallower levels of the subsurface (Alcalde et al., 2018). This CO₂ could potentially migrate
41 through geological conduits such as permeable faults and/or abandoned wells resulting in the
42 deterioration of fresh water resources above the CO₂ reservoir (Harvey et al., 2012; IEAGHG, 2011;
43 Lemieux, 2011; Lion et al., 2014) and leakage of a small portion of the CO₂ into the atmosphere (Ide et
44 al., 2006; IPCC, 2005). Recently, the Weyburn-Midale (Canada) CO₂ monitoring and storage project
45 faced allegations that leakage of CO₂ injected into the Weyburn-Midale oil field for Enhanced Oil
46 Recovery (EOR) and storage was causing a deterioration of the groundwater quality on a farm located
47 above the field (Beaubien et al., 2013; Gilfillan et al., 2017).

48 A variety of geochemical tools have been used to verify CO₂ storage security and track the fate
49 of CO₂ injected for storage. These include CO₂ soil gas and groundwater concentrations, stable C and
50 O isotopes within the CO₂, on-site monitoring parameters (pH, alkalinity, ORP, EC, temperature and
51 DO), inert gas tracers, major and trace ions and radiocarbon (¹⁴C) (Flude et al., 2016; Lee et al., 2016).
52 Soil gas and dissolved CO₂ concentrations in groundwater can provide a direct tracer of CO₂ migration,
53 allowing discrimination of different CO₂ origins and providing a means to establish the mass balance
54 of CO₂ present in the groundwater system (Ballentine et al., 2001; Beaubien et al., 2014; Gilfillan et al.,
55 2011; Lollar et al., 1997; Sathaye et al., 2016). Recent developments in on-site monitoring technologies
56 now allow the continuous measurement of a number of parameters (e.g. alkalinity, T, EC, pH) which
57 can be used to establish the overall distribution and temporal evolution of a small CO₂ plume within a
58 shallow groundwater aquifer (Lee et al., 2016). Noble gases are characterized by their inert behavior,
59 which makes them ideal tracers within a subsurface system. This inertness means that noble gases are

60 conservative tracers and do not partake in the chemical reactions that dilute the CO₂ leakage signals and
61 hence are capable of providing a robust means to distinguish between natural and stored CO₂ (Risk et
62 al., 2015).

63 Noble gas tracing techniques have been used to track both the fate and migration pathways of
64 injected CO₂ in reservoirs. Within a typical porous CO₂ storage reservoir, CO₂ is retained by a
65 combination of structural, residual and solubility trapping mechanisms (Alcalde et al., 2018; Holland
66 and Gilfillan, 2013; IPCC, 2005). Recent experiments at the CO₂CRC Otway Demonstration site for
67 CO₂ storage in Australia have used Kr and Xe as conservative tracers to determine the degree of residual
68 trapping within a porous saline formation, using a numerical mass balance approach (LaForce et al.,
69 2014). The degree of solubility trapping has also been determined using noble gases, through
70 identification of the degree of partitioning of the noble gases into groundwater present within the
71 reservoir formations (Ballentine et al., 1991; Brennwald et al., 2005; Gilfillan et al., 2008, 2009; 2014;
72 Pinti and Marty, 1995; Zhou et al., 2005).

73 Noble gas tracers are also suitable for monitoring the vertical migration of the reservoir CO₂,
74 thanks to the compositional difference of natural noble gas tracers between storage reservoir and the
75 near surface environment (Mackintosh and Ballentine, 2012). Gilfillan et al. (2011) applied noble gas
76 tracing tools to constrain the nature of CO₂ leakage into shallow groundwater and surface water bodies.
77 Further work by Gilfillan et al., (2017) used inherent tracers residing in the Weyburn-Midale injection
78 and storage project reservoir to show that CO₂ migration from the deep reservoir into the shallow aquifer
79 system had not occurred. This work found that the noble gas composition in the groundwater samples
80 above the CO₂ injection and storage project did not vary over a typical background level of a shallow
81 aquifer, of Air Saturated Water (ASW) with an excess air component of up to 45% (Gilfillan et al.,
82 2017). Recent work by Flude et al. (2016) and Flude et al. (2017) evaluated the inherent tracing ability
83 of noble gases focusing on the compositional difference of them between captured CO₂, the subsurface
84 storage reservoir, air and ASW. Differences in the noble gas contents of these samples stemmed from
85 the different CO₂ capturing processes and what controls the composition of noble gas tracer in a stored

86 fluid (e.g. gas stripping of reservoir water and/or interaction with radiogenic components).

87 The concept of inert tracers was extended to artificial enhancement studies, involving the
88 addition of inert gas tracers such as SF₆ and noble gases to the injected CO₂ in CCS storage. This aimed
89 to provide a much clearer distinction between the injected CO₂ and that naturally present in the
90 subsurface and so improving the monitoring efficiency (Myers et al., 2013; Nimz and Hudson, 2005).
91 For example, noble gases have been previously used as artificial tracers to indicate CO₂ leakage
92 pathways in the vadose zone (Cohen et al., 2013; Rillard et al., 2015) and in the aquifer system (Lu et
93 al., 2012; Nimz and Hudson, 2005; Stalker et al., 2009). In the CO₂-Vadose project, undertaken at a test
94 CO₂ release site in France, the lighter noble gases (He and Ne) were found to have the fastest arrival
95 time in monitoring wells due to their higher diffusion coefficient and low solubility within the soil water
96 compared to the CO₂ and other tracers (Cohen et al., 2013). In contrast, the heavier noble gas tracers
97 (Kr and Xe) exhibited the fastest arrival in the aquifer system due to their solubility in groundwater
98 compared to other noble gases following the artificial injection into a deep reservoir (~2 km) (Stalker
99 et al., 2015). In a recent test, a small amount of CO₂ (16.9 kg) spiked with noble gas was released into
100 a shallow aquifer at Korea CO₂ Storage Environmental Management (K-COSEM) study site, in order
101 to understand the behavior of the leaked plume in the shallow groundwater system. This study identified
102 that the mass distribution of the leaked CO₂ is predominantly controlled by the solubility of the
103 individual noble gases and mixing processes during the limited time of monitoring work (i.e. 4 months)
104 (Ju et al., 2019).

105 The shallow groundwater is the final zone encountered by migrating CO₂ before it is lost into
106 the vadose zone and atmosphere. Furthermore, this reservoir is directly linked into the human activity,
107 hence, should be protected from a potential leakage of stored CO₂ (Lee et al., 2016). While noble gas
108 tracers have proven useful to monitor leaked CO₂ plume in shallow aquifer systems (Flude et al., 2016;
109 2017), this has only been demonstrated on a few occasions, for example, in a natural CO₂ production
110 site using inherent noble gases (Gilfillan et al., 2011), in a CO₂ injection test site using artificially
111 enhanced noble gases (Ju et al., 2019) and to rule out CO₂ migration in a shallow aquifer above an

112 actual CO₂ storage reservoir using inherent noble gases (Gilfillan et al., 2017), as described above. In
113 this study, we present the results of applying noble gases to a CO₂ injection test into a near-surface
114 aquifer. This artificial CO₂ migration test aims to mimic a situation where a measurable amount of CO₂
115 (1.70x10² kg) has migrated from a deep CO₂ storage reservoir into a shallow groundwater aquifer. This
116 study focuses on determining the amount of CO₂ retained in the groundwater and the mechanisms
117 controlling the migration of the CO₂ plume using noble gas tracers. A mass balance model was
118 constructed based on the partitioning coefficients of noble gas tracers in a gas-water system, to
119 understand and to quantify the final retention of the injected CO₂ within the shallow aquifer system.

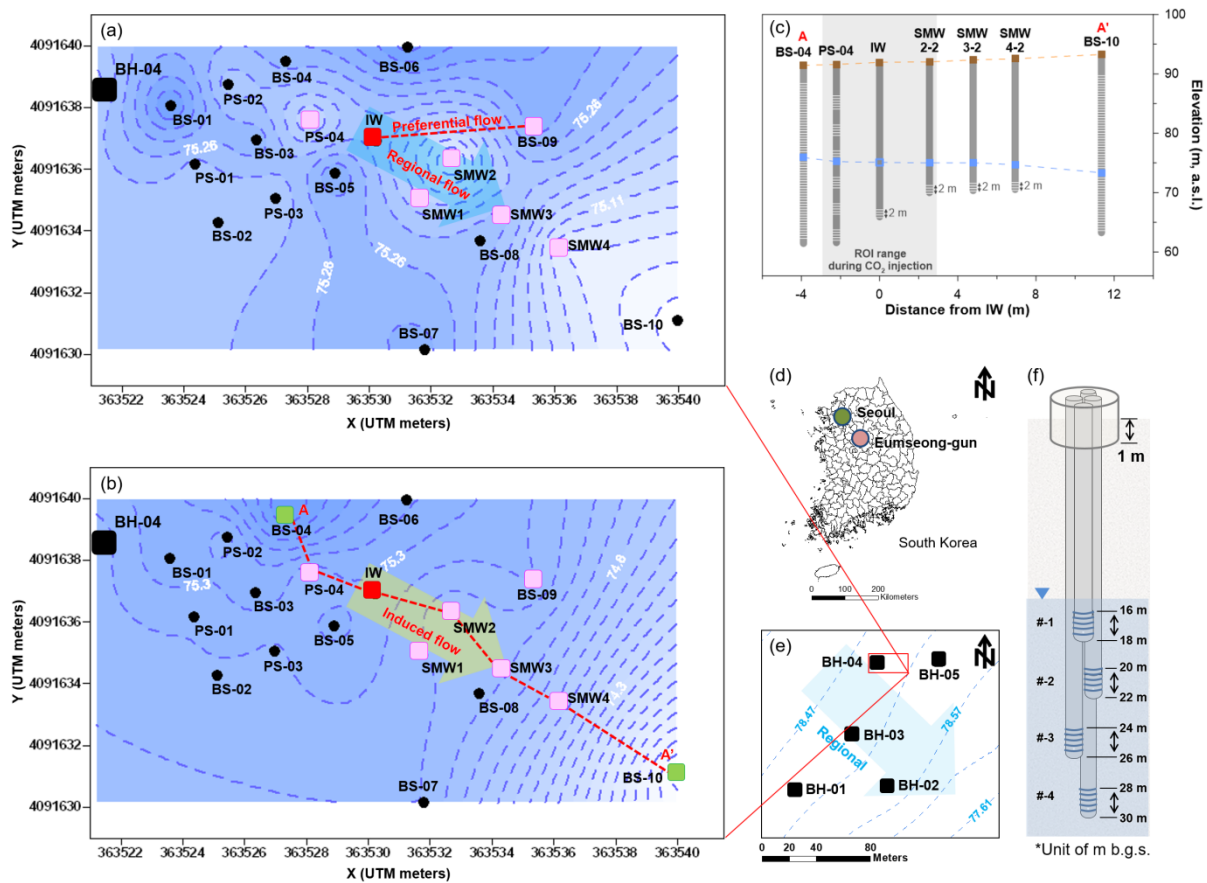
120 **2. Materials and methods**

121 **2.1 Site description**

122 The Korea CO₂ Storage Environmental Management (K-COSEM) Research Center has
123 installed a controlled CO₂ release experiment at Eumseong gun (county) of South Korea (Figure 1). The
124 geology at the field experimental site includes three different subsurface media, firstly consisting of a
125 weathered soil layer composed of medium to coarse grained silty sand (0–30 m below ground surface
126 (bgs)), followed by weathered biotite granite (30–70 m bgs), and finally consolidated biotite granite
127 (starting at 70 m bgs) (Lee et al., 2017; Ju et al., 2018a). The water level was located at the 16.0–18.4
128 m bgs and the hydraulic conductivity of the aquifer was estimated from pumping tests, ranging from
129 1.7×10^{-5} cm/s for the consolidated bedrock to 2.0×10^{-4} cm/s for the weathered layer. Prior to the
130 commencement of the experiment, the groundwater was flowing from the northwest toward the
131 southeast following a hydraulic gradient of 0.003 (i.e., the regional flow in Figure 1a).

132 At the K-COSEM site, a total of 24 monitoring wells had been installed in the shallow aquifer
133 (i.e. < 15 m below the water table) including the injection well (IW), partially screened (PS), boreholes
134 (BH), borehole screened (BS) and saturated zone monitoring wells (SMWs) (Figure 1a). Each saturated
135 zone monitoring well (SMW) contained several screened multi-depth monitoring wells for groundwater
136 monitoring at different depths (Figure 1f). In this CO₂ injection study, the IW and six monitoring wells
137 (PS-04, SMW1 to 4, BS-04, -09 and -10) were employed for the CO₂ injection experiment (Figure 1b).

138 The wells BS-04 and BS-10 located at both ends of the monitoring range were used to create an induced
 139 pressure gradient field by pumping out groundwater at a down-gradient location (BS-10) and successive
 140 injection in at an up-gradient location (BS-4) (Figure 1c). The SMWs are located along the created
 141 groundwater flow pathway, while PS-04 was up-gradient relative to the CO₂ injection point. The well
 142 BS-09 was intended to capture the preferential movement of the released CO₂ along a high connectivity
 143 zone between injection well and BS-09, identified in the work of Ju et al. (2019). Details on the study
 144 site and monitoring network can also be found in previous works (Lee et al., 2017; Lee et al., 2018; Ju
 145 et al., 2018b; Ju et al., 2019).



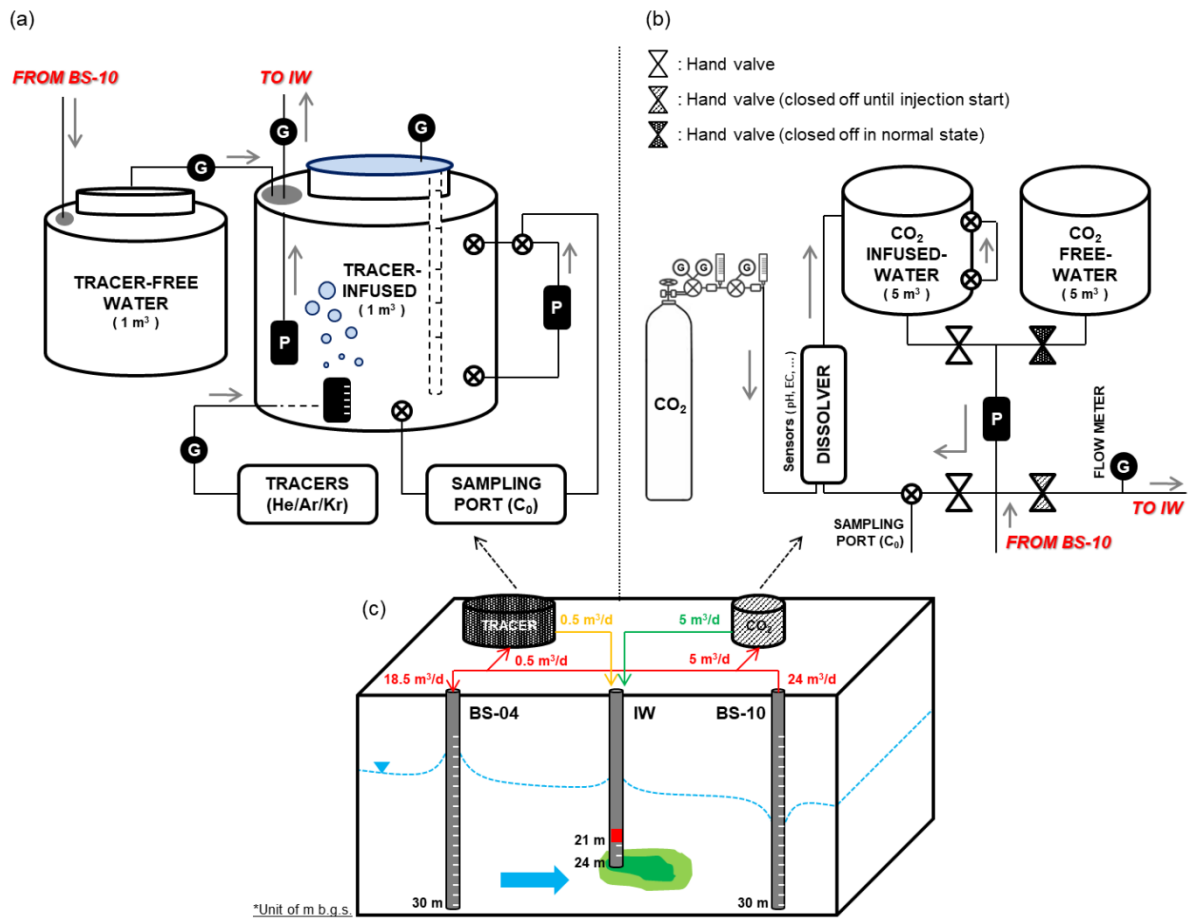
146
 147 **Figure 1.** Maps of the study site. Figures on the left show (a) natural regional groundwater flow (shown
 148 as a blue-colored arrow) before enhanced groundwater circulation using the wells BS-04 and BS-10,
 149 where a preferential path exists in this field due to local hydrogeological heterogeneity (16 May 2016),
 150 (b) induced pressure gradient field (shown as a green-colored arrow) after the pumping out and pumping

151 in using the two wells (see green squares) (4 July 2016). Note that the induced flow was intended to
152 speed up the plume migration along the groundwater flow (i.e., regional flow in [a]). Pink squares
153 represent the wells used for monitoring; a red square represents the injection well (IW). Figures on the
154 right show (c) a cross-section view along the induced pressure gradient (4 July 2016), (d) the location
155 map of the study area, (e) the contours of groundwater levels obtained by kriging using 17 wells
156 surrounding the study site (7 March 2015), and (f) the structure of each saturated zone monitoring well
157 (SMW) containing a bundle of four screened pipes with different lengths.

158 **2.2 Artificial injection**

159 **2.2.1 Induced pressure gradient field**

160 The CO₂ injection was undertaken in the induced pressure gradient field to reinforce the
161 groundwater flow, therefore, to speed up the CO₂ plume migration (Figure 2c). The hydraulic pressure
162 gradient was achieved by enhancing groundwater circulation, consisting of water production and
163 reinjection using the BS-04 and BS-10 wells located at both ends of the monitoring network (Figure
164 2c). A total of 24.0 m³/d of groundwater was pumped from BS-10 and reinjected into BS-04 (Figure
165 2c). A period of 1 month was required to stabilize the pressure gradient (22 May 2017 to 27 June 2017).
166 The pressure gradient was steeper near the injection site and production points (i.e. the BS-04 and BS-
167 10), with the average gradient being 0.18 (Figure 2c). The circulation was maintained until 17
168 September 2017.



169

170 **Figure 2.** Injection systems for the artificial CO₂ release experiment. (a) tracer-infused groundwater
 171 was prepared in a 1 m³ tank and (b) CO₂-infused groundwater was prepared in a 5 m³ tank. (c) gas-
 172 charged groundwater was continuously released into the induced pressure gradient field through the
 173 IW.

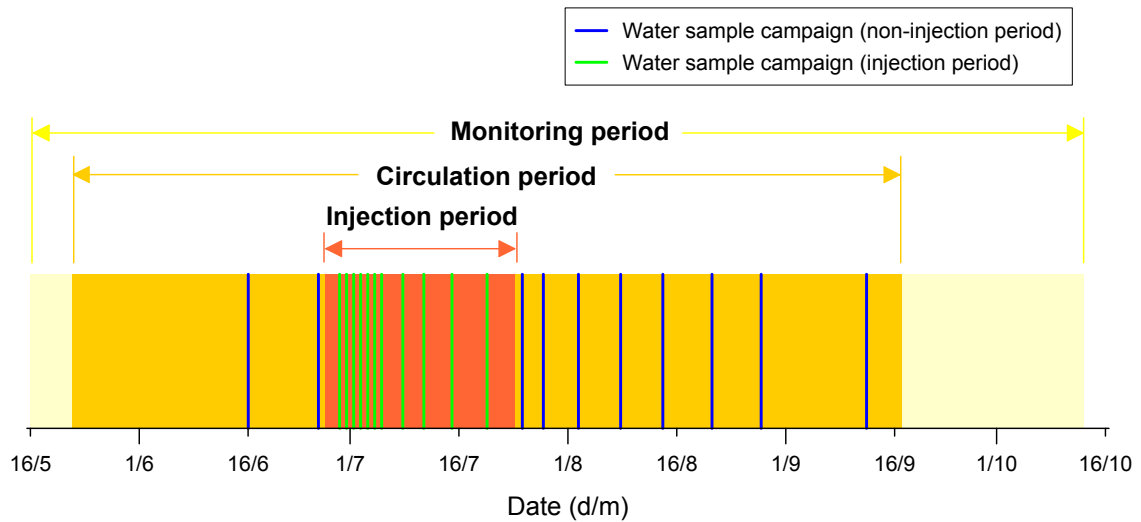
174 2.2.2 Injection

175 To prepare the injection water, the water flux sent to BS-04 (24.0 m³/d) was reduced to 18.5
 176 m³/d and 5.5 m³/d of groundwater was sent into the injection tank (Figure 2c). 5.0 m³/d of groundwater
 177 was sent into the CO₂ dissolver tank (Figure 2b) and 0.5 m³/d of tracer-enhanced water was prepared
 178 in the other tank (Figure 2a). The CO₂-infused groundwater was prepared in the 5 m³ tank equipped
 179 with the circulation pump, CO₂ dissolver, water sampling port and flow meter (Figure 2b). Injection
 180 was initiated when the CO₂ concentration reached the equilibrium state (termed C₀). To ensure that the
 181 equilibrium concentration was maintained, alkalinity, pH, EC, DO, ORP, temperature, salinity, TDS

182 was continuously monitored with real time measurement devices such as YSI (YSI Inc./Xylem Inc.,
183 USA), LTC Levellogger Junior (Solinst, Canada) and SH-300-DS (SOHA TECH, Inc., Korea) while
184 circulating water within the tank using a pump (Figure 2b). These measurements showed that it took
185 approximately 24 hours to achieve the equilibrium state. The noble gas infused groundwater was also
186 prepared one day ahead of the injection test. Approximately 0.5 m³/d of groundwater was pumped into
187 the 1 m³ of closed tank equipped with the circulation pump, tracer tank, water sampling port and flow
188 meter (Figure 2a). The injected tracers were a mixture of He (0.2 vol. %), Ar (99.4 vol. %), and Kr (0.4
189 vol. %) and were injected through a flowmeter and diffuser (AS-10 3/8) into the 1 m³ dissolver tank.
190 The infused liquids were first injected into the subsurface on 27 June 2017 and continued to be injected
191 for 27 days until 24 July 2017. Samples for initial concentration analyses (i.e. C₀) were collected during
192 the injection event and through the sampling ports (Figures 2a and b). Injection took place at 4.5–7.5 m
193 below the water table (corresponding to 21–24 m bgs) in an isolated zone below a packer (Figure 2c).
194 The ambient surface weather conditions during the injection event were 20.4–26.9°C without
195 precipitation. The injection rate was controlled by a submersible and controllable quantitative pump
196 (model MP1, Grundfos, Denmark) at a constant rate of 5.5 m³/d (Figure 2c).

197 **2.3 Real-time monitoring**

198 Real-time monitoring data was collected from 17 May 2017 to 13 October 2017 (Figure 3).
199 Over this period, hydraulic pressure (P), temperature (T) and electrical conductivity (EC) were
200 measured in-situ using the LTC Levellogger Junior (Solinst, Canada) and the barometric state was
201 monitored at the same time using the Barologger Edge (Solinst, Canada) at 10 minute intervals.



202

203 **Figure 3.** Schedule for water sample collection during the CO₂ injection test.

204 **2.4 Water sampling campaign**

205 **2.4.1 Baseline survey period**

206 Water samples were collected using a Waterra Inertial Pump with PowerPack PP-1 (Wattera,
 207 Canada) to obtain baseline data before the CO₂ injection. The local baseline of the *p*CO₂ was obtained
 208 on two occasions through water sampling between 16 June 2017 and 26 June 2017 (Figure 3). The
 209 baseline for the noble gas tracers was determined by a single water-sampling operation on 26 June 2017
 210 (Figure 3). Alkalinity was determined in the field site by acid titration method with 0.05 N HNO₃. The
 211 pH and temperature were also measured in-situ using a portable water quality meter (YSI ProDSS, YSI
 212 Inc./Xylem Inc., USA). The noble gas samples were collected using a standard copper tube of 28 cm³
 213 and a pinch-off clamp set.

214 **2.4.2 Injection and post-injection period**

215 Data acquisition after the CO₂ injection was conducted in the same manner as the baseline data
 216 collection. Water samples were collected on 19 occasions following the injection event, over 76 days
 217 from 27 June 2017 to 12 September 2017 (Figure 3).

218 **2.5 Laboratory analyses**

219 **2.5.1 Noble gas**

220 The noble gas samples were analyzed in the noble gas analysis laboratory at the Korea Polar
221 Research Institute (KOPRI) using an automated system as outlined in Stanley et al. (2009) and Kim et
222 al. (2016). Gases were first extracted from a groundwater sample under high vacuum condition ($\sim 10^{-7}$
223 mbar) and stored in an aluminosilicate glass ampoule (Lott and Jenkins, 1998). Excessive water vapor,
224 active gases, and condensable gases were then removed using cryogenic traps and a series of hot and
225 cold Zr-Al alloy getters (St 101, SAES Getters S.p.A., Italy) before sample injection into the RGA200
226 mass spectrometer (Stanford Research Systems, California, USA) for analysis. The noble gases, He,
227 Ne, Ar, and Kr were calibrated against air standards of 0.9 and 2.7 cm³ STP, to cover the wide range of
228 the tracer enhanced injection water. The discrepancy between duplicate samples was less than 5% (Ju
229 et al., 2019).

230 **2.6 Analytical methods**

231 **2.6.1 $p\text{CO}_2$ calculation**

232 $p\text{CO}_2$ values for the sampled waters were calculated using the monitored parameters of
233 alkalinity, pH, and temperature. Alkalinity, pH and temperature were measured in-situ. Using these data
234 a robust calculation for $p\text{CO}_2$ value was made using the program PHREEQC Version 3 (Parkhurst and
235 Appelo, 2013).

236 **2.6.2 Mass balance model**

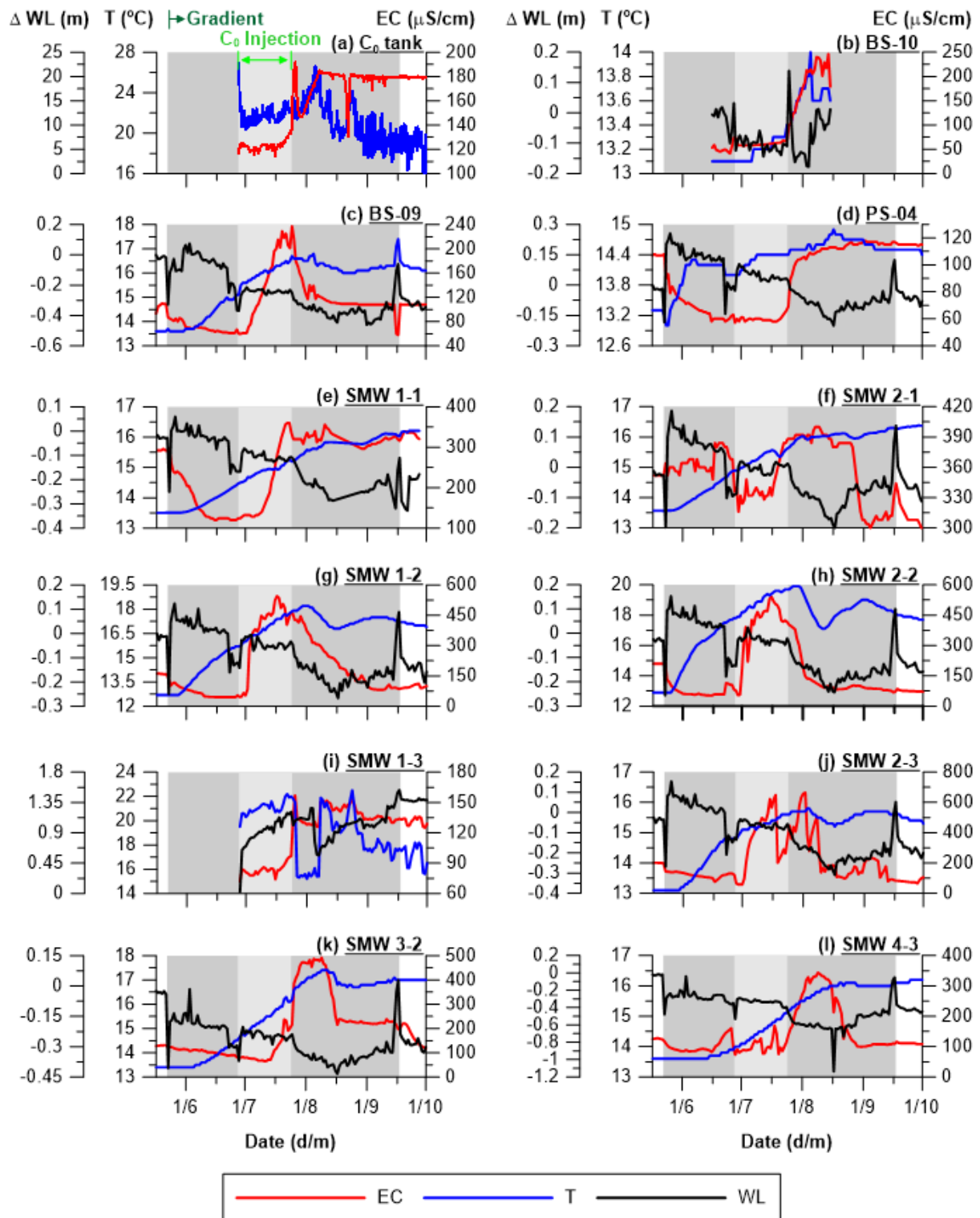
237 At the early stage of the CO_2 injection, the CO_2 plume is unstable with a high partial pressure,
238 resulting in a degree of CO_2 degassing. Hence, CO_2 bubbles rise freely from the brine with a proportion
239 of the CO_2 remaining in the dissolved phase. During the degassing period, the free-phase CO_2 strips out
240 the dissolved, relatively insoluble noble gases, especially the lighter elements (He and Ne), leaving the
241 system relatively enriched in the heavier noble gases (Ar, Kr, Xe) (Ballentine et al., 2002; Holland and
242 Gilfillan, 2013). Based on the degree of this enrichment, we can inversely constrain the mass balance
243 of the CO_2 plume in terms of the degassing process (see the Appendix A mass balance model for detailed
244 explanation).

245 **3 Results**

246 **3.1 Prior to CO₂ injection**

247 Pressure and temperature changes result in the degassing of insoluble substances from the
248 groundwater system. At the K-COSEM test site, the groundwater level shows a clear decreasing trend
249 due to large-scale water consumption from nearby industrial complexes (Figure 4) (Ju et al., 2019).
250 However, prior to the experiment the hydrostatic pressure data showed a stable correlation with
251 atmospheric pressure changes and no irregular turbulence (Supplementary Figure S1). Groundwater
252 temperatures corresponded to normal seasonal values ranging between 12.7 to 13.6°C (Figure 4).

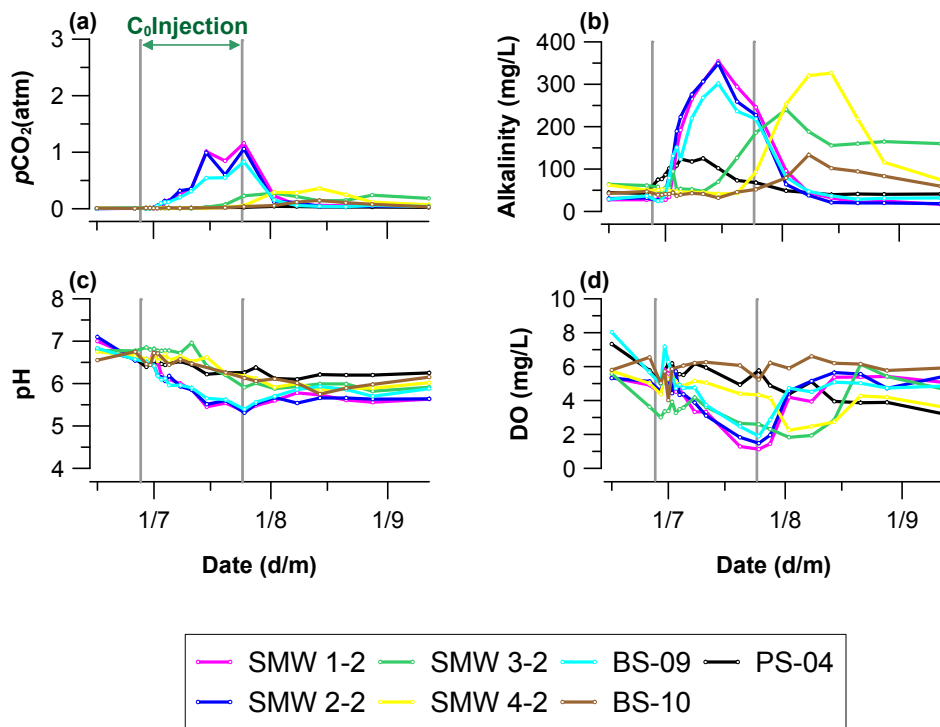
253 The induced pressure gradient commenced on the 22 May 2017 as a result of the onset of water
254 circulation (Figure 3c). Perturbations were detected in the water level (WL), temperature (T), and
255 electrical conductivity (EC) values during the initiation of water circulation (see the start points of dark
256 grey zone in Figure 4). The pressure turbulence was most noticeable within the monitoring wells located
257 inside the radius of influence (ROI) area both of the pumping (BS-10) and injection wells (BS-04). For
258 example, PS-04, SMW 1 series and SMW 2 series wells showed an instant pressure increase after the
259 circulation commenced, as they are located near the injection well (BS-04) (Figure 4d–j). In contrast,
260 wells SMW 3-2 and 4-3 showed an abrupt decrease in pressure, as a result of their location near to well
261 BS-10 where water was extracted (Figure 4k and l). Well BS-09 also displayed a modest increase in
262 pressure 9 days after water circulation commenced (specifically on 31 May 2017) (Figure 4c).
263 Temperature within all monitoring wells showed an overall increase after the water circulation regime
264 started (see the start points of dark grey zone in Figure 4). This is most likely linked to the groundwater
265 for injection having resided in the surface tank at temperatures warmer (i.e., 17.1 to 28.6°C) than those
266 of the subsurface groundwaters (i.e., 13.3°C) for the day prior to re-injection into the subsurface. The
267 EC showed the overall decreasing trend in the initial circulation period as the re-injected water (BS-10)
268 has a relatively low EC background compared to the other wells, with the exception of well SMW 2-1
269 (Figure 4).



270

271 **Figure 4.** Water level (WL), temperature (T) and electrical conductivity (EC) data. Measurements were
 272 completed in the monitoring wells continuously using a LTC data logger. The groundwater circulation
 273 was initiated at 22 May 2017 (dark grey shaded zone) and the CO₂ injection started at 27 June 2017 and
 274 kept going till 24 July 2017 (light grey shaded zone).

275 As outlined previously, two water sampling campaigns were conducted during the circulation
 276 period and prior to CO₂ injection commenced, in order to establish the groundwater baseline
 277 composition (16 June 2017 and 26 June 2017) (Figure 3). The baseline alkalinity values were relatively
 278 low (27.5–64.1 mg/L), DO exhibited a wide variation (3.6–8.0), pH was weakly acidic (6.5–7.1) and
 279 *p*CO₂ was relatively low (0.0–0.01 atm) prior to CO₂ injection (Figure 5). All of the parameters were
 280 close to the baseline values of low carbonate levels in the biotite granite protolith (Ju et al., 2019).



281

282 **Figure 5.** *p*CO₂, pH, alkalinity and DO values. The grey vertical lines represent the injection period.

283 During the water circulation period, pH exhibited an overall decreasing trend as the low-pH
 284 water was pumped out from the down-gradient well (BS-10) and reinjected into the up-gradient well
 285 (BS-04) (Figure 5c). DO also exhibited a decreasing trend as groundwater was re-equilibrated in the
 286 warm surface temperature (17.1–28.6°C) before being injected into the well BS-04 (Figure 4d). *p*CO₂
 287 and alkalinity showed minor variation across the monitored region depending on the groundwater flow
 288 direction and the initial C parameter distributions (Figure 4a and b).

289 Mean He, Ar and Kr concentrations measured before the injection commenced were 5.43×10^{-8}
290 $\text{cm}^3 \text{ STP/g}_{\text{H}_2\text{O}}$, $3.72 \times 10^{-4} \text{ cm}^3 \text{ STP/g}_{\text{H}_2\text{O}}$ and $9.80 \times 10^{-8} \text{ cm}^3 \text{ STP/g}_{\text{H}_2\text{O}}$, respectively. These are close
291 to the Air Saturated Water (ASW) value at the temperature condition (i.e. 13.3°C) of study site—such
292 as $4.58 \times 10^{-8} \text{ cm}^3 \text{ STP/g}_{\text{H}_2\text{O}}$, $3.58 \times 10^{-4} \text{ cm}^3 \text{ STP/g}_{\text{H}_2\text{O}}$ and $8.30 \times 10^{-8} \text{ cm}^3 \text{ STP/g}_{\text{H}_2\text{O}}$ for He, Ar and
293 Kr values, respectively (Kipfer et al., 2002).

294 **3.2 Injection fluid**

295 The gas-infused groundwater was released into the IW from 27 June 2017 to 24 July 2017
296 (Figure 3). The CO_2 -infused groundwater (C_0) collected from the 5 m^3 tank (Figure 2b) was initially
297 below the saturation point (0.40 atm) for 11 days after the injection (29 June 2017 to 8 July 2017), and
298 reached to the over-saturation state ($> 2.3 \text{ atm}$) about 18 days after the injection on 15 July 2017 (Figure
299 5a). This CO_2 variation can be attributed to an accidentally reduced water flux going into the CO_2 tank,
300 causing a decrease of the water level, resulting in altering of the C system balance in CO_2 tank. For the
301 same reason, the pH and DO initially maintained 5.0 and 3.9 mg/L but showed a sudden decrease to 4.2
302 and 0.5 mg/L on the 15 July 2017. Water samples collected from the 1 m^3 tank (C_0) (Figure 2a) were
303 analyzed for their He, Ar and Kr concentrations, and reported at $2.92 \times 10^{-5} \text{ cm}^3 \text{ STP/g}_{\text{H}_2\text{O}}$, $2.26 \times 10^{-}$
304 $^2 \text{ cm}^3 \text{ STP/g}_{\text{H}_2\text{O}}$ and $4.95 \times 10^{-5} \text{ cm}^3 \text{ STP/g}_{\text{H}_2\text{O}}$, respectively. The noble gas concentrations lie between
305 fully saturated and Air Saturated Water (ASW) levels, and thus they will remain dissolved in the
306 groundwater system unless being exposed to low partial pressure conditions such as air bubbles or the
307 vadose zone interface (i.e. water table) (Ju et al., 2019).

308 **3.3 Post injection**

309 **3.3.1 P, T and EC**

310 Pressure turbulence was observed in all monitoring wells prior to the initiation of CO_2 injection
311 (Figure 4), which can be attributed to the change in water volume from $24.0 \text{ m}^3/\text{d}$ to $18.5 \text{ m}^3/\text{d}$ for
312 preparing the gas-infused water of 5.5 m^3 (C_0) before CO_2 injection within the circulation system (see
313 the section 2.2.2 Injection for detailed explanation). Minor changes in temperature were observed inside
314 the Radius of Influence (ROI) zone of IW such as PS-04, BS-09, SMW 1 and SMW 2 (Figure 4c~j).

315 The temperature showed a gradual increase since the groundwater circulation initiated in which the
316 SMW 2-2 showed the highest increase of up to +7.0°C and followed by SMW1-2 (+5.5°C), SMW 3-2
317 (+4.0°C), BS-09 (+3.8°C) and the others (< +2.8°C) (Figure 4). The higher increase in the temperature
318 of BS-09 indicates a preferential flow gradient still exists in the study site even after the formation of
319 the induced pressure gradient (Figure 1a). In EC data, the most prominent signals were recorded at
320 SMW 1-2 (+464 $\mu\text{S}/\text{cm}$, +472%), SMW 2-2 (+447 $\mu\text{S}/\text{cm}$, +368%), SMW 2-3 (+531 $\mu\text{S}/\text{cm}$, +301%),
321 SMW 3-2 (+383 $\mu\text{S}/\text{cm}$, +250%) with the others showing a less pronounced change (< +129%). These
322 observations were consistent with temperature data, exhibiting the greatest change in the SMW #-2
323 wells. This indicated that the CO₂ plume moved horizontally from the injection depth of 21–24 m to the
324 screen depth of SMW #-2 (i.e., 20–22 m) (Figure 1c). The response in EC is clearly different to that of
325 temperature as a notable increase in EC was only observed after CO₂ injection occurred. This is because
326 EC is the function of geochemical interaction between the CO₂ water and the rock materials (Vialle et
327 al., 2014). In the groundwater flow regime, the SMW series wells, BS-09 and BS-10 are located ahead
328 of the migration direction of the IW, which is illustrated by the clearly increasing EC trend (Figure 1b).
329 Alternatively, well PS-04 is located upgradient from the CO₂ injection point, resulting in a gradual
330 lowering of the EC trend after the CO₂ injection was initiated as there is no communication between
331 this well and the CO₂ rich-water (Figure 1b).

332 **3.3.2 $p\text{CO}_2$, pH, alkalinity and DO**

333 As expected, the chemical elements exhibited strong signals correlating with the CO₂ plume
334 arrival. The parameters are presented as breakthrough curves (BTCs) (Figure 5). Note that for the
335 SMWs, the parameters represent the data from the injection depth (i.e., SMW #-2) only, as this
336 generated the largest signals among all depths. The $p\text{CO}_2$ produced the strongest signal at SMW 1-2
337 (+1.15 atm, +25,385%) which was followed by SMW 2-2 (+1.05 atm, +18,067%), BS-09 (+0.82 atm,
338 +12,631%), SWM 4-2 (+0.35 atm, +3,746%) and the other wells (< +2,923%) (Figure 5a). The
339 pronounced response of $p\text{CO}_2$ compared to other parameters is attributed to its low baseline
340 concentration (0.0–0.01 atm) (Risk et al., 2015). Alkalinity also showed significant increases with the
341 arrival of the injected CO₂, particularly in wells SMW 1-2 (+326.4 mg/L, +1,189%), SMW 2-2 (+318.0

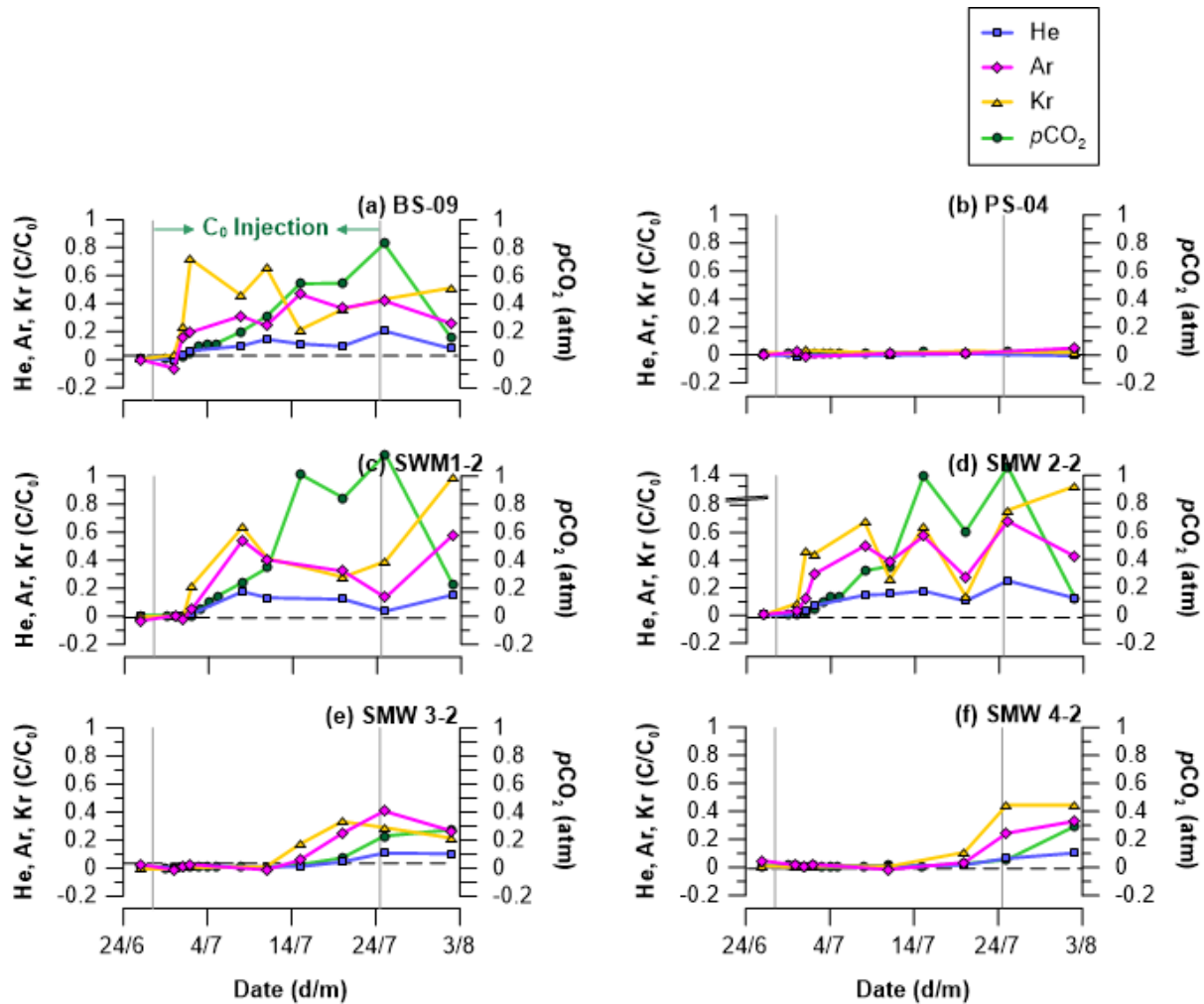
342 mg/L, +1,017%), BS-09 (+269.2 mg/L, +821%), SMW 4-2 (+270.0 mg/L, +478%) with other wells
343 showing smaller, but measureable changes (< +286%) (Figure 5b). Alkalinity gradually increases with
344 the chemical interactions between the CO₂ plume and the aquifer materials similar to the EC. The small
345 differences in response to CO₂ injection between EC and alkalinity can be attributed to the geochemical
346 variation of the study site resulting in different CO₂ related buffering capacities (Sechriest, 1960).

347 The pH also decreased noticeably, changing by -1.5 units at SMW 2-2, which was followed by
348 -1.5 units at SMW 1-2, -1.4 units at SMW 2-3, -1.3 units at BS-09 and > -0.96 units at the others (Figure
349 5c). The DO showed relatively modest change by up to -4.0 mg/L (-78%) at SMW 1-2 which was
350 followed by BS-09 (-4.9 mg/L, -72%), SMW 2-2 (-3.7 mg/L, -72%), SMW 3-2 (-2.8 mg/L, -60%) and
351 the others (< -58%) (Figure 5d). In this experimental setting, the DO evolves with the three-component
352 groundwater mixing between low-DO water volumes (re-injection water at BS-04 and injection water
353 at IW) and high-DO water volume (local groundwater) (Figure 2).

354 3.3.3 Noble gas tracers

355 The measured concentrations of He, Ar and Kr tracers are presented in BTCs (Figure 6). The
356 concentration was normalized to the injection amount (C_0) after the background portion (i.e.
357 atmospheric origin) was subtracted from both monitored (C) and initial concentration (C_0), to simply
358 define the CO₂ arrival as a positive signal. Note that for the SMWs, the parameters present the data
359 from the injection depth (i.e., SMW #-2) only, as this exhibited the largest signals of all depths. As a
360 result, the tracers successfully produced the strong positive signals with the CO₂ plume arrival in the
361 BTCs (Figure 6). The tracer concentrations exhibited variable arrival times and concentrations due to
362 the CO₂ plume following different flow paths within the heterogeneous groundwater system at the site,
363 similar to the findings of Kilgallon et al. (2018), Lee et al. (2017), Lu et al. (2012) and Stalker et al.
364 (2015). Most importantly, Kr showed the earliest arrivals through all monitoring wells compared to the
365 He and Ar tracer. This was attributed to the Kr taking a less distributed pathway through the subsurface
366 than the other tracers, and a result of the dilution of CO₂ plume along the concentration gradient (see
367 the discussion section 4.1.2 Diffusion process controlling the efficiency of noble gas tracing).

368 The tracers associated with the CO₂ plume were firstly detected in SMW 2-2 (+4 d) followed
369 by BS-09 (+4 d), SMW 1-2 (+5 d), SMW 3-2 (+18 d) and SMW 4-2 (+23 d) (Figure 6a, c, d, e and f).
370 The strongest signal was recorded at SMW 2-2 (+1,430% for He, +322% for Ar and +6,904% for Kr)
371 suggesting the majority of the CO₂ plume moved along the induced groundwater pressure gradient
372 (Figure 6). A portion of the tracers also moved toward BS-09 and produced a strong signal in spite of
373 being a greater distance away from the injection point (5.2 m) than that of SWM 1-1 and SMW 2-2 (2.6
374 m). This can be attributed to the preferential flow pathway present in the study site (Figure 1a) (Ju et
375 al., 2019; Lu et al., 2012). Well PS-04 did not record the presence of any tracers during the injection
376 period due to its location behind the IW in the groundwater flow direction (Figure 1b). It is worth noting
377 that SMW 4-2 exhibited a higher concentration of Kr once the tracers arrived than SWM 3-2 (Figure
378 6), implying that a low conductivity zone hinders well SMW 3-2 from capturing the full CO₂ plume.
379 This result was consistent with the observations made in alkalinity and *p*CO₂ (Figure 5).



380

381 **Figure 6.** Gas tracer concentration during the experiment. Noble gas was presented as C/C_0 (see the
 382 text for details) with $p\text{CO}_2$. The grey vertical lines show the start and end of the injection period. The
 383 Air Saturated Water (ASW, black dotted horizontal line) was calculated according to Kipfer et al. (2002)
 384 to indicate the local background level of noble gas tracers.

385

386

387

388

389

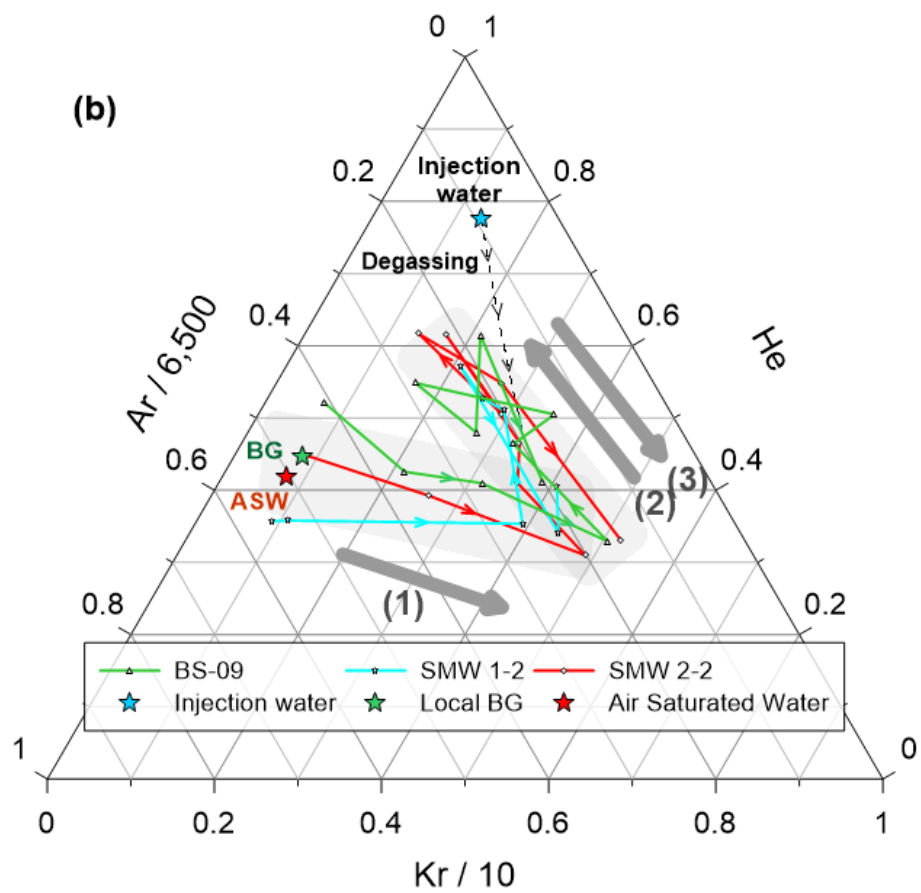
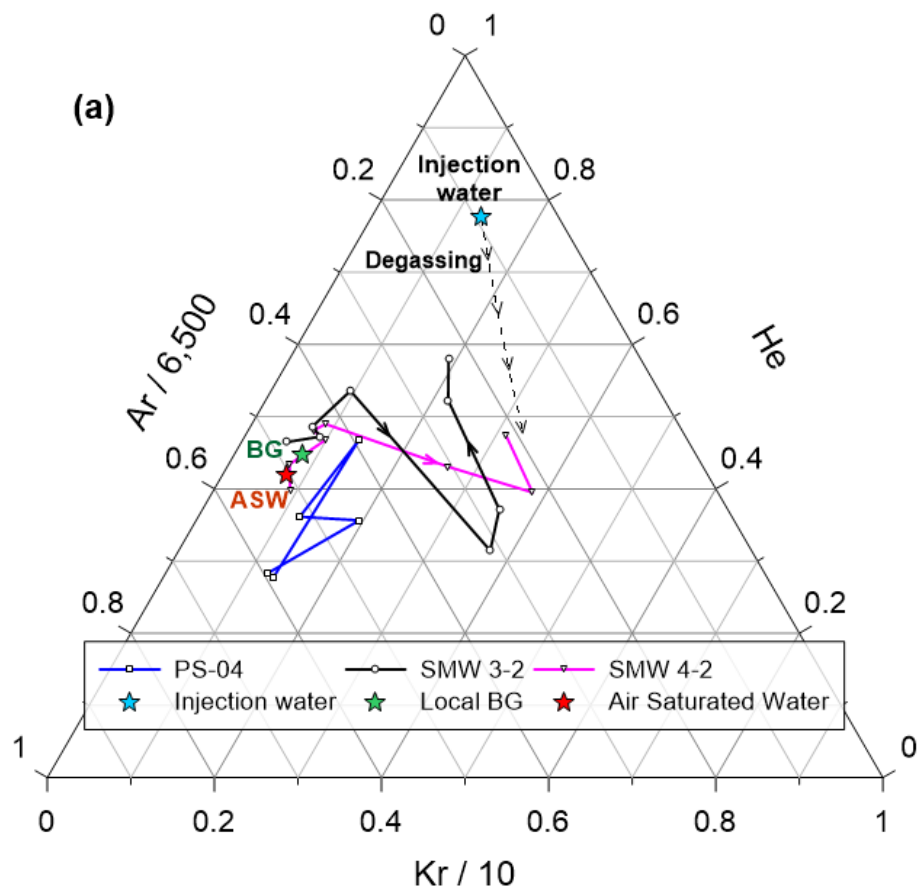
390

391

392

As the injection water gradually approached the monitoring network, the observation wells captured the temporal evolution of the CO_2 plume. In the early stage of BTCs, Kr showed the fastest arrival time compared to the other tracers for all monitoring wells (Figure 6). This was followed by an increase in Ar and He concentrations, with both parameters soon reaching their peak concentration within a few days (Figure 6). In the final stage of BTCs, the plume tail is recorded in all of the monitoring wells through the decrease of noble gas concentrations after injection at the IW ceased. However, it can be observed that the concentration increased in the last stage of the BTCs for monitoring wells adjacent to IW (Figure 6c and d). This can be attributed to the circulation injection system of this

393 experiment. In the final stage of the injection period (4 days before the end of injection), the tracer-
394 charged plume had reached BS-10 (Figure 4b). As water was still being produced for the reinjection at
395 the IW, a portion of the CO₂ plume was returned back into the injection tank containing the artificial
396 noble gas tracers. Note that heavier components such as Ar and Kr acted as an early warning tracer for
397 CO₂ arrival in every monitoring well during the monitoring period. This was attributed to physical
398 mechanisms affecting the distribution of the dissolved gases (see the section 4.1.2 Diffusion process
399 controlling the efficiency of noble gas tracing).



401 **Figure 7.** Noble gas ternary diagram showing the two groups of wells categorized by their response.
402 (a) monitoring wells which showed no concentration change from background level (i.e., PS-04) or
403 only an early-stage evolution (i.e., SMW 3-2 and SMW 4-2). (b) monitoring wells that showed a three-
404 step evolution as located close to the injection point (i.e., SMW 1-2 and SMW 2-2) and located in a
405 preferential migration path (i.e., BS-09). The early-stage CO₂ plume is characterized by high Kr
406 concentration (Arrow 1), the plume then gradually increases in He and Ar concentrations (Arrow 2). In
407 the final stage, it becomes rich in Kr again, following the cessation of injection (Arrow 3). The peak
408 composition was different from that of injection water due to initial degassing loss.

409 The consistent temporal evolution of the recorded noble gas concentrations within the six
410 monitoring wells is depicted in the ternary diagram of Figure 7. The local BG (i.e., green star) represents
411 the average of background level of individual monitoring wells. Prior to the CO₂ plume arrival, each
412 monitoring well plots near to the Air Saturated Water (ASW) level. The initial arrival of the CO₂ plume
413 was marked by a significant increase in Kr in all monitoring wells (see the arrow 1 in Figure 7) which
414 corresponds to the early stage evolution in the BTCs (Figure 6). Note that PS-04 did not exhibit a
415 response after injection. Following the arrival of the Kr tracer, the He and Ar concentrations within the
416 monitoring wells increase as the plume center approached, converging at a single point (Figure 7).
417 However, the concentrations of noble gas tracers at the peak concentrations were lower than those at
418 the time of injection. They were 73.6–88.3% (He), 26.2–55.5% (Ar), and 0–65.5% (Kr) of the initial
419 concentrations. The lower concentrations can be attributed to the degassing loss of the injection fluid
420 (Sathaye et al., 2016), explained in more detail in the section 4.1.1. This degassing process controls the
421 overall retention amount of the injected CO₂. The composition of the plume tail captured in the
422 monitoring wells was similar to the composition of the plume front, characterized by a high Kr
423 concentration (Figure 7).

424 **3.4 Following injection**

425 CO₂ injection ceased after 28 days (27 June 2017 to 24 July 2017) (Figure 3). This corresponds
426 to the point where the monitoring parameters start to change at the BS-10 (Figure 4b and 5). In this

427 moment, the slight increase of EC was also observable in the CO₂ tank as CO₂ water re-entered the
428 injection tank (Figure 4a). Additionally, PS-04 also showed a minor increase in EC at the termination
429 period due to the re-circulation of CO₂ injected water (Figure 4d). From this point (24 July 2017), the
430 groundwater circulation system was modified to avoid the re-enhancement of the CO₂ plume. Another
431 local groundwater from BH-03 was prepared and from then onwards substituted the circulation portion
432 going to the BS-04 (Figure 1e and 2c).

433 **3.5 Following groundwater circulation**

434 The groundwater circulation ended on 17 September 2017, 56 days after CO₂ injection stopped
435 and 118 days after groundwater circulation commencement (Figure 3). The pressure turbulence was
436 observable in all monitoring wells (Figure 4) and also EC turbulence was detected in some of the
437 monitoring wells (Figure 4c, f and k), but the groundwater quickly recovered to its previous state (Figure
438 4).

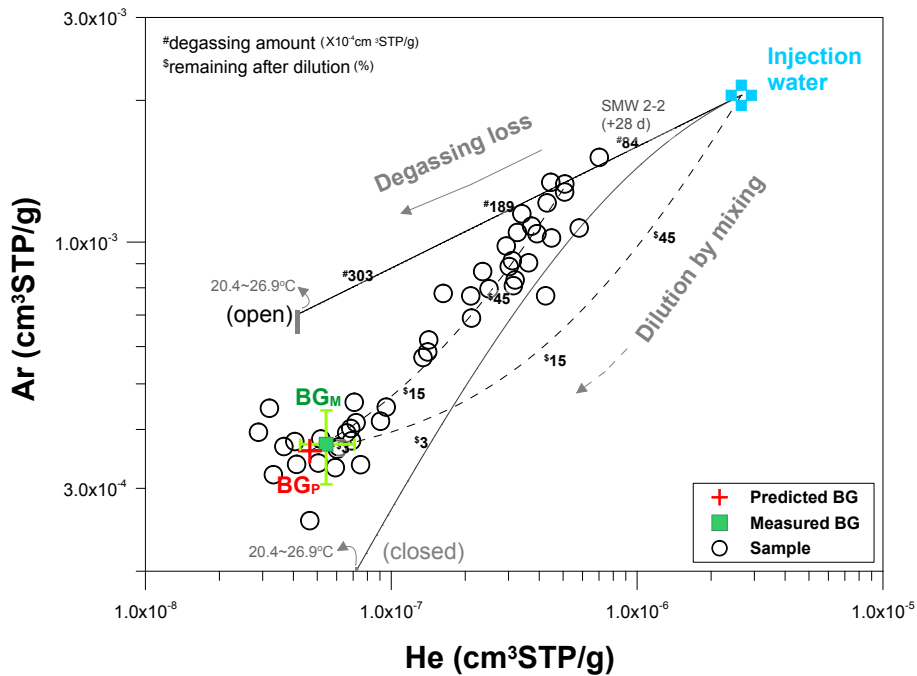
439 **4 Discussion**

440 **4.1 Mass retention mechanisms**

441 **4.1.1 Degassing process controlling the overall retention amount of released CO₂**

442 If an inert tracer is continuously released into the groundwater system, the concentration will
443 gradually increase in monitoring wells and eventually become similar to the composition of injection
444 fluid. In this study, as the tracer-charged water was continuously released into the groundwater system,
445 the monitored concentration was expected to resemble the injection fluid's concentration by the final
446 stage. However, a notable difference in CO₂ and noble gas concentrations was observed between the
447 injection fluid and the plateau points (Figure 7). This phenomenon indicates that tracer mass was not
448 conserved in the groundwater system and suffered from mass-reducing processes. As the noble gas
449 tracer is biochemically inert in the groundwater system, the decrease is likely to be the result of physical
450 processes (Holland and Gilfillan, 2013). For instance, a similar noble gas deficit has been observed in
451 a natural CO₂-rich system, where CO₂ and CH₄ bubbles also stripped out the insoluble gases from the
452 groundwater system (Gilfillan et al., 2008, 2017; Brennwald et al., 2005; Zhou et al., 2005) and in

453 artificial CO₂ injection sites (Nimz and Hudson, 2005; Stalker et al., 2015). Hence, this deficit could be
 454 explained by the degassing of unstable CO₂-rich plume.



455
 456 **Figure 8.** Mass balance of the CO₂ plume depicted with He and Ar tracer. The plume was expected to
 457 follow the mixing line between the injection water (blue cross symbol) and the measured background
 458 concentration (BG_M, green square symbol). Degassing loss of CO₂ from the dissolved CO₂ plume,
 459 would result in a new mixing line starting from the SMW 2-2 (+28 days) toward the background
 460 concentration (BG_P, red cross symbol). The BG_P was estimated based on the optimization process of
 461 the degassing model (see the Appendix B Model optimization for detailed explanation). The shaded
 462 zone on the degassing models indicates the uncertainty arising from the injection water temperature
 463 (20.4–26.9°C).

464 A diagram was constructed using noble gas tracers to determine the major processes
 465 influencing the CO₂ plume migration (Figure 8). In Figure 8, the concentrations of He and Ar at the
 466 well SMW 2-2 (on 25 July 2017) decreased gradually to their background concentration (BG_P),
 467 indicating mixing of the plume with the local groundwater. The mass distribution of observed samples
 468 was the function of two distinct processes over the testing period: mass reduction of the CO₂ plume
 469 occurred through the degassing process (black line), followed by the dilution of the plume by the local

470 groundwater (black dotted line). The observed data clearly indicated the mixing process was preceded
 471 by the degassing process.

472 **Table 1** Mass balance of the leaked CO₂ plume in shallow aquifer system.

Open system	Injection		After degassing loss			Solubility [†] (mM/atm)
	Amount (kg)	partial pressure (atm)	ΔAmount (kg)	Δpartial pressure (atm)	Remaining (%)	
He	7.04×10^{-5}	3.07×10^0	5.64×10^0	2.46×10^0	19.9	0.386
Ar	5.43×10^0	6.11×10^0	1.85×10^0	2.08×10^0	66.0	1.50
Kr	2.50×10^0	7.41×10^0	5.13×10^0	1.52×10^0	79.5	2.71
CO ₂ p. [‡]	1.70×10^2	6.62×10^0	2.72×10^0	1.07×10^0	98.4	38.7

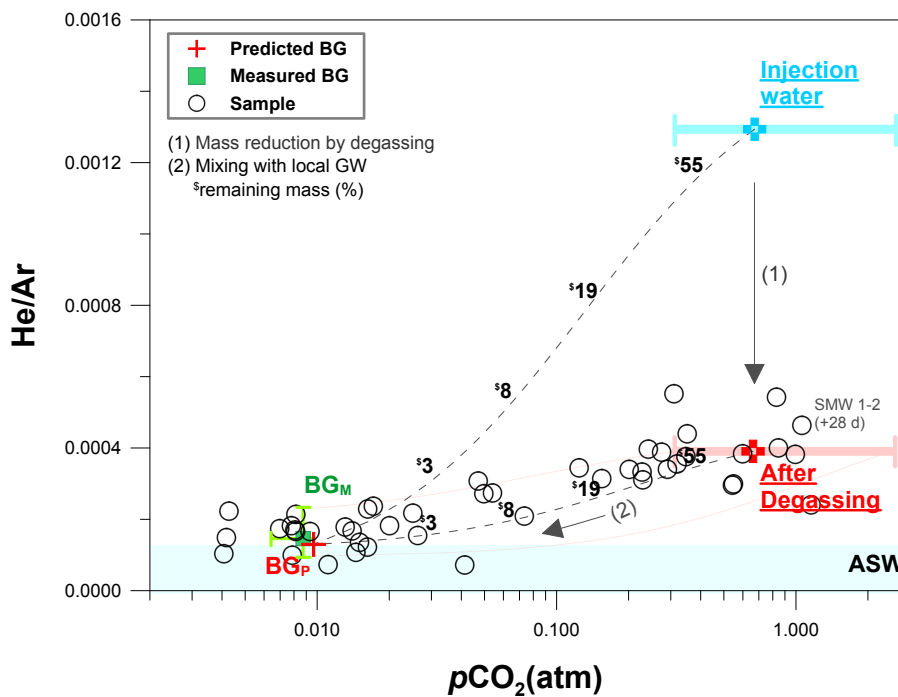
473 [†]NIST chemistry webbook of Sander (2017) at temperature of 21.8°C.

474 [‡]The predicted value from model optimization (see the Appendix B Model optimization for detailed
 475 explanation).

476 Elemental fractionation of noble gases is controlled by their differing solubilities and the
 477 ambient reservoir conditions (Figure 8) (Ballentine et al., 2002; Ma et al., 2009). In a closed system,
 478 the dissolved air remains in the groundwater, and equilibrium is achieved between the bubbles and the
 479 surrounding groundwater. In an open system, the air bubbles are mobile after the phase transition and
 480 escape from the aquifer system continuously until the end of the degassing process. In Figure 8, the
 481 mixing line (black dotted line) intersects a degassing line (black line) explaining the loss of air bubbles
 482 by $1.40 \times 10^{-2} \text{ cm}^3/\text{g}_{\text{H}_2\text{O}}$ through the degassing process in an open system. The analytical technique for
 483 this calculation is shown in Appendix A Mass balance model. In the experiment, CO₂ degassing was
 484 detected just above the water table at the IW reconfirming the initial loss happened into the vadose zone
 485 (Supplementary Figure S2).

486 Unlike noble gases, CO₂ is involved in diverse chemical and biological processes in the
 487 groundwater. To identify the major controls on the CO₂ distribution, the *p*CO₂ was plotted against
 488 measured noble gas tracer concentrations in Figure 9. As expected, the total mass of CO₂ in the plume
 489 was decreased by degassing and mixing processes. Our data designate a clear mixing line stretching

490 from SMW 1-2 (25 July 2017) to BG_p, indicating that mixing process mainly controlled the mass
 491 distribution of CO₂ in the plume after the initial degassing event. The minor variations from the mixing
 492 trend mostly fall in the ranges of the initial composition of injected CO₂-infused water (Figure 9). The
 493 solubility-controlled process is shown as the black arrow stretching from the blue-cross symbol to red-
 494 cross symbol (Figure 9). The abrupt change in He/Ar ratio stands in strong contrast to the minimal
 495 change observed in the *p*CO₂ during the degassing event (ca. 1.6% overall loss of CO₂). Losses of noble
 496 gases (20.5% for Kr, 34.0% for Ar, and 80.1% for He) are much greater than for CO₂ (Table 1).



497

498 **Figure 9.** Plot of *p*CO₂ against He/Ar showing the concentration changes of CO₂ and noble gas tracers
 499 during CO₂ plume evolution. The BG_M (green square symbol) is the measured background level, and
 500 the BG_P (red cross symbol) is an estimated value from the optimization process of the degassing model
 501 (see the Appendix B Model optimization for detailed explanation). The CO₂ plume firstly reduces total
 502 mass by the degassing process (Arrow 1) and then gradually gets diluted by mixing with local
 503 groundwater (Arrow 2).

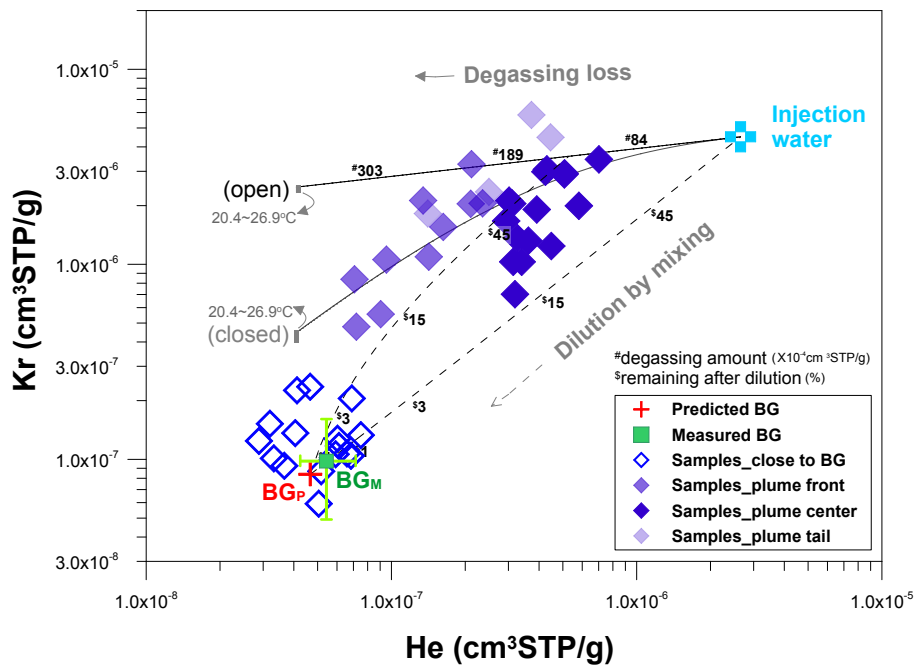
504

4.1.2 Diffusion process controlling the efficiency of noble gas tracing

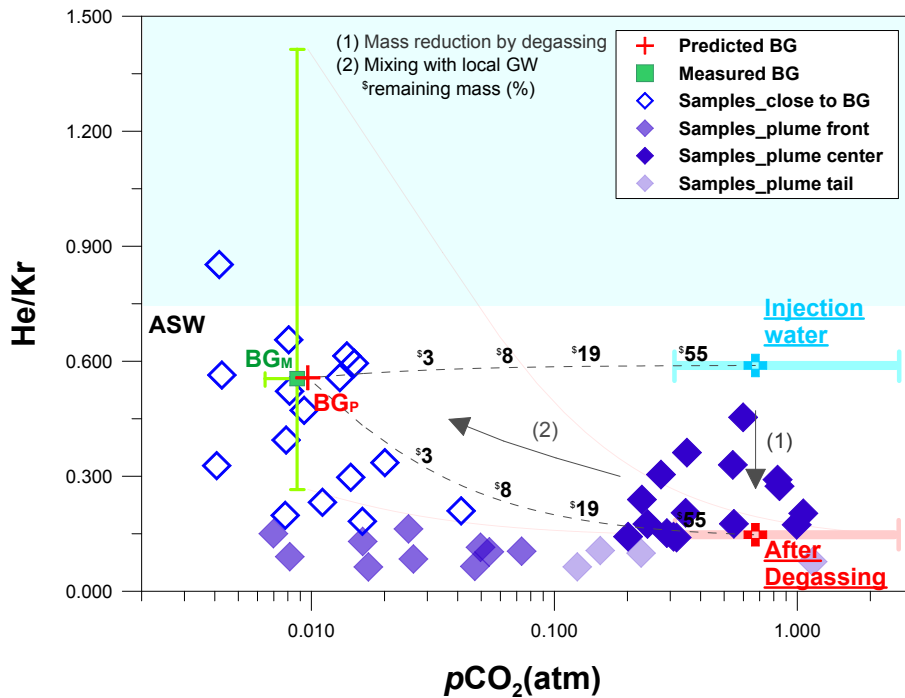
505

The different noble gas species cover a wide mass range and thus may provide a chance to

506 constrain the mass-dependent processes occurring in the groundwater system. A comparison was made
 507 to scrutinize the behavioral difference for noble gases, as observed from the He/Ar (Figure. 8) and
 508 He/Kr (Figure 10) relationships. The mixing line in Figure 10, represented by a black dotted line
 509 stretching from the degassing line to BGp, corresponds to the mixing line estimated in Figure 8.
 510 However, it is noteworthy that the He and Kr pair did not exhibit a singular trend with many variations
 511 scattering from the estimated mixing line. It is also noteworthy that samples from the plume's center
 512 tend to converge on the estimated mixing line, while the samples from both the plume's front and tail
 513 display a large scatter pattern over the estimated line (Figure 10). Such discordance was also observable
 514 in the $p\text{CO}_2$ versus He/Kr diagram (Figure 11) in which many samples, especially those from the
 515 plume's front and tail had significantly lower He/Kr ratios (around 0.10) than the ratio describing the
 516 estimated mixing line (0.24). This difference indicates that another mass-dependent process was
 517 affecting the tracer distribution in addition to the solubility-controlled process.



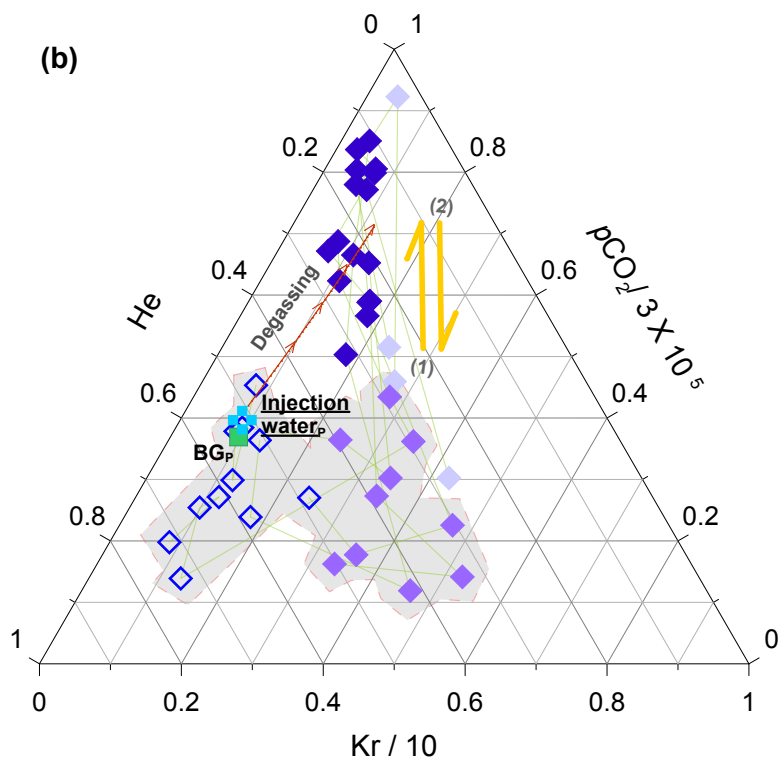
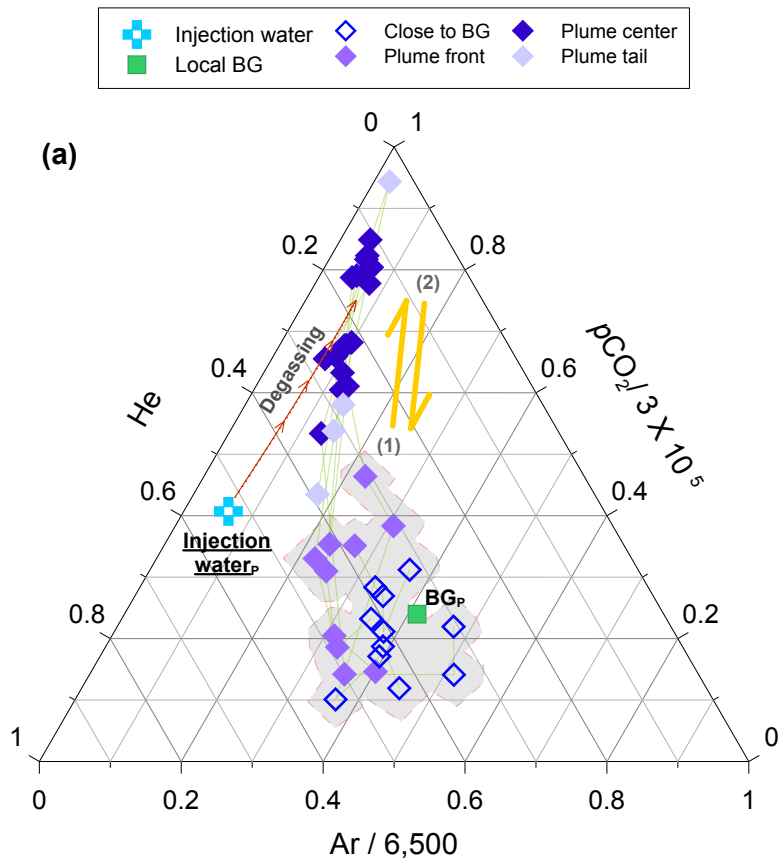
518
 519 **Figure 10.** Mass balance of the CO₂ plume depicted with He and Kr tracers. To see the plume evolution
 520 in detail, the samples were sorted by the breakthrough positions. Note that many samples, especially on
 521 the plume front and tail, are scattered over the estimated mixing line, contrary to the He–Ar pair mixing
 522 trend in Figure 8.



523

524 **Figure 11.** Diagrams showing the concentration changes of CO_2 and noble gas tracers during CO_2
 525 plume evolution. To see the plume evolution in detail, the samples were sorted by the breakthrough
 526 positions. Note that, many samples, especially on the plume's front and tail, are scattered from the
 527 estimated mixing line, as compared to the observations in the $p\text{CO}_2$ versus He/Ar relationship in Figure
 528 9.

529 To further examine the temporal progression of the CO_2 plume, ternary plots of $p\text{CO}_2$, He, and
 530 Ar or Kr were composed according to the locations of samples in the plume (i.e., front, center, and tail)
 531 (Figure 12). In the He/Ar/ $p\text{CO}_2$ diagram, the samples have a small variation near BG_p in the initial
 532 period, while as the plume center approached the monitoring points, it showed an upward shift toward
 533 the degassing point in the Figure 12a. In the He/Kr/ $p\text{CO}_2$ diagram, the samples show a much wider
 534 variation during the initial stage of the CO_2 plume arrival than the observed change in the He/Ar/ $p\text{CO}_2$
 535 diagram (Figure 12b). This difference indicated that another physical process was involved in the mass
 536 distribution at the CO_2 plume's front. Note that the initial composition of the plume was characterized
 537 by the high concentration of Kr as it appeared firstly in the observation wells (see also Figure 7).



539 **Figure 12.** Ternary diagram showing the compositions of $p\text{CO}_2$, He, and Ar (a) or Kr (b) tracers. To
540 scrutinize the plume evolution, the samples were sorted according to the breakthrough positions. In the
541 initial period of plume evolution, the relative compositional change among $p\text{CO}_2$, He and Kr (b) showed
542 a much wider variation near the background levels (BG_p , green square symbol) than that observed
543 among $p\text{CO}_2$, He and Ar (a), which attributed to the diffusion process (see the text for details). This
544 diffusion-dominant movement was followed by the upward shift toward the degassing point (see Arrow
545 1), as also shown by the intersection point in Figure 8. In the final stage, the samples return to the
546 composition similar to the plume front (see Arrow 2), after cessation of injection.

547 In open water, diffusion is capable of elemental fractionation depending on the molecular mass
548 (Zheng and Bennett, 2002). According to Fick's law, the mass distribution of a solute in a groundwater
549 system is restricted by molecular diffusion along the concentration gradient. In our experimental design,
550 the artificial injection formed a CO_2 - and tracer-rich plume in the groundwater system, setting a steep
551 concentration gradient at the plume boundary. Consequently, the plume boundary was actively
552 subjected to the diffusion process facing with the local groundwater of low concentration level of noble
553 gases. As the diffusion rate is inversely proportional to the elemental mass of the solute, the tracer
554 composition at the plume boundary was regulated by the mass-dependent fractionation. This
555 phenomenon also has been observed in a coal bed methane field, where the free CO_2 and CH_4 gases
556 stripped off the insoluble noble gases from groundwater and this action set the concentration gradient
557 at interfaces with the un-degassed local groundwater, at which diffusion process resulting in a mass
558 dependent fractionation of noble gas tracers (Zhou et al., 2005). Overall, the fact that the diffusion
559 allocates the mass distribution at plume boundary (i.e., plume's front and tail) suggests that the early
560 detection of the migrated CO_2 plume is dependent on this process. This further implies that the early-
561 stage degassing loss is of primary importance in terms of the noble gas tracing efficiency because the
562 degassing process is associated with the overall plume composition including the feature of the
563 concentration gradient at plume front.

564 5 Conclusions

565 A portion of CO₂ stored within the deep subsurface may unintentionally migrate upward to
566 reach overlying shallow aquifers. Whilst noble gas tracers have proved to be useful in monitoring CO₂
567 leakage, they have been rarely adopted for monitoring purposes in the shallow aquifer system. This
568 study utilized the noble gas tracers to indicate the CO₂ leakage and also to elucidate the mass balance
569 of the leaked plume after injection of 1.70 x 10² kg of CO₂ into a shallow aquifer system. The CO₂- and
570 tracer-enhanced groundwater was released into the induced gradient field and subsequent monitoring
571 works have been conducted. The noble gas tracers produced a strong signal of the migrated CO₂, with
572 Kr consistently exhibiting the first arrival time, ahead of the plume and the other noble gas tracers
573 throughout all of the monitoring points.

574 The mass distribution of the CO₂ plume was controlled by three different physical processes;
575 solubility-controlled (degassing), physical groundwater mixing and diffusion. The degassing process
576 reduced the overall mass of the CO₂ plume and caused noble gas tracers to be mass-dependently
577 fractionated, which occurred at the initial stage of CO₂ leakage before plume migration. The diffusion
578 process was also involved during the plume migration, but only influenced the noble gas distributions
579 in the leaked plume and did not act as a primary control for the CO₂ distribution within the monitoring
580 period. This phenomenon, however, can accelerate the dilution of artificial tracers at the plume front,
581 especially for the lighter elements, suggesting this process has an important control on the monitoring
582 efficiency of the artificial tracers in terms of early detection of CO₂ leakage. Most importantly, as the
583 noble gas tracers display more apparent changes according to the retention mechanisms than CO₂ itself,
584 they can provide a robust system for precisely monitoring both the fate and pathway taken by the
585 migrating CO₂.

586 Noble gas tracers were used to constrain the physical retention mechanisms of the injected CO₂
587 within a shallow aquifer. Our findings indicate that around the injection point, CO₂ degassing
588 dominantly occurs from the dissolved plume due to the high gas pressure, suggesting a near-surface
589 monitoring network is necessary for capturing the active “vertical” movement of degassed budget in
590 this area. This can be accomplished by performing a continuous monitoring of CO₂ at the vadose zone,

591 for example by a soil flux measure, soil gas sampling and borehole head space sampling around a
592 potential leak point. The monitoring regime can be performed cost-effectively with limiting a
593 “degassing boundary” around a suspected leak point. In this study, only a few meters away from the
594 leak point (>2.6 m), the degassing behavior was greatly diminished as a gas pressure of CO₂ plume
595 reduced significantly. From this point, the CO₂ plume was stabilized as a dissolved phase and
596 dominantly diluted by mixing with a local groundwater along a flow direction. Therefore, from this
597 stage, sparse monitoring of saturated zone is recommended for tracing down a horizontal migration of
598 a dissolved CO₂ plume, rather than an intensive gas monitoring for a degassed component. Hence, the
599 key aspect to establish an effective monitoring network is how well constrained the “CO₂ degassing
600 boundary” around a potential leak point is, and how well the groundwater flow regime is understood.

601 Monitoring of degassed CO₂ might not be easily achieved in a real CCS field using direct
602 measurements. In this study, the degassing boundary was just a few meters from the leak point (< 2.6
603 m), whilst a strong artificial gradient (~0.18) was enforced for the plume migration. This suggests that
604 a degassing boundary would be even narrower in a natural gradient system, making a direct detection
605 of this extremely difficult. Furthermore, heterogeneity in the vadose zone can put an additional
606 uncertainty in monitoring of the vertical flux, as gaseous CO₂ can take various pathways in the vadose
607 zone depending on the soil permeability distribution (Cohen et al., 2013). Hence, identification of a
608 point source of CO₂ leakage using a direct measurement technique in the vadose zone would be very
609 difficult, unless an intensive monitoring is undertaken around the exact point source. However, noble
610 gas monitoring of groundwater is able to record the migration of a CO₂ plume from the leak point along
611 the groundwater flow pathway, as highlighted in this study. Our findings are similar to previous work
612 (Mackintosh and Ballentine, 2012) that showed monitoring of noble gases in groundwater is an order
613 of magnitude more sensitive for detecting migrated gases than vadose zone gas monitoring. Therefore,
614 we recommend that monitoring of noble gases in groundwaters should be used in addition to direct
615 vadose zone methods, in order to increase the sensitivity of the monitoring regime and improve the
616 protection of the shallow groundwater aquifer above a storage site.

617 **Acknowledgements**

618 This research was supported by a Korea Environmental Industry & Technology Institute (KEITI) grant
619 entitled “R&D Project on Environmental Management of Geologic CO₂ Storage” (Project Number:
620 2018001810002), by a Korea Polar Research Institute grant (PE19060) and by a National Research
621 Foundation of Korea (NRF) grant funded by the Korean government (MSIT) (No. 0409-20190119). We
622 thank all the members of the K-COSEM team and, appreciate Intae Kim and Minjung Kim for their
623 efforts and support on noble gas analysis. Also, we appreciate the help of Dr. Stan E. Beaubien in
624 interpreting the noble gas data. Finally, the authors would like to thank two anonymous reviewers for
625 their detailed comments and observations which greatly improved the present paper.

627 **Appendix A. Mass balance model**

628 At least, two noble gases of different solubility are necessary to determine the degassed mass
 629 as outlined in Ju et al. (2019). The closed system is a one-step phase-partitioning process, and therefore,
 630 the degassed amount can be determined just by repeatedly adjusting the gas/liquid ratio until the result

631 $\left(\frac{A}{B}\right)_{(l)}$ fits into the measured data:

632
$$\left(\frac{A}{B}\right)_{(g)} = \left(\frac{A}{B}\right)_{(l)} \times \alpha$$

633
$$\alpha = \frac{\frac{r_A}{\phi_A} K_A}{\frac{r_B}{\phi_B} K_B}$$

634 Here:

635 $\left(\frac{A}{B}\right)_{(g)}$ = A and B ratio in exsolved bubbles, where A and B are different noble gases

636 $\left(\frac{A}{B}\right)_{(l)}$ = the composition of A and B remaining in the dissolved phase

637 α = partitioning coefficient for gas/liquid system

638 K_A, K_B = Henry's constant for A and B, from Sander et al., (2017)

639 r_A, r_B = dissolved-phase activity coefficients for A and B and

640 ϕ_A, ϕ_B = gas-phase fugacity coefficients for A and B.

641 In open system, the CO₂ bubble ($V_{(g)}$) is continuously lost into vadose zone carrying the noble
 642 gas tracers with it from the groundwater system until the plume is stabilized. An iteration calculation
 643 can be undertaken to account for the continuous loss and which terminates when the resultant mass (
 644 $m_{(l)}^i$) fits the observed noble gas data:

645
$$m_{A(l)}^i = m_{A(l)}^{i-1} - m_{A(g)}^{i-1}$$

646
$$m_{B(l)}^i = m_{B(l)}^{i-1} - m_{B(g)}^{i-1}$$

647 Here:

648 i = Iteration step

649 $m_{(l)}^{i-1}$ = mass in dissolved phase before $i - 1^{th}$ degassing loss (g)

650 $m_{(l)}^i$ = mass in dissolved phase after $i - 1^{th}$ degassing loss (g)

651 $m_{(g)}^{i-1}$ = degassed mass during $i - 1^{th}$ degassing process (g)

652 and degassed mass was determined from the degassed volume, such that:

653
$$m_{(g)}^{i-1} = C(V_{(g)} \times p^{i-1})$$

654
$$C = M/R \cdot T$$

655
$$p^{i-1} = \gamma K x^{i-1}/\Phi$$

656
$$x^{i-1} = 18 [NG]^{i-1} (\rho_{(l)} V_{(l)})^{-1}$$

657 Here:

658 $V_{(g)}$ = degassed volume during $i - 1^{th}$ degassing process (cc)

659 C = conversion factor from volume to mass

660 M = molar mass (g/mol)

661 R = gas constant (8.314 cc · atm/K/mol)

662 T = temperature (K)

663 p^{i-1} = partial pressure of removed noble gas during $i - 1^{th}$ degassing process

664 K = Henry's constant in units of pressure (atm)

665 γ = liquid-phase activity coefficient

666 Φ = gas-phase fugacity coefficient

667 x^{i-1} = molar fraction of noble gas in dissolved phase at $i - 1^{th}$ degassing moment ($mol_{NG}/mol_{(l)}$)

668 $[NG]^{i-1}$ = number of moles in dissolved phase at $i - 1^{th}$ degassing moment (mol)

669 $\rho_{(l)}$ = density of dissolved phase (g/cm^3)

670 $V_{(l)}$ = volume of dissolved phase (cm^3)

671 For an open system, an iterative model was used with a fixed $V_{(g)}$ value which should be small enough
672 to finally achieve convergence with the measured noble gas composition. The noble gas concentration
673 in the groundwater was gradually decreased in iterative steps. In the final stage ($i = n$), $\frac{m_A^n}{m_B^n}$ was
674 matched against the monitored composition, and then the total degassed volume was calculated by
675 multiplication of the bubble size ($V_{(g)}$) and the number of iteration steps (i) in the open system model.

676 **Appendix B. Model optimization**

677 Model optimization can be achieved in a similar manner to that used by Ballentine (1997) and
678 Castro et al. (2009). The optimization aims to replicate the monitored noble gas data into a calculated
679 mixing line with the smallest misfit to the observed data. As the monitored concentration is defined by
680 mixing between two end-members, therefore, to achieve the minimum misfit, the end-members
681 constituting the predicted mixing line were repeatedly updated. There are two end-members for the
682 mixing line such as: 1) the noble gas concentration after the degassing event; and 2) the noble gas
683 concentration of the background concentration (Supplementary Figure S3). The first end-member is the
684 function of the initial amount and total degassed budget ($V_{(g)}$) of a species as discussed in the previous
685 section. The second end-member is the function of excess air intrusion level (A) to the Air Saturated
686 Water (ASW) (Mazor and Bosch, 1987; Kipfer et al., 2002). Hence, this optimization process allows
687 quantification of the degassing amount and the background level of leaked plume within the
688 groundwater system. The optimization process is given by:

689

690
$$\chi^2 = \sum_{i=1}^N \left[\left(\frac{NG1_i^m - NG1_i^p}{\sigma_{NG1,i}} \right)^2 + \left(\frac{NG2_i^m - NG2_i^p}{\sigma_{NG2,i}} \right)^2 \right]$$

691 Here:

692 $i = i^{\text{th}}$ sample

693 $N =$ the number of sample

694 $\sigma =$ error of the observed data

695 $NG1^m =$ measured value of noble gas sample

696 $NG1^p =$ predicted value of noble gas sample from the arbitrary mixing line

697 This optimization process was conducted using a code compatible with the Matlab program.

698

699 **References**

700 Alcalde, J., Flude, S., Wilkinson, M., Johnson, G., Edlmann, K., Bond, C.E., Scott, V.,
701 Gilfillan, S.M.V., Ogaya, X., Haszeldine, R.S., 2018. Estimating geological CO₂ storage security to
702 deliver on climate mitigation. *Nat. Commun.* 9(1), 2201. <https://doi.org/10.1038/s41467-018-04423-1>.

703 Ballentine, C.J., 1997. Resolving the mantle He/Ne and crustal ²¹Ne/²²Ne in well gases. *Earth*
704 *Planet Sci. Lett.* 152(1-4), 233–249. [https://doi.org/10.1016/S0012-821X\(97\)00142-8](https://doi.org/10.1016/S0012-821X(97)00142-8).

705 Ballentine, C.J., Burgess, R., Marty, B., 2002. Tracing fluid origin, transport and interaction
706 in the crust. *Rev. Mineral. Geochem.* 47(1), 539–614.

707 Ballentine, C.J., O'nions, R.K., Oxburgh, E.R., Horvath, F., Deak, J., 1991. Rare gas
708 constraints on hydrocarbon accumulation, crustal degassing and groundwater flow in the Pannonian
709 Basin. *Earth Planet Sci. Lett.* 105(1-3), 229–246. [https://doi.org/10.1016/0012-821X\(91\)90133-3](https://doi.org/10.1016/0012-821X(91)90133-3).

710 Ballentine, C.J., Schoell, M., Coleman, D., Cain, B.A., 2001. 300-Myr-old magmatic CO₂ in
711 natural gas reservoirs of the west Texas Permian basin. *Nature* 409(6818), 327.
712 <https://doi.org/10.1038/35053046>.

713 Beaubien, S.E., Bigi, S., Lombardi, S., Sacco, P., and Tartarello, M.C., 2014. Groundwater
714 changes caused by flow through naturally occurring gas (±water) leakage points. 4th EAGE CO₂
715 Geological Storage Workshop 2014; Stavanger; Norway; April 22–24, 2014.

716 Beaubien, S.E., Jones, D.G., Gal, F., Barkwith, A.K.A.P., Braibant, G., Baubron, J.C., Ciotoli,
717 G., Graziani, S., Lister, T.R., Lombardi, S., Michel, K., Quattrocchi, F., Michel, K., 2013. Monitoring
718 of near-surface gas geochemistry at the Weyburn, Canada, CO₂-EOR site, 2001–2011. *Int. J. Greenh.*
719 *Gas Control* 16, 236–262. <https://doi.org/10.1016/j.ijggc.2013.01.013>.

720 Brennwald, M.S., Kipfer, R., Imboden, D.M., 2005. Release of gas bubbles from lake sediment
721 traced by noble gas isotopes in the sediment pore water. *Earth Planet Sci. Lett.* 235(1–2), 31–44.
722 <https://doi.org/10.1016/j.epsl.2005.03.004>.

723 Castro, M.C., Ma, L., Hall, C.M., 2009. A primordial, solar He–Ne signature in crustal fluids
724 of a stable continental region. *Earth Planet Sci. Lett.* 279(3–4), 174–184.
725 <https://doi.org/10.1016/j.epsl.2008.12.042>.

726 Cohen, G., Loisy, C., Laveuf, C., Le Roux, O., Delaplace, P., Magnier, C., Rouchon, V., Garcia,
727 B., Cerepi, A., 2013. The CO₂-Vadose project: Experimental study and modelling of CO₂ induced
728 leakage and tracers associated in the carbonate vadose zone. *Int. J. Greenh. Gas Control* 14, 128–140.
729 <https://doi.org/10.1016/j.ijggc.2013.01.008>.

730 Flude, S., Györe, D., Stuart, F.M., Zurakowska, M., Boyce, A.J., Haszeldine, R.S.,
731 Chalaturnyk, R., Gilfillan, S.M.V., 2017. The inherent tracer fingerprint of captured CO₂. *Int. J. Greenh.*
732 *Gas Control* 65, 40–54. <https://doi.org/10.1016/j.ijggc.2017.08.010>.

733 Flude, S., Johnson, G., Gilfillan, S.M., Haszeldine, R.S., 2016. Inherent tracers for carbon
734 capture and storage in sedimentary formations: composition and applications. *Environ. Sci. Technol.*
735 50(15), 7939–7955. <https://doi.org/10.1021/acs.est.6b01548>.

736 Gilfillan, S.M.V., Ballentine, C.J., Holland, G., Blagburn, D., Sherwood Lollar, B., Scott, S.,
737 Schoell, M., Cassidy, M., 2008. The noble gas geochemistry of natural CO₂ gas reservoirs from the
738 Colorado Plateau and Rocky Mountain provinces, USA. *Geochim. Cosmochim. Acta* 72, 1174–1198.
739 <https://doi.org/10.1016/j.gca.2007.10.009>.

740 Gilfillan, S.M.V., Haszeldine, S., Stuart, F., Gyore, D., Kilgallon, R., Wilkinson, M., 2014.
741 The application of noble gases and carbon stable isotopes in tracing the fate, migration and storage of
742 CO₂. *Energy Procedia* 63, 4123–4133. <https://doi.org/10.1016/j.egypro.2014.11.443>.

743 Gilfillan, S.M.V., Lollar, B.S., Holland, G., Blagburn, D., Stevens, S., Schoell, M., Cassidy,
744 M., Ding, Z., Zhou, Z., Lacrampe-Couloume, G., Ballentine, C.J., 2009. Solubility trapping in
745 formation water as dominant CO₂ sink in natural gas fields. *Nature* 458(7238), 614.
746 <https://doi.org/10.1016/j.gca.2007.10.009>.

747 Gilfillan, S.M.V., Sherk, G.W., Poreda, R.J., Haszeldine, R.S., 2017. Using noble gas

748 fingerprints at the Kerr Farm to assess CO₂ leakage allegations linked to the Weyburn-Midale CO₂
749 monitoring and storage project. *Int. J. Greenh. Gas Control* 63, 215–225.
750 <https://doi.org/10.1016/j.ijggc.2017.05.015>.

751 Gilfillan, S.M.V., Wilkinson, M., Haszeldine, R.S., Shipton, Z.K., Nelson, S.T., Poreda, R.J.,
752 2011. He and Ne as tracers of natural CO₂ migration up a fault from a deep reservoir. *Int. J. Greenh.*
753 *Gas Control* 5(6), 1507–1516. <https://doi.org/10.1016/j.ijggc.2011.08.008>.

754 Harvey, O.R., Qafoku, N.P., Cantrell, K.J., Lee, G., Amonette, J.E., Brown, C.F., 2012.
755 Geochemical implications of gas leakage associated with geologic CO₂ storage. *Crit Rev. Environ. Sci.*
756 *Technol.* 47(1), 23–36. <https://doi.org/10.1021/es3029457>.

757 Holland, G., Gilfillan, S., 2013. Application of noble gases to the viability of CO₂ storage. In
758 : Burnard, P. (Eds), *The Noble Gases as Geochemical Tracers. Advances in Isotope Geochemistry*,
759 Springer, Berlin, Heidelberg 177–223. https://doi.org/10.1007/978-3-642-28836-4_8.

760 Ide, S.T., Friedmann, S.J., Herzog, H.J., 2006. CO₂ leakage through existing wells: current
761 technology and regulations. In *8th International Conference on Greenhouse Gas Control Technologies*,
762 19–22.

763 IEAGHG, 2011. *Potential Impacts on Groundwater Resources of CO₂ Storage*. IEAGHG,
764 Cheltenham, UK.

765 IPCC, 2005. *Intergovernmental Panel on Climate Change. Special Report on CO₂ Capture*
766 *and Storage*, edited, pp. 208–210.

767 Ju, Y., Beaubien, S.E., Lee, S.S., Kaown, D., Hahm, D., Lee, S., Park, I.W., Park, K., Yun,
768 S.T., Lee, K.K., 2019. Application of natural and artificial tracers to constrain CO₂ leakage and
769 degassing in the K-COSEM site, South Korea. *Int. J. of Greenh. Gas Control* 86, 211–225.
770 <https://doi.org/10.1016/j.ijggc.2019.05.002>.

771 Ju, Y., Kaown, D., Lee, K.K., 2018a. A three-pronged approach for identifying source and

772 extent of nitrate contamination in groundwater. *J. Soil Water Conserv.* 73(5), 493–503.
773 <https://doi.org/10.2489/jswc.73.5.493>.

774 Ju, Y., Lee, S.S., Kaown, D., Lee, K.K., 2018b. Application of Inert Gas Tracers to Identify the
775 Physical Processes Governing the Mass Balance Problem of Leaking CO₂ in Shallow Groundwater
776 System. 14th Greenhouse Gas Control Technologies Conference; Melbourne; Australia; October 21–
777 26. https://papers.ssrn.com/sol3/papers.cfm?abstract_id=3365686.

778 Kilgallon, R., Gilfillan, S.M.V., Edlmann, K., McDermott, C.I., Naylor, M., Haszeldine, R.S.,
779 2018. Experimental determination of noble gases and SF₆, as tracers of CO₂ flow through porous
780 sandstone. *Chem. Geol.* 480, 93–104. <https://doi.org/10.1016/j.chemgeo.2017.09.022>.

781 Kim, I., Hahm, D., Rhee, T.S., Kim, T.W., Kim, C.S., Lee, S., 2016. The distribution of glacial
782 meltwater in the Amundsen Sea, Antarctica, revealed by dissolved helium and neon. *J. Geophys. Res.:
783 Oceans* 121(3), 1654–1666. <https://doi.org/10.1002/2015JC011211>.

784 Kipfer, R., Aeschbach-Hertig, W., Peeters, F., Stute, M., 2002. Noble gases in lakes and
785 ground waters. *Rev. Mineral. Geochem.* 47(1), 615–700. <https://doi.org/10.2138/rmg.2002.47.14>.

786 LaForce, T., Ennis-King, J., Boreham, C., Paterson, L., 2014. Residual CO₂ saturation estimate
787 using noble gas tracers in a single-well field test: the CO₂CRC Otway project. *Int. J. Greenh. Gas
788 Control* 26, 9–21. <https://doi.org/10.1016/j.ijggc.2014.04.009>.

789 Lee, K.K., Lee, S.H., Yun, S.T., Jeon, S.W., 2016. Shallow groundwater system monitoring
790 on controlled CO₂ release sites: a review on field experimental methods and efforts for CO₂ leakage
791 detection. *Geosci. J.* 20(4), 569–583. <https://doi.org/10.1007/s12303-015-0060-z>.

792 Lee, S.S., Ju, Y., HA, S.W., Joun, W.T., Jun, S.C., Yun, S.T., Lee, K.K., 2018. Controlled CO₂
793 Injection into a Shallow Aquifer and Leakage Detection Monitoring by Two Different Leakage Events
794 at the K-Cosem Site, Korea. In 14th Greenhouse Gas Control Technologies Conference Melbourne;
795 Australia; October 21–26. https://papers.ssrn.com/sol3/papers.cfm?abstract_id=3366360.

796 Lee, S.S., Kim, H.H., Joun, W.T., Lee, K.K., 2017. Design and Construction of
797 Groundwater Monitoring Network at Shallow-depth CO₂ Injection and Leak Test Site, Korea. *Energy*
798 *Procedia* 114, 3060–3069. <https://doi.org/10.1016/j.egypro.2017.03.1434>.

799 Lemieux, J.M., 2011. The potential impact of underground geological storage of carbon
800 dioxide in deep saline aquifers on shallow groundwater resources. *Hydrogeol. J.* 19(4), 757–778.
801 <https://doi.org/10.1007/s10040-011-0715-4>.

802 Lions, J., Devau, N., De Lary, L., Dupraz, S., Parmentier, M., Gombert, P., Dictor, M.C., 2014.
803 Potential impacts of leakage from CO₂ geological storage on geochemical processes controlling fresh
804 groundwater quality: a review. *Int. J. Greenh. Gas Control* 22, 165–175.
805 <https://doi.org/10.1016/j.ijggc.2013.12.019>.

806 Lollar, B.S., Ballentine, C.J., Onions, R.K., 1997. The fate of mantle-derived carbon in a
807 continental sedimentary basin: integration of C/He relationships and stable isotope signatures. *Geochim.*
808 *Cosmochim. Acta* 61(11), 2295–2307. [https://doi.org/10.1016/S0016-7037\(97\)00083-5](https://doi.org/10.1016/S0016-7037(97)00083-5).

809 Lott, D.E., Jenkins, W.J., 1998. Advances in analysis and shipboard processing of tritium and
810 helium samples. *International WOCE Newsletter*, 30, 27–30.

811 Lu, J., Cook, P.J., Hosseini, S.A., Yang, C., Romanak, K.D., Zhang, T., Freifeld, B.M., Smyth,
812 R.C., Zeng, H., Hovorka, S.D., 2012. Complex fluid flow revealed by monitoring CO₂ injection in a
813 fluvial formation. *J. Geophys. Res. Solid Earth* 117. <https://doi.org/10.1029/2011JB008939>.

814 Ma, L., Castro, M.C., Hall, C.M., 2009. Atmospheric noble gas signatures in deep Michigan
815 Basin brines as indicators of a past thermal event. *Earth Planet Sci. Lett.* 277(1–2), 137–147.
816 <https://doi.org/10.1016/j.epsl.2008.10.015>.

817 Mackintosh, S.J., Ballentine, C.J., 2012. Using ³He/⁴He isotope ratios to identify the source of
818 deep reservoir contributions to shallow fluids and soil gas. *Chem. Geol.* 304–305, 142–150.
819 <https://doi.org/10.1016/j.chemgeo.2012.02.006>.

820 Mazor, E., Bosch, A., 1987. Noble gases in formation fluids from deep sedimentary basins: a

821 review. *Appl. Geochem.* 2(5–6), 621–627. [https://doi.org/10.1016/0883-2927\(87\)90014-X](https://doi.org/10.1016/0883-2927(87)90014-X).

822 Myers, M., Stalker, L., Pejčić, B., Ross, A., 2013. Tracers—Past, present and future applications
823 in CO₂ geosequestration. *Appl. Geochem.* 30, 125–135.
824 <https://doi.org/10.1016/j.apgeochem.2012.06.001>.

825 Nimz, G.J., Hudson, G.B., 2005. The use of noble gas isotopes for monitoring leakage of
826 geologically stored CO₂. In: Thomas, D., Benson, S. (Eds.), *Carbon Dioxide Capture for Storage in*
827 *Deep Geologic Formations* vol. 2. Elsevier Press, Amsterdam 1113–1130.

828 Parkhurst, D.L., Appelo, C.A.J., 2013. Description of input and examples for PHREEQC
829 version 3: a computer program for speciation, batch-reaction, one-dimensional transport, and inverse
830 geochemical calculations (No. 6-A43). US Geological Survey. <https://doi.org/10.3133/tm6A43>.

831 Pinti, D.L., Marty, B., 1995. Noble gases in crude oils from the Paris Basin, France:
832 Implications for the origin of fluids and constraints on oil-water-gas interactions. *Geochim. Cosmochim.*
833 *Acta* 59(16), 3389–3404. [https://doi.org/10.1016/0016-7037\(95\)00213-J](https://doi.org/10.1016/0016-7037(95)00213-J).

834 Rillard, J., Loisy, C., Le Roux, O., Cerepi, A., Garcia, B., Noirez, S., Rouchon, V., Delaplaceb,
835 P., Willequet, O., Bertrand, C., 2015. The DEMO-CO₂ project: A vadose zone CO₂ and tracer leakage
836 field experiment. *Int. J. Greenh. Gas Control* 39, 302–317. <https://doi.org/10.1016/j.ijggc.2015.04.012>.

837 Risk, D., Lavoie, M., Nickerson, N., 2015. Using the Kerr investigations at Weyburn to screen
838 geochemical tracers for near-surface detection and attribution of leakage at CCS/EOR sites. *Int. J.*
839 *Greenh. Gas Control* 35, 13–17. <https://doi.org/10.1016/j.ijggc.2015.01.019>.

840 Sander, R., 2017. Henry's Law Constants. In: Linstrom, P.J., Mallard, W.G. (Eds.), *NIST*
841 *Chemistry WebBook*, NIST Standard Reference Database Number 69. National Institute of Standards
842 and Technology, Gaithersburg MD, 20899. <https://doi.org/10.18434/T4D303>.

843 Sathaye, K.J., Larson, T.E., Hesse, M.A., 2016. Noble gas fractionation during subsurface gas
844 migration. *Earth Planet Sci. Lett.* 450, 1–9. <https://doi.org/10.1016/j.epsl.2016.05.034>.

845 Sechriest, R.E., 1960. Relationship between total alkalinity, conductivity, original pH, and
846 buffer action of natural water. OHIO J. SCI. 60(5), 303.

847 Stalker, L., Boreham, C., Underschultz, J., Freifeld, B., Perkins, E., Schacht, U., Sharma, S.,
848 2009. Geochemical monitoring at the CO2CRC Otway Project: tracer injection and reservoir fluid
849 acquisition. Energy Procedia 1(1), 2119–2125. <https://doi.org/10.1016/j.egypro.2009.01.276>.

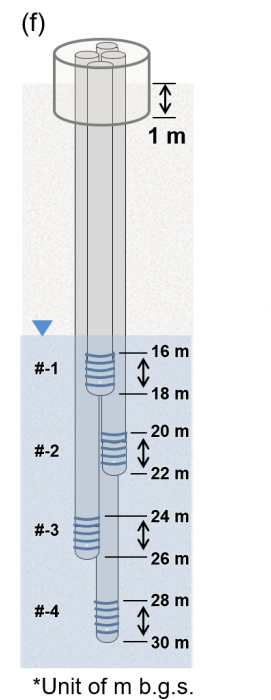
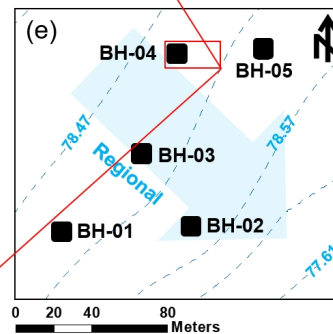
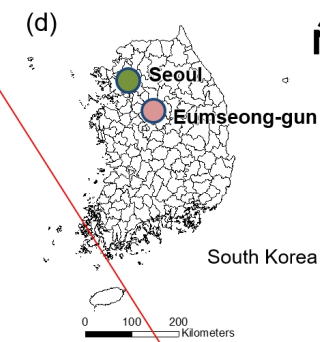
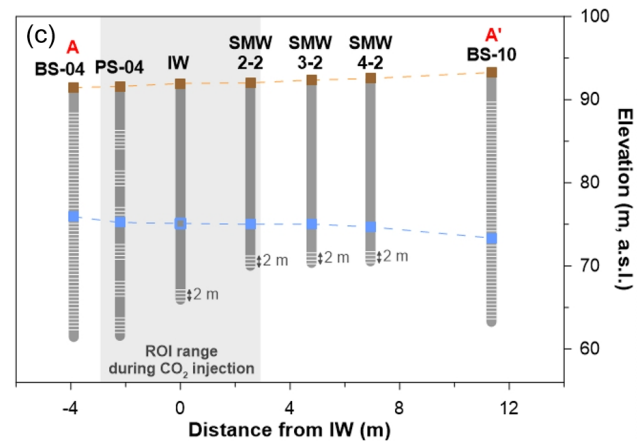
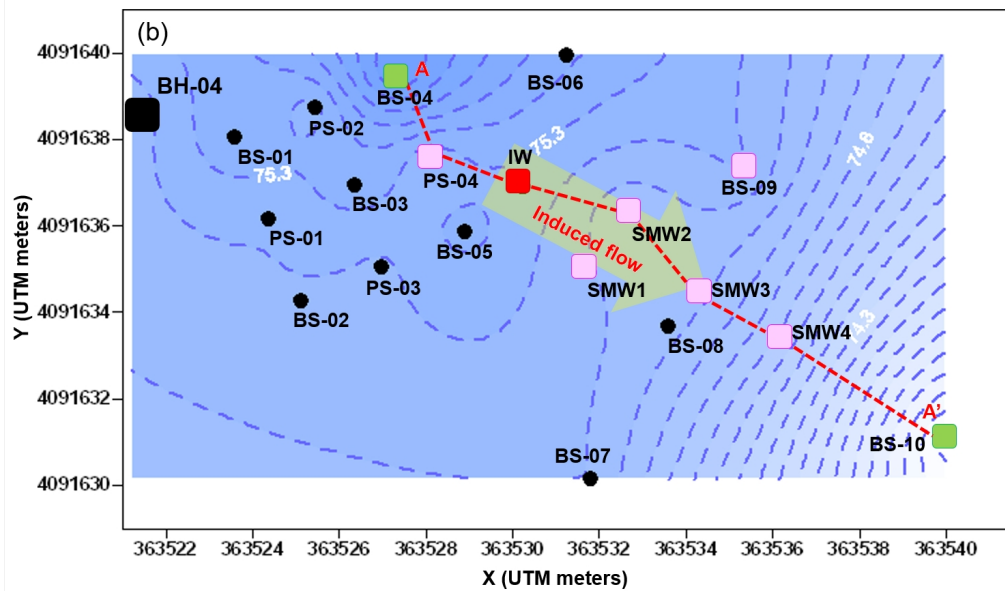
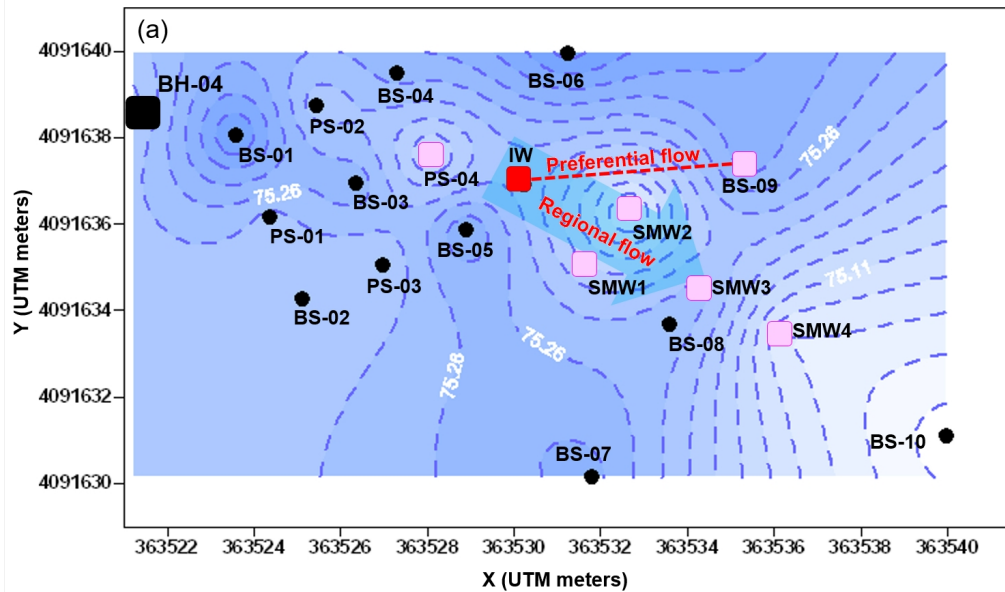
850 Stalker, L., Boreham, C., Underschultz, J., Freifeld, B., Perkins, E., Schacht, U., Sharma, S.,
851 2015. Application of tracers to measure, monitor and verify breakthrough of sequestered CO₂ at the
852 CO2CRC Otway Project, Victoria, Australia. Chem. Geol. 399, 2–19.
853 <https://doi.org/10.1016/j.chemgeo.2014.12.006>.

854 Stanley, R.H., Jenkins, W.J., Lott, D.E., Doney, S.C., 2009. Noble gas constraints on air-sea
855 gas exchange and bubble fluxes. J. Geophys. Res.: Oceans 114(C11).
856 <https://doi.org/10.1029/2009JC005396>.

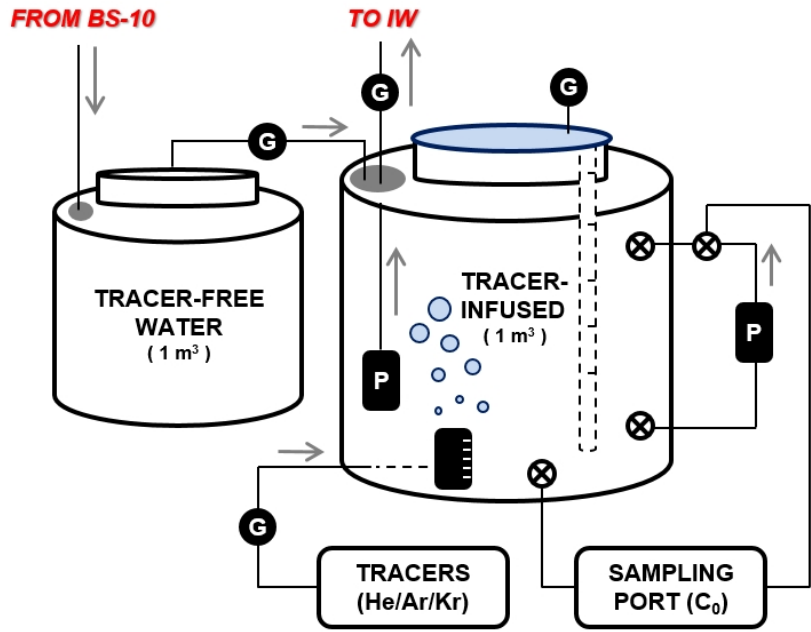
857 Vialle, S., Contraires, S., Zinzsner, B., Clavaud, J.B., Mahiouz, K., Zuddas, P., Zamora, M.,
858 2014. Percolation of CO₂-rich fluids in a limestone sample: Evolution of hydraulic, electrical, chemical,
859 and structural properties. J. Geophys. Res. Solid Earth 119(4), 2828–2847.
860 <https://doi.org/10.1002/2013JB010656>.

861 Zheng, C., Bennett, G.D., 2002. Applied contaminant transport modeling. Wiley-Interscience,
862 New York.

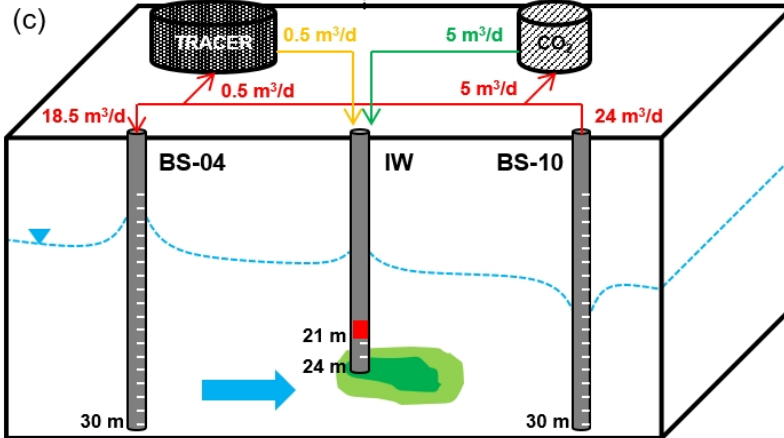
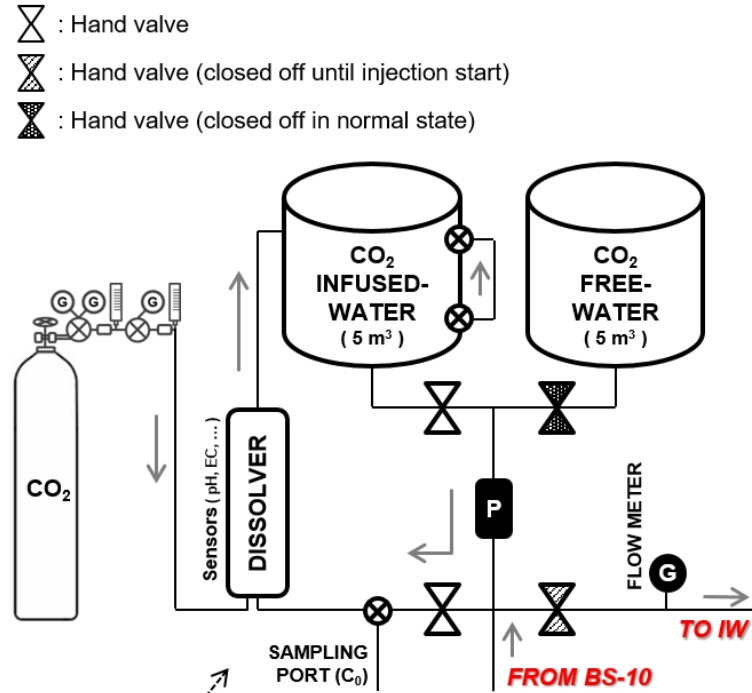
863 Zhou, Z., Ballentine, C.J., Kipfer, R., Schoell, M., Thibodeaux, S., 2005. Noble gas tracing of
864 groundwater/coalbed methane interaction in the San Juan Basin, USA. Geochim. Cosmochim. Acta
865 69(23), 5413–5428. <https://doi.org/10.1016/j.gca.2005.06.027>.



(a)

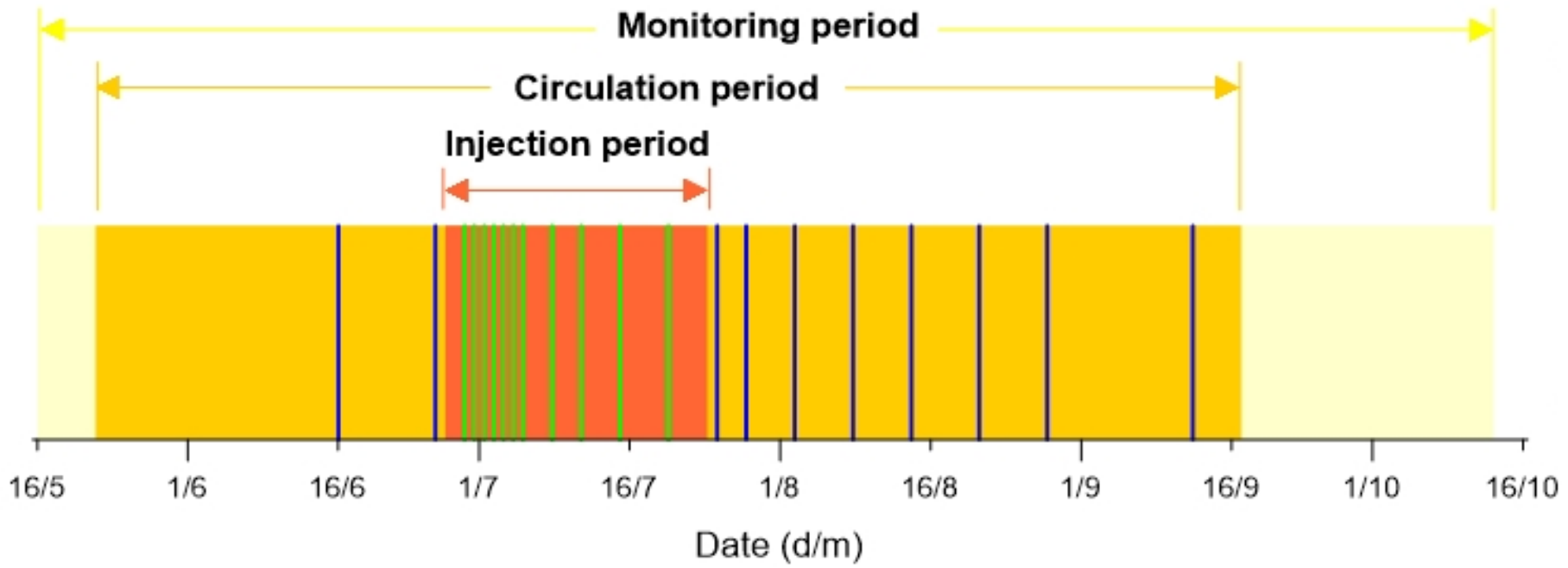


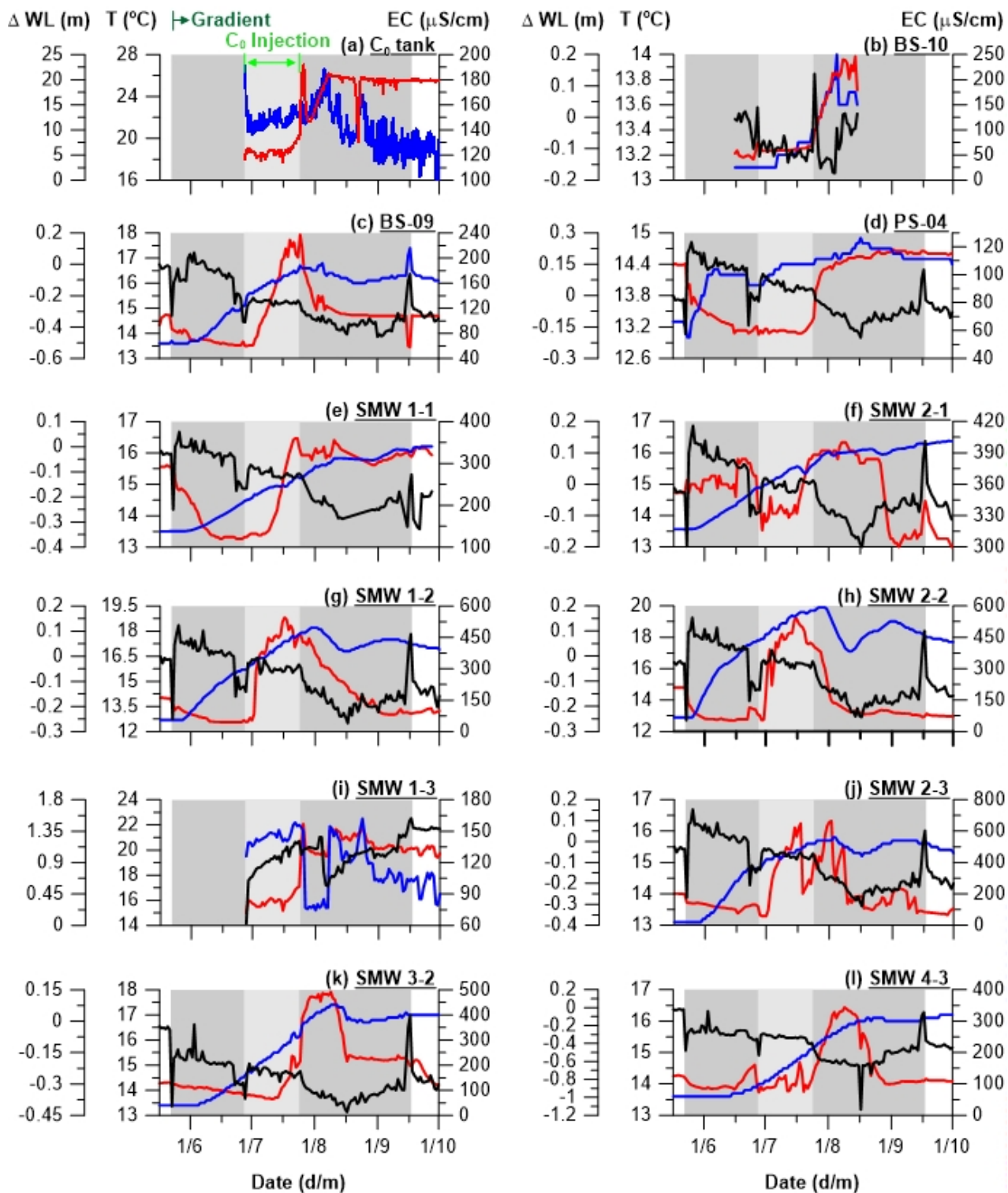
(b)

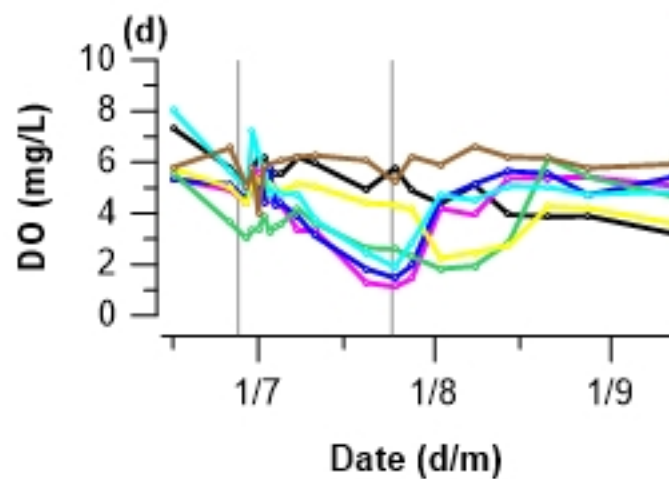
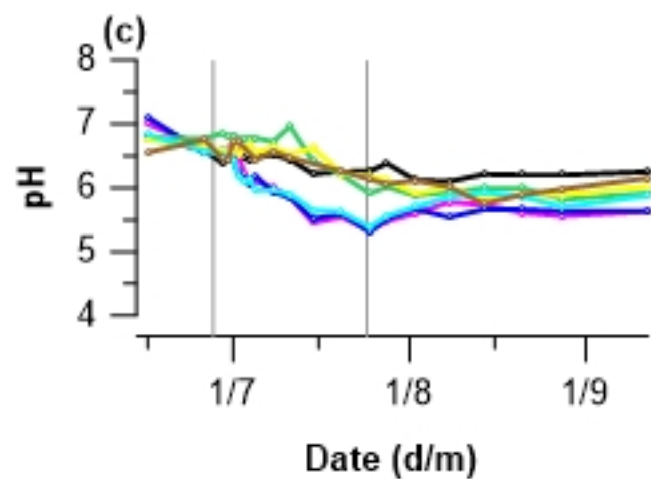
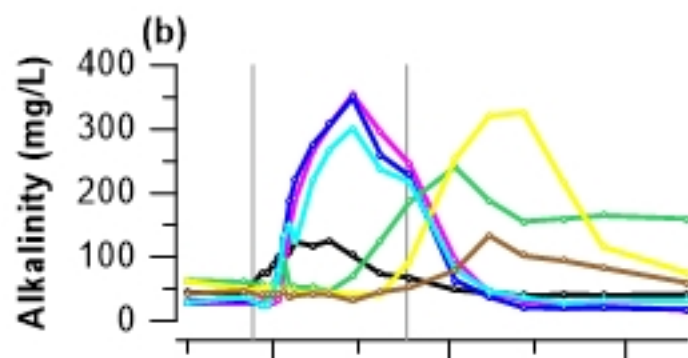
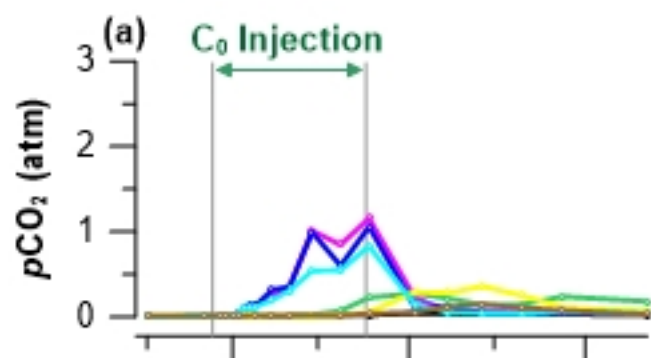


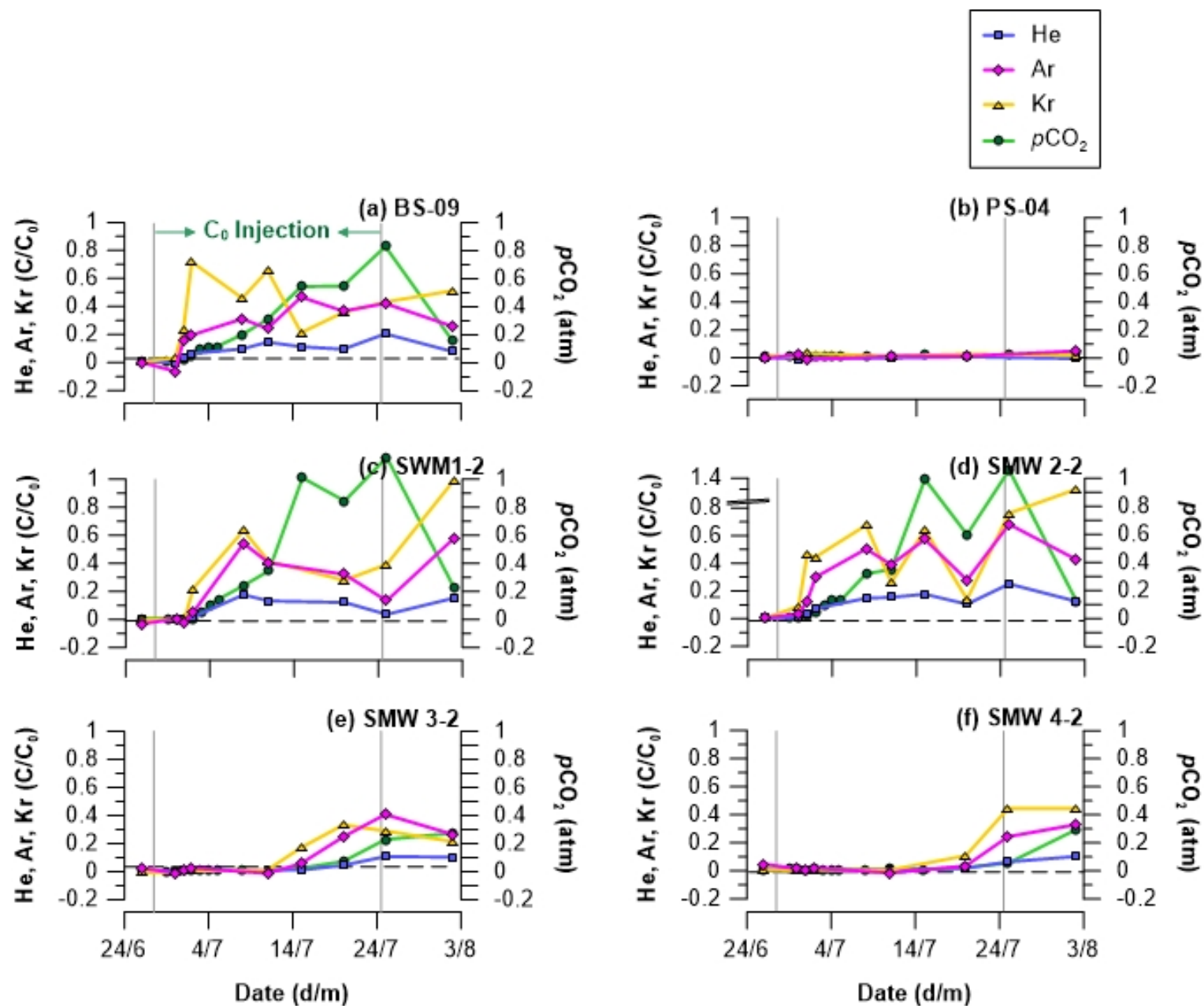
*Unit of m b.g.s.

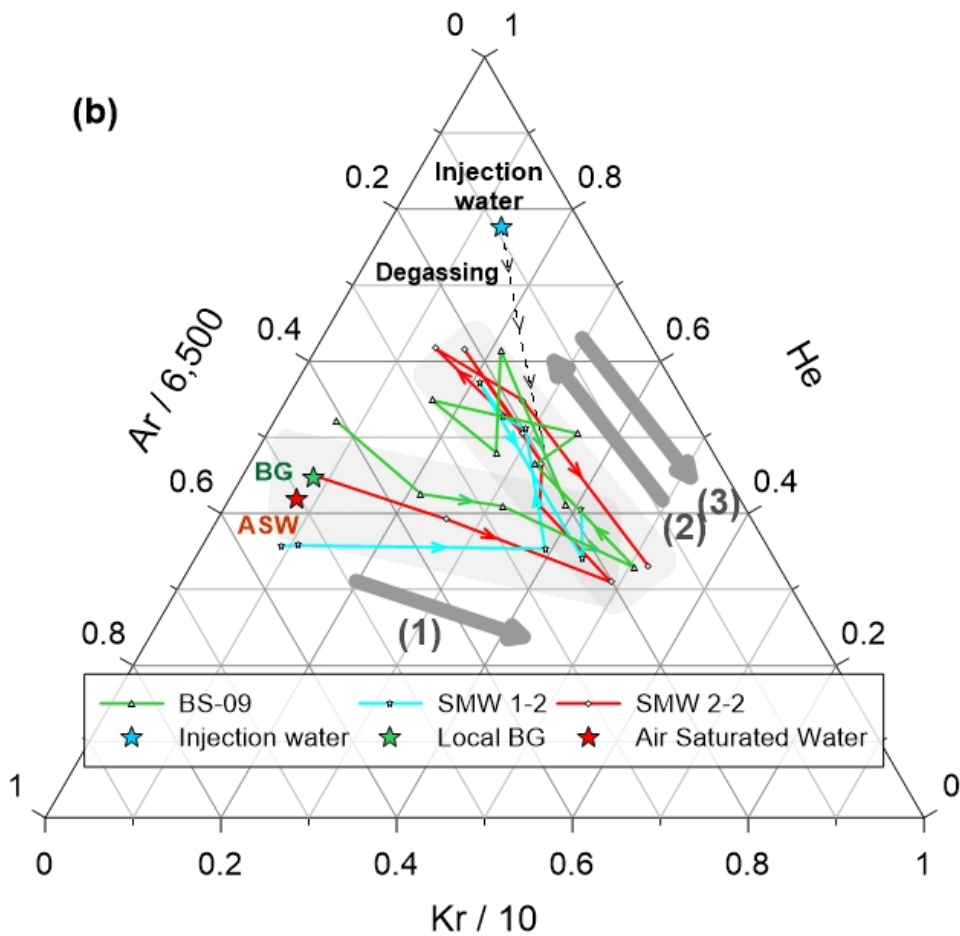
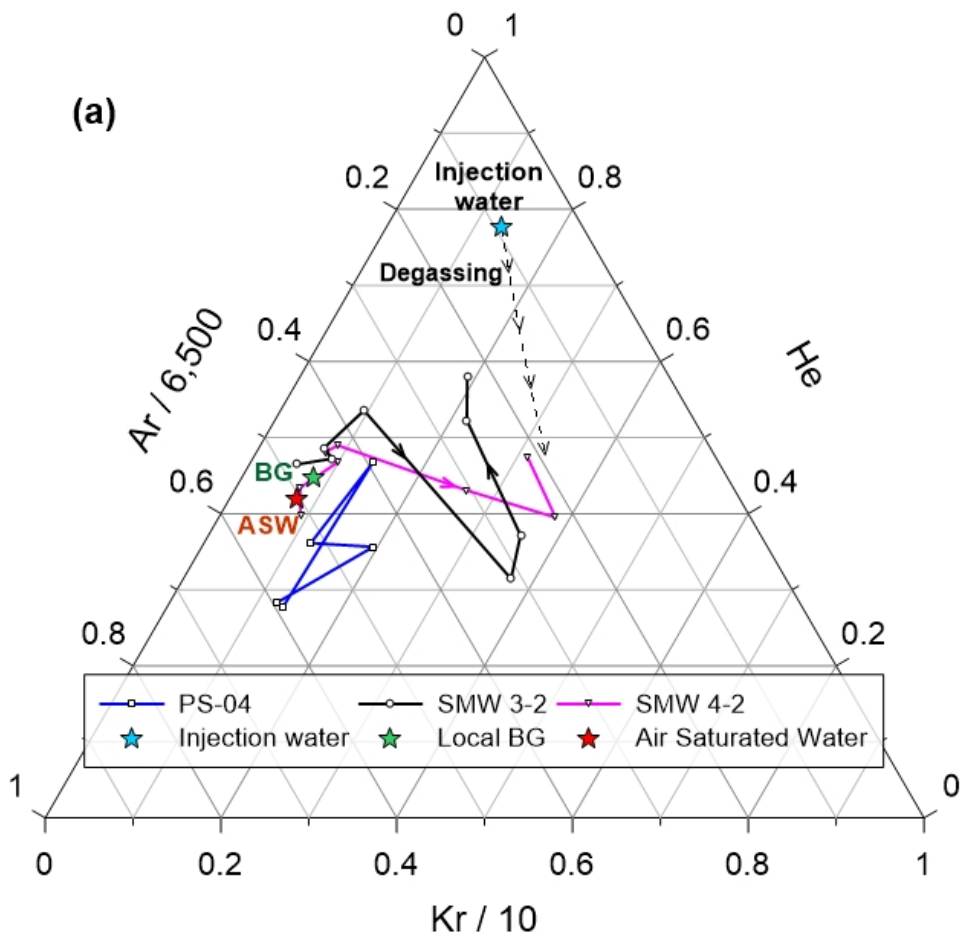
- Water sample campaign (non-injection period)
- Water sample campaign (injection period)

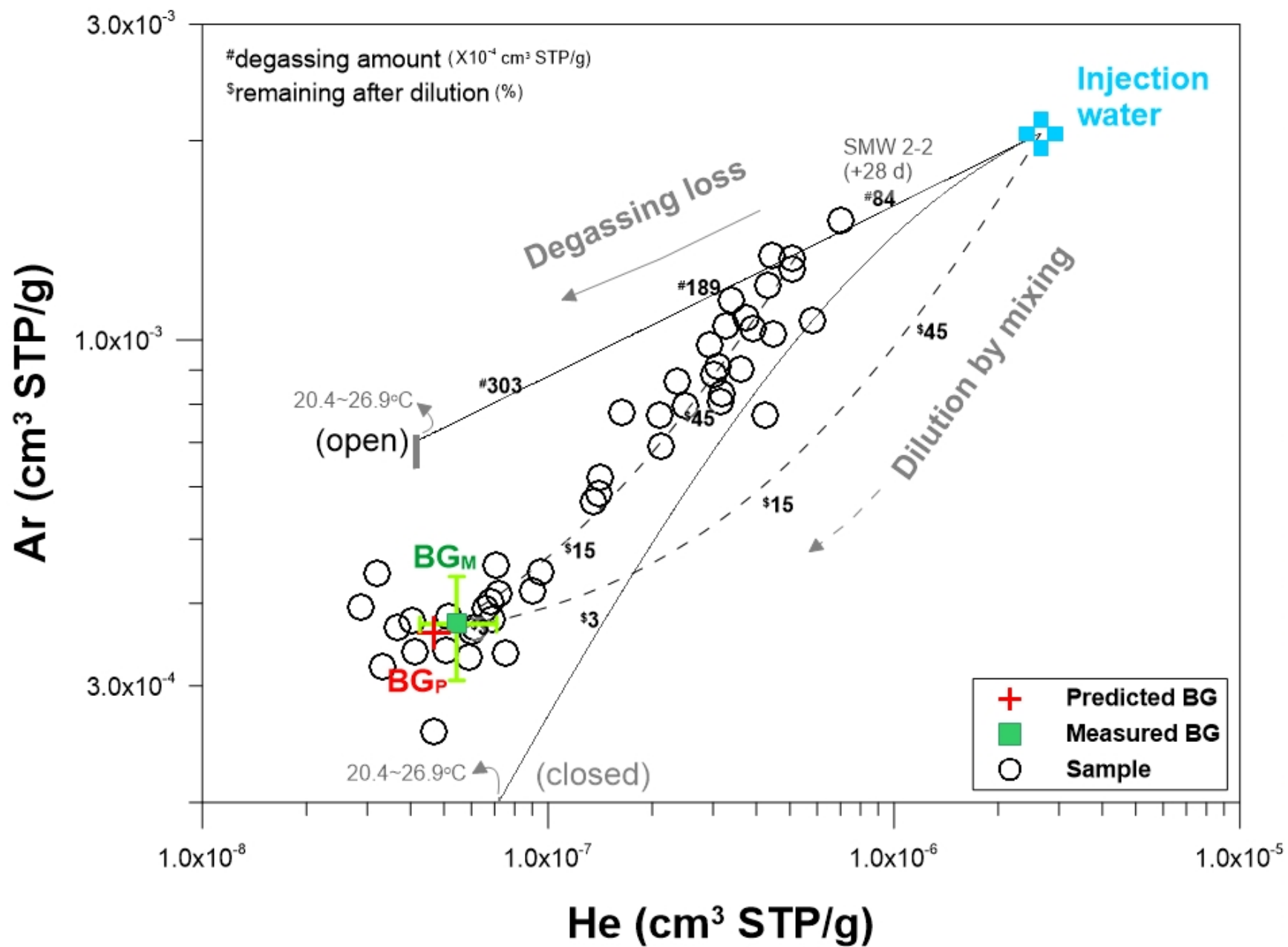


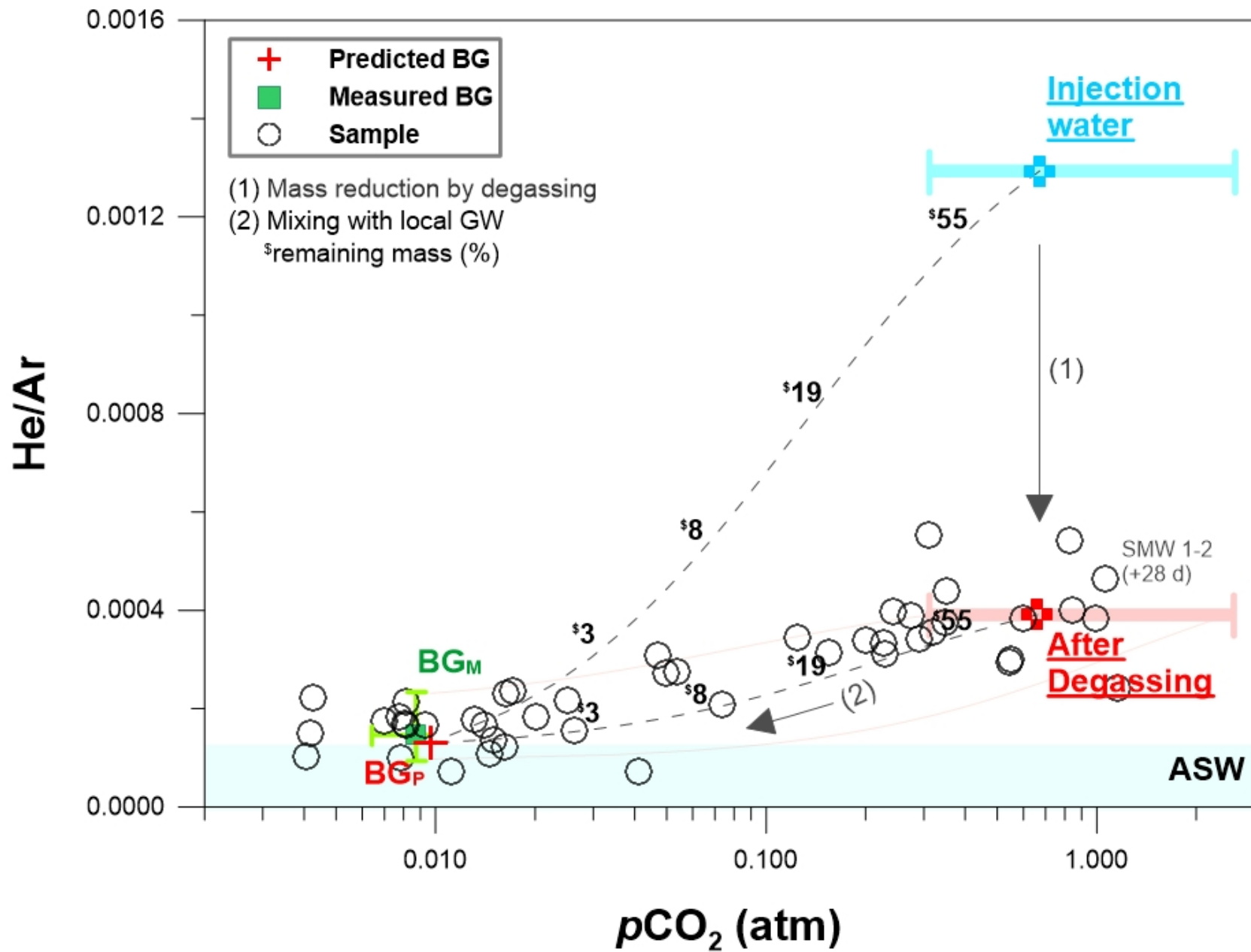


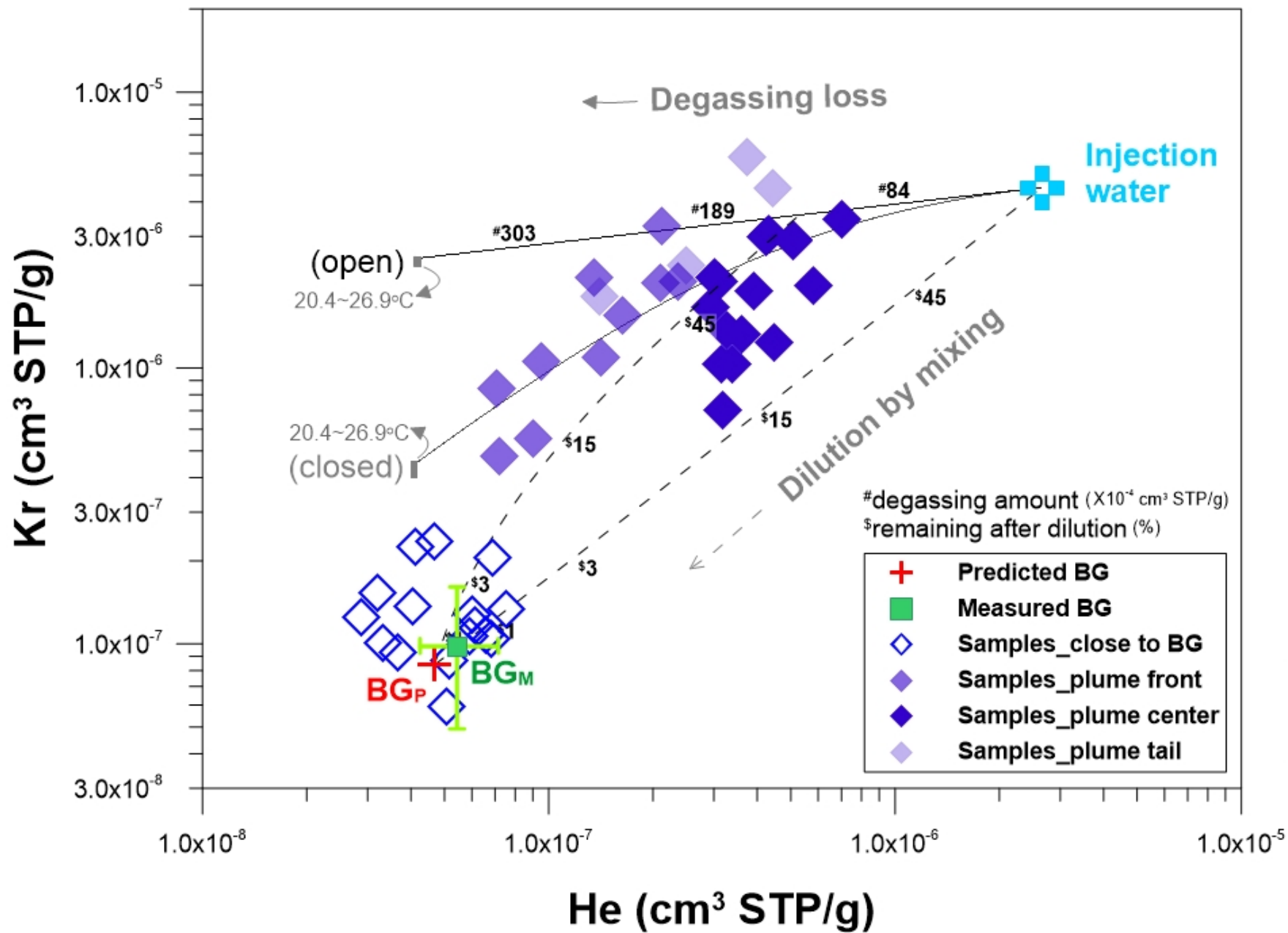


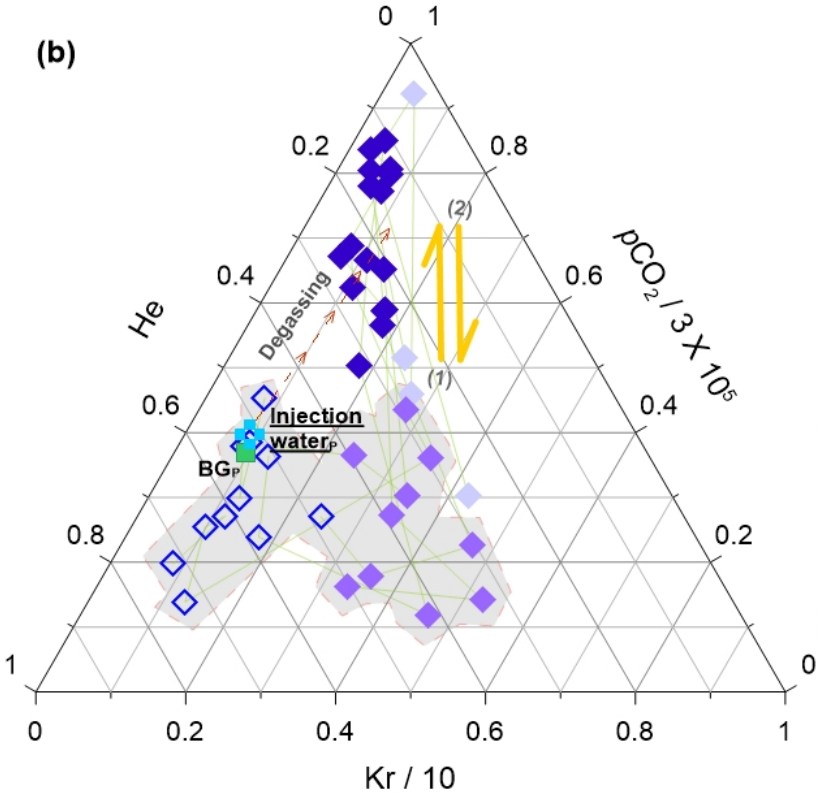
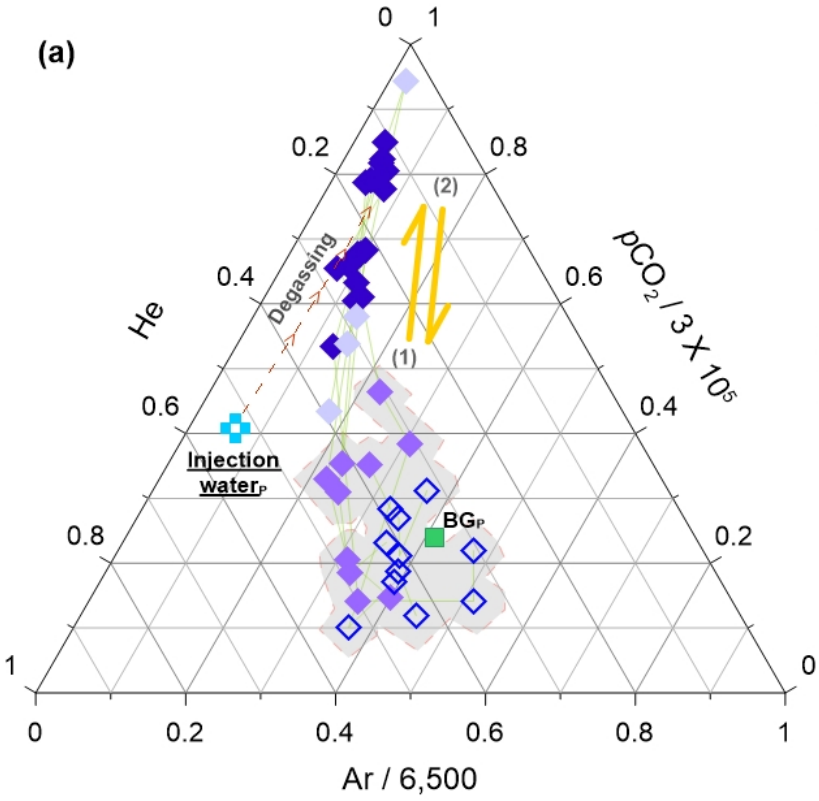
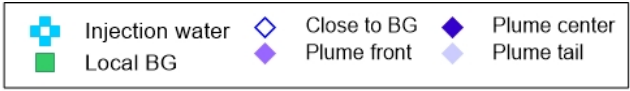












Declaration of interests

The authors declare that they have no known competing financial interests or personal relationships that could have appeared to influence the work reported in this paper.

The authors declare the following financial interests/personal relationships which may be considered as potential competing interests:

YeoJin Ju: Conceptualization, Methodology, Data Curation, Investigation, Writing - Original Draft

Stuart M. V. Gilfillan: Writing - Review & Editing

Seong-Sun Lee: Project administration, Investigation

Dugin Kaown: Data Curation

Doshik Hahm: Resources, Data Curation, Writing - Review & Editing

Sanghoon Lee: Data Curation

In-Woo Park: Data Curation

Seung-Wook Ha: Investigation

Keyhong Park: Resources, Data Curation

Hyun-Kwon Do: Investigation

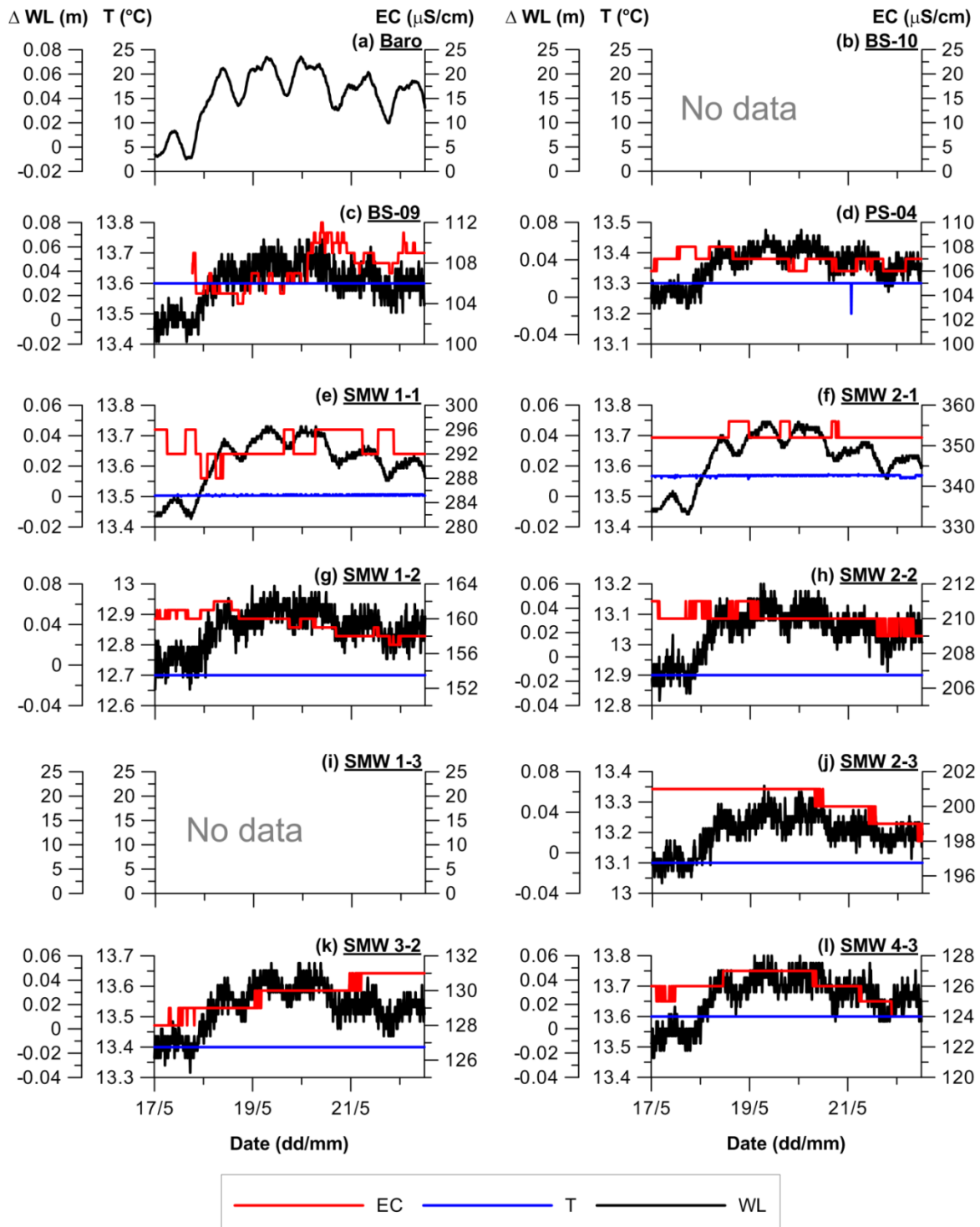
Seong-Taek Yun: Funding acquisition, Project administration, Writing - Review & Editing

Kang-Kun Lee: Funding acquisition, Supervision, Writing - Review & Editing

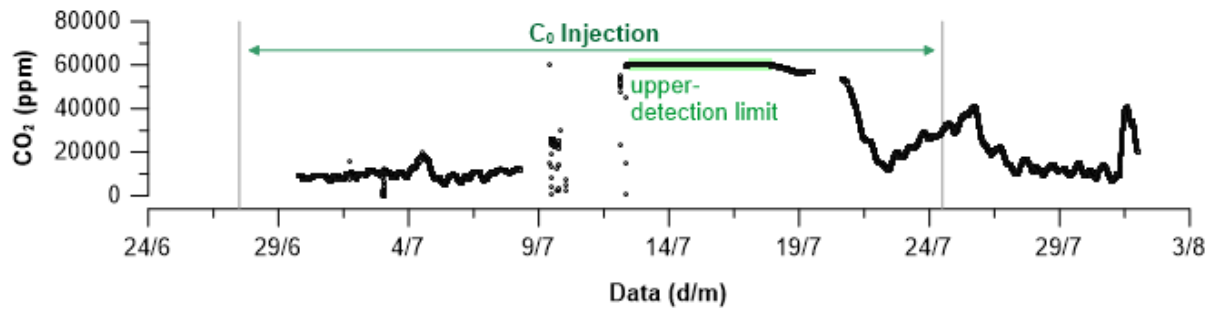
Supplementary Material

Application of noble gas tracers to identify the retention mechanisms of CO₂ migrated from a deep reservoir into shallow groundwater

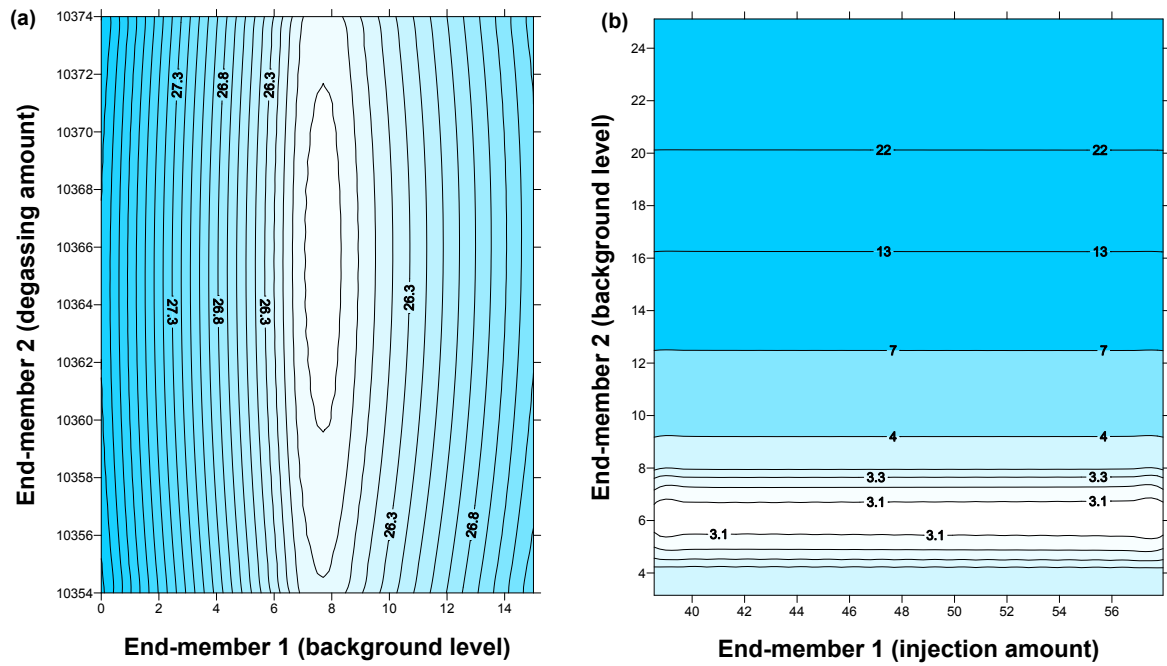
YeoJin Ju¹, Stuart M. V. Gilfillan², Seong-Sun Lee¹, Dugin Kaown¹, Doshik Hahm³, Sanghoon Lee¹, In-Woo Park¹, Seung-Wook Ha¹, Keyhong Park⁴, Hyun-Kwon Do⁵, Seong-Taek Yun⁵, Kang-Kun Lee¹,*



Supplementary Figure S1. Water level (WL), temperature (T) and electrical conductivity (EC) data. Measurement was completed in the monitoring wells continuously using LTC data logger before groundwater circulation (from 16 May 2017 to 22 May 2017). Note that the WL was corresponding to the atmospheric pressure change before experiment initiation and, T and EC were consistent throughout this period.



Supplementary Figure S2. CO₂ concentration monitored above the injection material inside the IW. The concentration was significantly elevated and reached to the maximum limit of the equipment suggesting the CO₂ leakage through the isolation materials occurred during injection period.



Supplementary Figure S3. Model optimization by χ^2 minimization method. In the left figure (a), the degassing amount (i.e. y-axis) and background level of noble gases (i.e. x-axis) were decided at the smallest χ^2 (i.e. center of the white-colored zone). In the right figure (b), the background level of CO_2 (i.e. y-axis) and injection amount of CO_2 (i.e. BG_p , x-axis) were decided at the smallest χ^2 (i.e. center of the white-colored zone).